NOVEL APPROACHES TO GRID THERAPY: ELECTRON GRID AND PHOTON MINIBEAMS

A Dissertation
Presented to
The Academic Faculty

By

Gregory Szalkowski

In Partial Fulfillment
of the Requirements for the Degree
Doctor of Philosophy in the
School of Woodruff School of Mechanical Engineering

Georgia Institute of Technology

August 2019

NOVEL APPROACHES TO GRID THERAPY: ELECTRON GRID AND PHOTON MINIBEAMS

Approved by:

Dr. C-K Chris Wang, Advisor
School of Mechanical Engineering
Georgia Institute of Technology

Dr. Nolan Hertel
School of Mechanical Engineering
Georgia Institute of Technology

Dr. Anna Erickson
School of Mechanical Engineering
Georgia Institute of Technology

Dr. Eric Elder
School of Mechanical Engineering
Georgia Institute of Technology

Dr. Eva Lee
School of Industrial and Systems Engineering
Georgia Institute of Technology

Date Approved: April 23, 2019

ACKNOWLEDGEMENTS

I would like to start by expressing my deepest thanks and appriciation to my advisor Dr. C-K Chris Wang, who helped kindle my interest in research and who guided me through my time in graduate school. His help and mentorship were invaluable both for this work and for my development as a researcher. I would also like to thank the other members of my committee, Dr. Nolan Hertel, Dr. Anna Erickson, Dr. Eric Elder, and Dr. Eva Lee for their guidance and assistance.

I would also like to thank my friends and collegues for their assistance and support throughout my time in graduate school, in particular Caleigh Samuels and Serdar Charyyev for help with the simulations that formed the backbone of my work.

Finally, I would like to thank my parents for their unwavering support and encouragement thoughout my life, and without whom I would never have gotten this far.

TABLE OF CONTENTS

LIST OF TABLES

LIST OF FIGURES

SUMMARY

This dissertation describes a study into the dosimetric properties of several new forms of spatially fractionated radiation therapy, commonly referred to as SFRT or GRID; small beam electron GRID, radioisotope-based photon minibeam GRID, and megavoltage photon minibeam GRID. For each methodology, a combination of Monte Carlo simulation (using the Monte Carlo code MCNP6) and physical measurements (using EBT3 radiochromic film) was used to characterize the dose rate and peak-to-valley dose ratio (PVDR) of each of the proposed methods. This presented work shows the calculated and/or measured in-phantom dose distributions from each of these new modalities. In all cases, beam definition similar to or exceeding that of clinically used GRID therapy techniques was achieved, as defined by the PVDR. In addition, the photon-based minibeam modalities were able to effectively produce beams below 5 mm in diameter, which could be expected to significantly improve healthy tissue recovery. Also in this work, the limitations and challenges of each of these techniques are discussed, namely the reduced dose rate that corresponds to the small beam size. However, each method has some conditions under which it can effectively be used, and with further development in specified areas, aspects of this work could be applied clinically.

CHAPTER 1
INTRODUCTION AND BACKGROUND

1.1 Overview

While the treatment techniques have changed over the years, the goal of radiation therapy has always been to administer dose in a way that maximizes the damage to a specific volume of tissue while minimizing damage to any other tissue. In this way, cancerous (or other diseased) tissue can be killed while minimizing the side effects that would result from damage to healthy tissue. While a variety of treatment options exist to meet this constraint, from brachytherapy (the temporary or permanent implantation of radioactive seeds into the target tissue) to proton therapy (the use of high energy proton beams to deliver dose to the target tissue), accelerator based photon therapy has been the most common treatment modality.

In almost all modern photon treatments, healthy tissue dose is kept low by irradiating the patient using beams from multiple different directions, or even by keeping the beam on as the accelerator moves in an arc around the patient, while keeping the target tissue at the center of rotation. While this can irradiate a relatively large volume of healthy tissue, the dose to this tissue is kept low enough such that it does not cause any major damage. However, this dose can increase the chance of secondary cancers, with some estimates stating an almost twofold increase in cancer risk.[1]

However, it is also possible to reduce the side effects of radiation therapy by instead concentrating the dose to healthy tissue into small beamlets through a technique known as spatially fractionated radiation therapy (SFRT) or GRID therapy. In this style of therapy, the healthy tissue in these regions of high dose are heavily damaged, but since the volume of this damaged tissue is relatively small, the unirradiated healthy tissue around these regions

can quickly proliferate and repair the damage. In these styles of treatment, it is important to both keep the high dose volume small [2] and to minimize the dose to the surrounding tissue [3, 4] to maximize the clinical benefit and minimize the recovery time.

1.2 Objectives

This work will investigate several novel methods of administering SFRT and evaluate the dose distributions resulting from the use of these methods for their suitability for clinical application. All methods will have the primary goal of achieving a peak-to-valley dose ratio (PVDR), that is, the ratio between the dose in beam (i.e. the peak dose) to out of beam(i.e. the valley dose), that matches or exceeds the value for conventional GRID treatments. The PVDR is a parameter used to evaluate the quality of the beam definition. The higher the PVDR, the better the beam would perform in terms of normal tissue sparing during the treatment. Each method also has a particular secondary goal in addition to this constraint. The first modality, electron GRID, is intended to allow for the treatment of tumors between the skin surface and radiosensitive organs (also known as organs at risk or OARs), as the limited range of electrons in tissue leads to a significant reduction in the ”exit dose” past the distal end of the tumor. The second, minibeam therapy with photon-emitting radioisotopes, seeks to reduce the beam size to increase the potential radiobiological benefit . Finally, linac-based MV photon minibeam therapy seeks to match the beam size achieved with the radioisotopes while increasing the dose rate to allow for faster treatments.

The dose distributions from each of these methods will be calculated using the Monte Carlo radiation transport code MCNP6[5]. In order to benchmark these simulations, comparable physical measurements were taken using EBT3 Gafchromic film (Ashland, Covington, KY).

1.3 Overview of GRID therapy

1.3.1 History of GRID therapy

Grid therapy is far from a new technique, it was first developed in 1909 by Alban Kohler in Germany [6], and was independently introduced to the United States by F. Liberson [7] in 1933. Initial designs used lead collimators with 1 cm diameter holes, with a spacing to assure the grid gave a 50:50 open to shielded ratio. In both cases, it was developed to address a critical problem with the orthovoltage treatments of the time: skin sparing. [8, 9] Because of the poor depth dose distribution of orthovoltage x-rays, where the maximum dose was deposited at the surface and the dose to deeper tissues dropped off significantly, it was impossible to administer a treatment dose to deep seated tumors without exceeding the skin tolerance and causing highly detrimental biological effects in the healthy tissue. However, by irradiating in an array of beams instead of in a broad open field, healthy tissue was protected from the radiation around each of the beamlets, allowing for centers of regrowth that greatly improved the tissue's ability to recover and therefore the skin tolerance. [10] While the tumor did benefit somewhat from this spatial fractionation of the dose, animal studies conducted by Urano et. al. found that grid therapy increased the tolerance of the skin and other healthy tissue by a factor of 1.8, while the tumor tolerance only increased by 1.23, leading to a gain of 1.5. [11] This difference in the tolerance of the skin and the tumor to treatment is thought to be a result in the different tissue's reaction to the bystander effect, where unirradiated cells will experience similar damage and death as nearby irradiated cells, though the exact biological reason for this difference in response is unknown. [12]

1.3.2 Megavoltage GRID therapy

As accelerator technology advanced and higher energy beams became available, the use of GRID became less necessary as megavoltage beams have a buildup region near the surface

where they deposit relatively little dose. As the percent depth dose curves in Figure 1.1 show, higher energy beams deposit a much smaller percentage of their energy at shallow depths compared to lower energy beams. Because of this, and the development of more advanced treatment techniques such as IMRT and VMAT, GRID was no longer needed for skin sparing for the majority of external beam treatments. However, for large and/or radioresistant tumors, GRID therapy maintains its advantage over these new techniques, such as for melanomas [13, 14], cervical cancers [15], head and neck cancers [16], lung tumors [17], and others [18, 19, 20, 21]. Since the effective treatment of these tumors require large doses in a single fraction, the use of GRID can minimize or avoid any severe radiation induced side effects in the skin at the beam entrance. This is especially important for bulky tumors because of the large field size needed to fully treat these kinds of tumors, meaning that any late effects would encompass a considerable area of skin, and because large tumors tend to be more radioresistant [22].

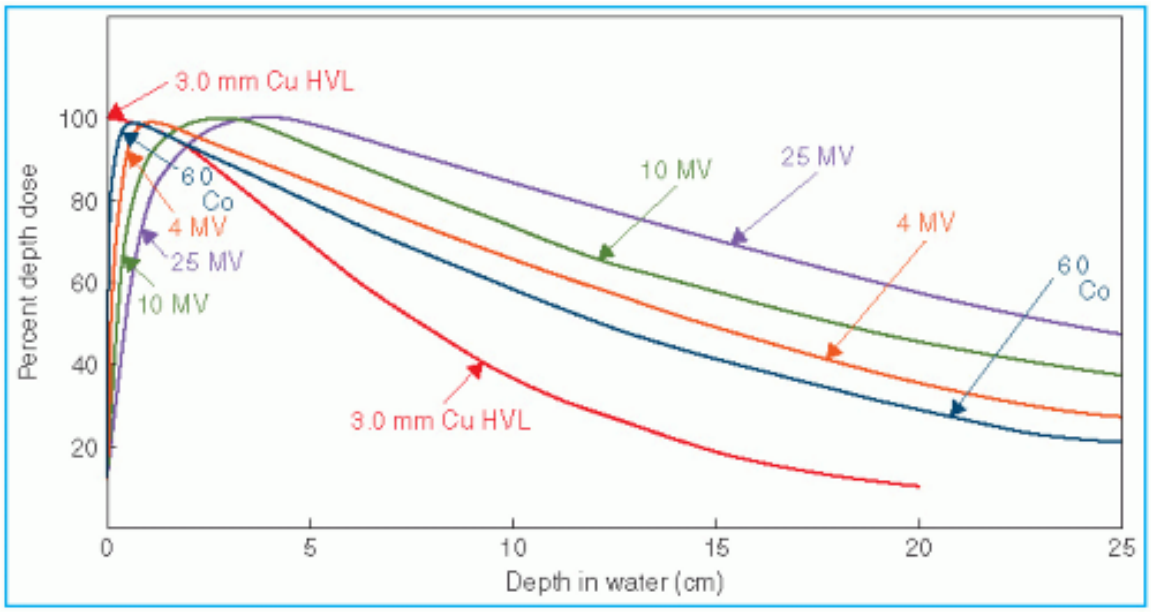

Figure 1.1: Percent depth dose curves from several photon beams of different energies. Br J Radiol. 1978;(suppl 11); and the Appendix.

The specifics of these GRID treatments vary depending on what type of tumor is being treated and which center is administering the treatment, but typically they are administered

using a specially machined block (typically made of brass) [18], or using the multi-leaf collimator (MLC) to create a checkerboard pattern [18, 23], slits [24] or even spheres (for a 3D treatment) [25]. While the exact hole diameters and center-to-center spacings change somewhat between centers, they tend to be around 1 cm and 2 cm respectively (measured at isocenter). [18, 19, 23, 26] The peak dose administered to the tumor also ranges from 10 Gy [19] to 20 Gy [16, 19], but it is always administered in a single fraction. Both of these methods have been found to give similar clinical results, though using the MLC gives the advantage of not having to purchase additional equipment [26]. However, as the MLC can physically only deliver a subset of the holes at a time, using a block decreases the treatment time by a factor of 3-5 and can increase patient throughput [27]. This increase in the amount of beam that needs to be delivered for the MLC treatments has also been shown to decrease the PVDR in some cases due to leakage through the MLCs [18], though other studies show similar PVDRs for both approaches [23].

Overall, GRID treatments have been shown to be effective, both via modeling and in clinical use, for the treatment of a variety of different tumors. In all cases referenced here, GRID was successfully used to administer a large dose in a single fraction with minimal normal tissue effects.

1.4 Radiobiology

As mentioned above, the exact radiobiological mechanisms that underlay the effectiveness of GRID therapy are not well understood [12], even though they can be modeled fairly accurately [14, 28, 29]. One of the most common theories used to explain this phenomenon is what is known as the bystander effect, where irradiated cells release some kind of chemical signal that causes nearby cells to die, even if they were not irradiated [30, 31]. While the exact methods of chemical signaling are not relevant to this work, its effect forms one of the main basis of spatially fractionated radiation therapy. Because of this effect, even when only portions of the tumor are irradiated, a significant amount of cell death still occurs in

the tumor. Because tumor tissue experiences greater bystander effects than normal tissue [32, 33, 34], this gives a radiobiological advantage that allows for preferential killing of the tumor tissue.

Additionally, other studies have shown a strong dependence of normal tissue recovery inversly related to field size, where tissue can recover quickly from being irradiated using a small field (or, as is more likely the case, an array of small fields), even when a high dose is used[2, 35, 36]. In particular, the work done by Hopewell et al shows that once the beam diameter is brought below approximately 5 mm, as can be seen in the reproduced Figure 1.2, the healthy tissue tolerance increases almost exponentially.

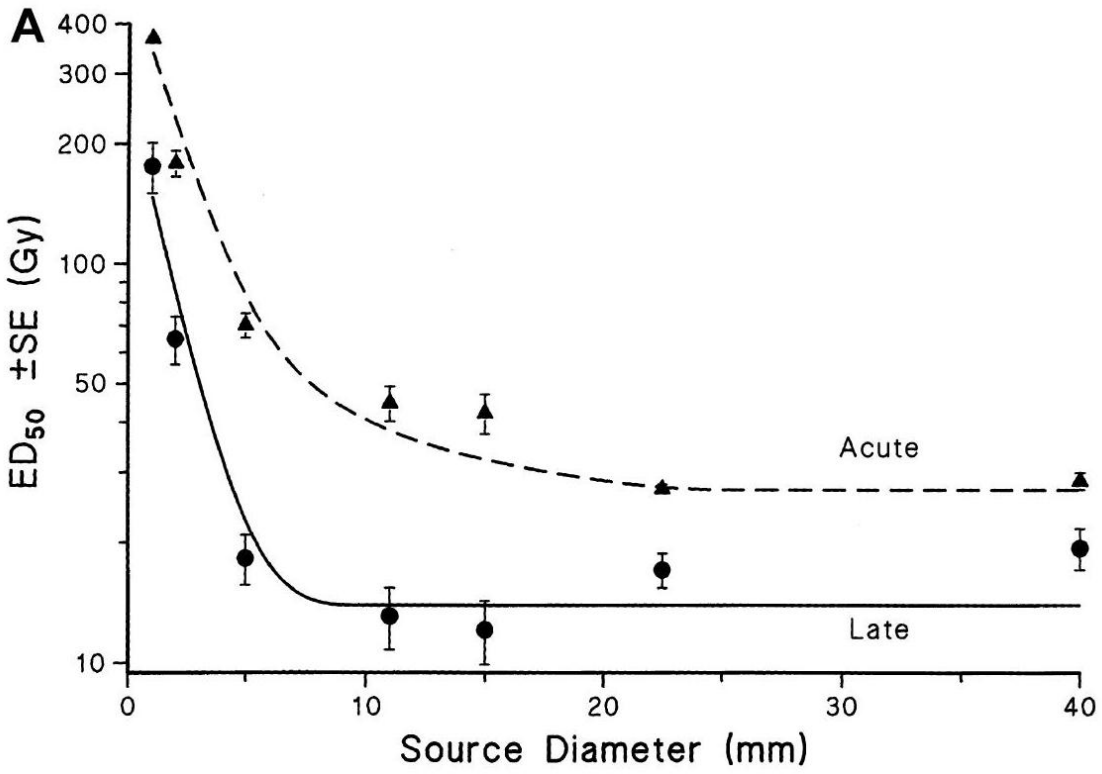

Figure 1.2: Plot from J.W. Hopewell, K.-R. Trott / Radiotherapy and Oncology 56 (2000) 283-288 [2] From the caption "Animal data showing the influence of field size on biological responses in different normal tissues. (A) data for pig skin for: [triangles] the acute reactions of moist desquamation/acute ulceration; and [circles], late dermal thinning after 104 weeks. ..."

This strong correlation is what influenced the latter part of this work, when the beam

size was reduced to 2-3 mm in diameter. However, this effect can be reduced when the surrounding healthy tissue receives some dose, as shown in the work by Bijl et al [3, 4]. In one study, the ED_{50} for paralysis when irradiating rat spines using a 4 mm wide field dropped from 53.7 Gy to 39 Gy when the 20 mm surrounding the high dose field was irradiated with a "shower" of only 4 Gy [4]. This demonstrates that even relatively low doses delivered to the areas surrounding small fields greatly reduces the radiobiological advantage of using these small fields by reducing the healthy tissue's ability to recover.

Also of interest in the same study, the ED_{50} for an 8 mm length of irradiation increase from 24.9 Gy to 45.4 Gy when the 8 mm single field was split into two 4 mm fields separated by 8 mm. [4]. This further reinforces the idea that normal tissue tolerance can be increased by splitting a single large field in to multiple, smaller fields.

1.5 Monte Carlo modeling and MCNP6

The use of Monte Carlo modeling in areas related to medical physics has a long history, with papers on electron transport extending back to 1959 [37] and coupled photon/electron transport going back to 1962 [38]. While the relevant codes have changed over the years, the basic principles governing the radiation transport of these particles have remained fairly similar. [39]

For photons, the process is relatively straightforward compared to electrons, in relation to the relatively few times photons interact with materials when compared to charged particles. As a basic summary, photon transport is generally done in Monte Carlo codes by first generating some path-length to the first (or next) interaction site (generally calculated using a function that includes the mean free path of the photon in the material and a random number). The particular interaction that occurs is then generated by randomly sampling from the probability distribution given by the relative interaction probabilities. Finally, the particulars of the interaction are generated using the relative probability distributions (the scatter angle for Compton scattering using the Klein-Nishena cross-section, for example).

For simple simulations, the energetic electron resulting from the interaction is assumed to deposit its energy locally to eliminate the need to simulate secondaries, though this approximation becomes more and more inaccurate as the photon energy increases and/or the tally volume decreases. [40] Luckily for the photon simulations done in this work, the maximum secondary range is small compared to the dimensions of the tally volumes, meaning this approximation can be used. Regardless, the transport process is repeated for the photon until some termination criteria is met, usually an energy cutoff and/or a geometric limit.

For electrons, the collapsed history approach first introduced by Berger in 1963 [41] has remained relatively unchanged, even through to MCNP6 [5]. Instead of modeling each individual Coulomb scatter event for the electron, something that would quickly become prohibitively computationally expensive, a type of random walk approach is used, where each "step" of the walk includes the contributions from many interactions. In brief, some walk distance is chosen (for MCNP6, this distance is energy dependent, with a larger distance used for higher energy electrons), and the electron is moved this distance through the medium. The energy lost during this distance and the new deflection angle are then generated using the random sampling approach central to Monte Carlo, using a probability distribution generated by the relevant multiple-scattering theory. For example, for energy loss, either the continuous-slowing-down approximation, the fluctuation of ionization loss, or the fluctuation of ionization and bremsstrahlung loss could be used, depending either on the implementation (which may chose a single method for all electrons) or properties of the electron (the the fluctuation of ionization and bremsstrahlung loss would make more sense for a high energy electron moving through a high Z medium due to the significant contribution of radiative losses). [41] Again, this process is then repeated for the electron until it meets some criteria for termination.

As mentioned, by modeling coupled photon/electron transport, it is possible to accurately model the majority of radiation treatment modalities used today (with the notable exception of heavy charged particle treatments, though again these can be simulated in a

manner similar to electrons). In fact, Monte Carlo methods have been used in several treatment planning scenarios, with the main limitation to implementation the calculation time needed by these systems. However, with the development of both faster computers and more efficient MC codes, the use of these types of systems is growing. [42]

MCNP6, or Monte Carlo N-Particle, is a particular implementation of Monte Carlo radiation transport developed by Los Alamos National Laboratory. While not initially developed for use for treatment planning, MCNP has proved effective for a variety of treatment planning cases, including ^{192}Ir brachytherapy [43], ^{60}Co teletherapy [44], and as a double check for a conventional treatment planning system [45], and has been experimentally verified in innumerable other studies. Because of this, MCNP6 is a strong choice of Monte Carlo code for this work.

1.6 Film dosimetry and EBT3 radiochromic film

In cases where high resolution dosimetry needs to be done, such as for small fields or in high-gradient regions of radiation beams, radiochromic film has become the standard tool used to make these measurements. [46] With a spatial resolution down to 25 μm, it is easy to overcome the volume effects and relatively poor resolution encountered when using ion chambers or even diode detectors. GafChromic EBT3 film (produced by Ashland, Covington, KY), the film used in this work, is constructed as a thin active layer sandwiched in-between two transparent polyester bases, as shown in Figure 1.3.

While the film is optimized for doses between 0.2 Gy to 10 Gy, by utilizing all three color channels, the film has a dynamic range of 0.1 to 20 Gy [47], and both limits of this range will be tested in this work.

Due to the small beam sizes used in this work, with the smallest experimental beam having a diameter of only 3 mm, using radiochromic film was necessary to take accurate physical measurements.

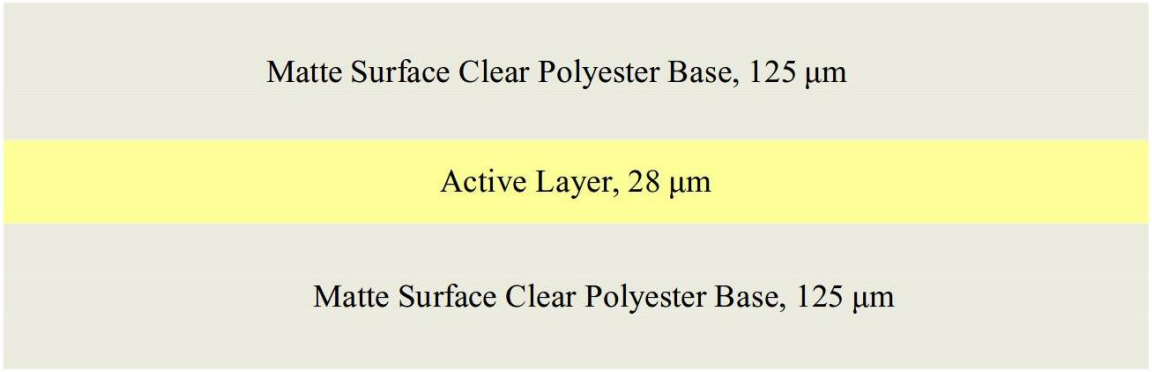

Figure 1.3: Diagram of EBT3 construction, taken from the EBT3 user manual [47]. The active, radiosensative layer is protected by relatively thick sheets of clear polyester.

CHAPTER 2
ELECTRON GRID

2.1 Motivation

While MV GRID has proven to be clinically useful, it still suffers from some limitations that we hoped to alleviate by using electrons. To start, while the skin tissue at the beam entrance tumor is able to recover well from the high dose delivered due to the spatial fractionation, organs behind the tumor may not fair so well. This requires some care be taken when choosing the beam angle, and could prevent the treatment of tumors located near certain OARs. However, electrons, with their limited range, would be able to treat these cases with little worry about exit dose.

Additionally, while MV GRID therapy has shown positive results while leaving some of the tumor tissue unirradiated, clinical outcomes could potentially be further improved if a more uniform dose could be delivered to the tumor while maintaining the spatial fractionation in the healthy tissue on the surface. As electrons undergo significant lateral scattering (compared to photons) uniform tumor dose can be achieved with electrons of the proper energies.

While some past work has been done looking at electron GRID, all these works either looked at lower energies[48, 49] or hole sizes 1.5 cm and larger [50], which would limit the maximum treatment depth and radiobiological benefit, respectively.

2.2 Methods

While working on developing the electron GRID, an initial attempt was made to conduct some Monte Carlo simulations using MCNP6. However, a number of issues made these simulations more time intensive than simply taking physical measurements. To start, elec-

tron transport in MCNP6 is relatively slow due to the large number of interactions that electron undergo compared to neutral particles. While a neutral particle like a photon or a neutron will generally only undergo several collisions or interactions, each of which removes a significant portion of the particle's energy, electrons continuously lose energy as they travel though a large number of Columbic interactions. Typically, these interactions are grouped via the collapsed history approach used by MCNP6, where the expected value of the total energy loss and scatter angle are calculated for all interactions that occurred within some track-length instead of for each individual interaction, which lowers the computational cost of electron tracking. However, due to the high spacial resolution needed for these simulations given the small beam size, this collapsed history distance needed to be reduced such that several of these collapsed history lengths could fit into each voxel. With a voxel size of 0.5x0.5x0.5 mm, this required a small collapsed history length and therefore a large increase in the number of interaction sites that needed to be simulated. This was particularly an issue since the electron source was a linac and therefore had to be placed approximately 100 cm from the phantom surface in order to give an accurate representation of the beam divergence. Even with these approximations, each simulation took almost a month of computer time (and due to how MCNP calculates mesh tallies, they could not be multi-threaded). GEANT4, another Monte Carlo code, has been shown to be somewhat faster for charged particle transport and coul be a better choce for future simulations, but the computational times would still have been long. As such, it was determined that it would be more efficient to simply choose three beam sizes and spacings based on the literature and take measurements using radiochromic film to evaluate the dose distribution. The selected beam sizes were 5, 10, and 15 mm with center-to-center spacings of 10, 20, and 30 mm, respectively. The 15 mm hole size was selected to match the smallest hole sized currently seen in the literature (Meigooni et al[50]), the 10 mm to be in line with the standard MV GRID hole size for a physical collimator [18], and 5 mm to investigate hole sizes smaller than used in current practice.

2.2.1 Experimental measurement

In order to create an array of beamlets, three aluminum collimators were fabricated, each with a different hole diameter, as shown in Figure 2.1.

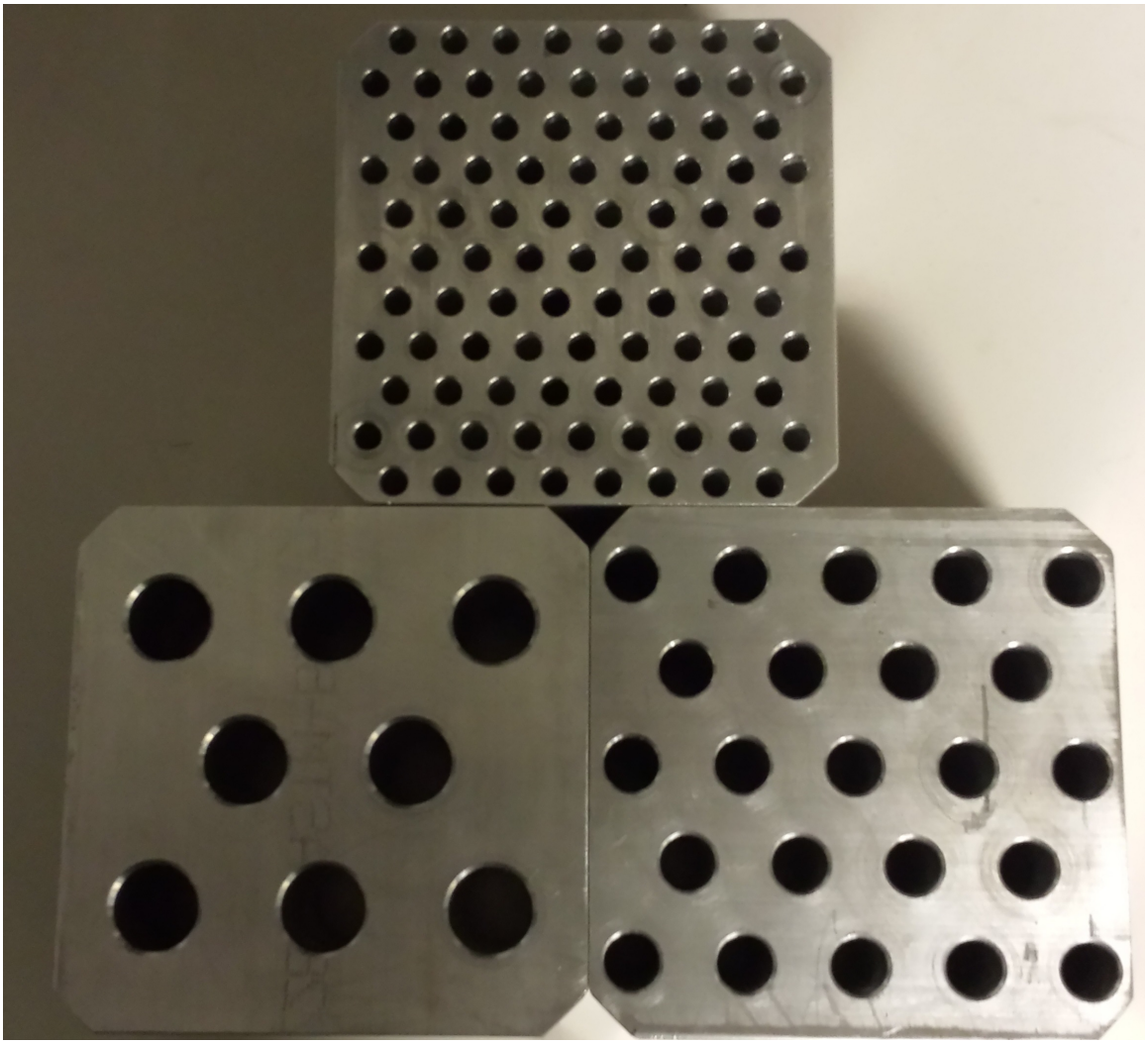

Figure 2.1: Aluminum collimators fabricated for use in film irradiations. Each collimator was made to fit into the 10 cm x 10 cm cone. Starting on the top and moving clockwise, the hole diameters are 5, 10, and 15 mm, respectively.

While cerrobend is typically used for electron cutouts, aluminum was chosen as the collimating material for this case as it is much easier to machine (cerrobend contains several heavy metals, including lead, which cannot be machined in the Georgia Tech machine shop). Additionally, as a low Z material, the use of aluminum also reduced the production

of bremsstrahlung photons. These collimators slotted into the 10 cm x 10 cm electron cone, as can be seen in Figure 2.2.

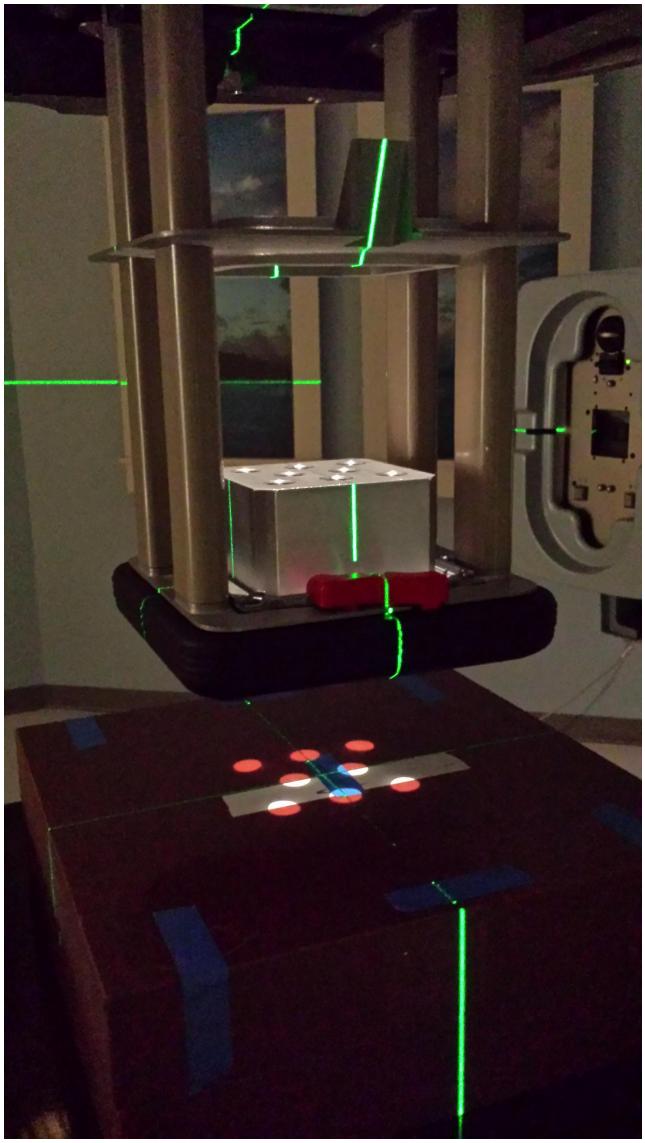

Figure 2.2: 15 mm hole collimator in position for irradiation.

The collimators were designed to have 5, 10, or 15 mm diameter holes arranged in a hexagonal array, with a center-to-center spacing corresponding to twice the hole diameter (10, 20, and 30 mm respectively). Due to restraints on what could be manufactured, the holes were not made to be divergent as is typically used in GRID collimators.

To set up the irradiation, first four, 30x30x5 cm blocks of solid water were positioned

vertically on the treatment couch and aligned along the crossline laser. The accessory mount and the 10 cm x 10 cm electron cone were then mounted onto the treatment head. The elevation of the couch was then adjusted such that the top of the solid water was at 100 cm SSD (source to surface distance). The film was placed vertically in the middle of the solid water such that it extended through the middle of the beam and the top edge of the film was made to be flush with the top of the solid water. The film was attached with painters tape, and marks were made to show the position of the film so that future films could be precisely positioned in the same location, as shown in Figure 2.3. The other half of the solid water was then moved so that it was again flush with the rest of the solid water and tightly sandwiching the film. After a final verification of the alignment, the 0.5 cm diameter hole aluminum collimator was positioned in the electron cone. The film was then irradiated to 600 MU at a rate of 600 MU/min at an energy of 22 MeV. Afterward, the irradiated film was removed and a new film was put into its place. This process was repeated for 18 MeV and 15 MeV electrons and for the 10 mm and 15 mm collimators.

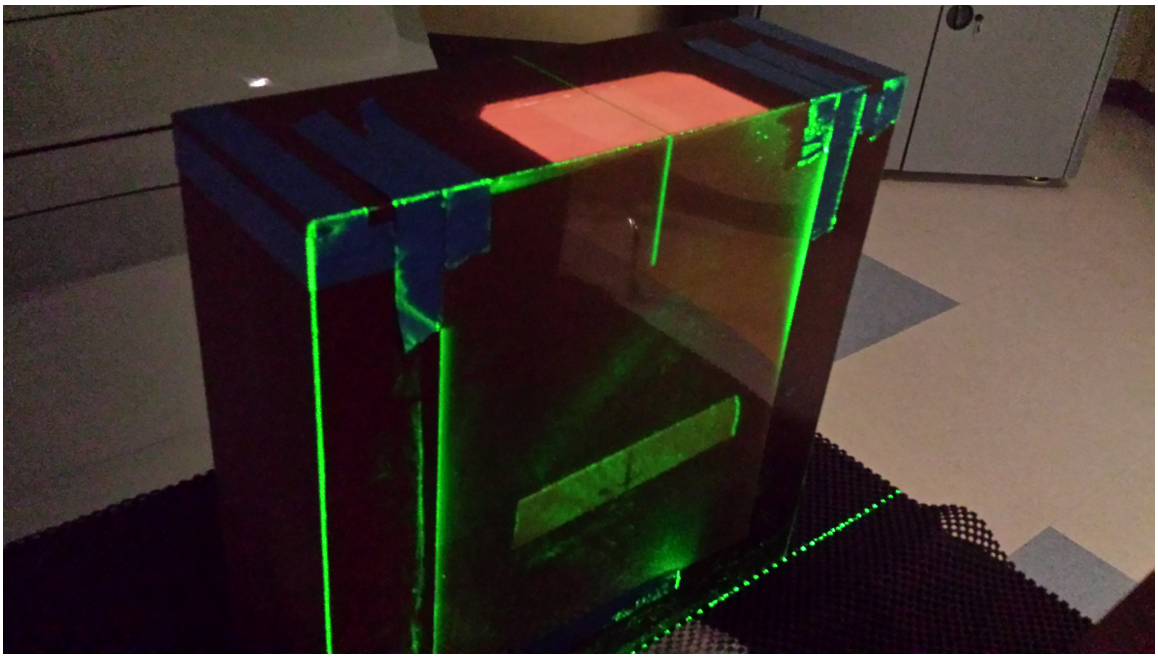

Figure 2.3: Film in position for irradiation with one side of the phantom removed. Solid water on either side provides scatter that one would expect to see in a patient.

The films were then digitized by scanning them using an Epson 11000xl scanner located at Emory University Hospital. A custom MATLAB (MATLAB R2018b, The MathWorks, Natick, 2018) script was used to align and crop the images so they could be more easily compared to each other and to GRID dose distributions from the literature.

2.2.2 Film calibration

In order to relate the change in the optical density (OD) to the absorbed dose in gray (Gy), the film must first be calibrated. While this is a simple process, it must be done for each batch of film as every batch can vary in how it responds to receiving dose. There are different methods for calibrating these films, but the method outlined below was chosen as it was the closest to the experimental setup and used a small amount of film. To calibrate the film, the solid water was arranged in the same geometry as the experimental measurements. For each energy, a film was irradiated with an open 10 cm x 10 cm field to 600 MU at a rate of 600 MU/min. Since films have a slight energy dependence and a non-linear dose dependence, it was important to create a calibration film for each energy and to irradiate them to the same dose as the test films. The films were also digitized using the Epson 11000xl scanner located at Emory hospital. While software does exist to read and analyze film, a custom written MATLAB code was used instead as it made comparisons to the MCNP6 simulations easier. In this setup, the film measurement is highly similar to beam measurements that were taken during the commissioning of the beam (commissioning was done using a water tank instead of solid water, but solid water is a comparable substitute). Because of this, the commissioning percent depth dose measurements (PDD) can be used to determine the dose at any given depth using the MU to Gy conversion formula:

$$Dose(Gy, d) = \#ofMU * Outputfactor * PDD(d) \tag{2.1}$$

Since a 10 cm x 10 cm field was used instead of the calibration field size of 15 cm x 15 cm, an output factor correction is needed, but no other corrections, such as inverse square or off-axis factor, are necessary. Using these known doses, it was then possible to create a calibration curve to convert between OD and dose. OD values were sampled every 3 mm from the film image (corresponding to the data points from the beam commissioning data) and, using the known dose at these depths, a curve was fitted using the vendor recommended equation below [47].

$$d(D) = a + b/(D - c) \tag{2.2}$$

where $d(D)$ is the OD of the film at dose D and a,b,c are fitting parameters.

Because of the slight energy dependence of the response of the film, calibration films were created for each energy used (15, 18, and 22 MeV). Each film was irradiated to the same 600 MU at a rate of 600 MU/min as the experimental films to ensure there was no change in the films response to higher dose levels.

2.3 Results and discussion

Films were exposed using each of the three collimator sizes and using both 18 and 22 MeV electrons. Initially, 15 MeV electrons were also used, but it quickly became clear from a cursory look at the films that the range of these electrons would not be clinically useful. Figure 2.4 shows and example of one of the calibration films and the resulting calibration curve that was used to convert the films from OD to dose.

(a)

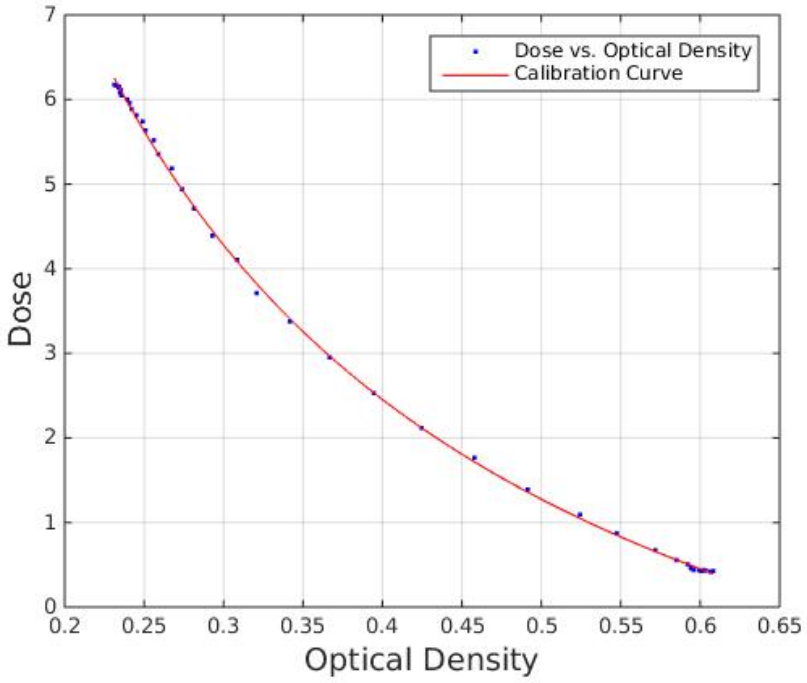

(b)

Figure 2.4: 22 MeV calibration film (a) and the resulting calibration curve (b) using the calibration formula provided by Ashland.

Figures 2.5-2.7 show the results for 18 MeV electrons. For the 5 and 10 mm holes (Figures 2.5 and 2.6, a ”doming” of the dose can be seen because the collimator holes did not follow the divergence of the beam and more electrons could make it through the center holes compared to the holes on the edge. A slight misplacement of the collimator also caused a skew in the dose towards the right of the film. Imperfections in the film at the edge also resulted in some areas being read as negative dose.

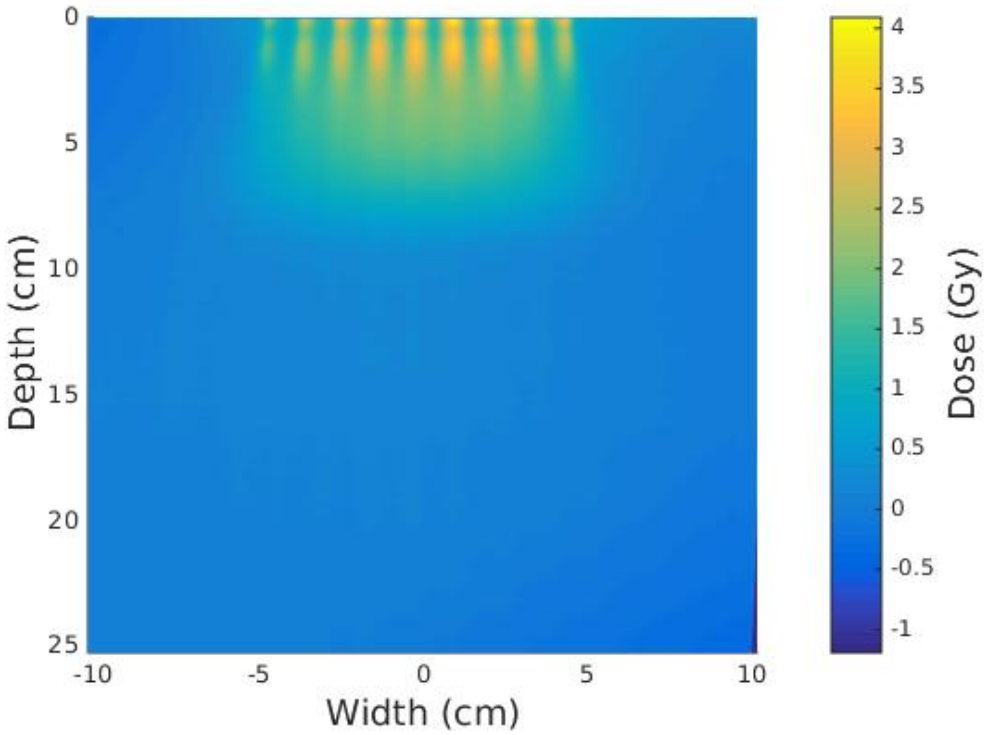

Figure 2.5: Film measurement results from using 18 MeV electrons with the 5 mm hole size collimator.

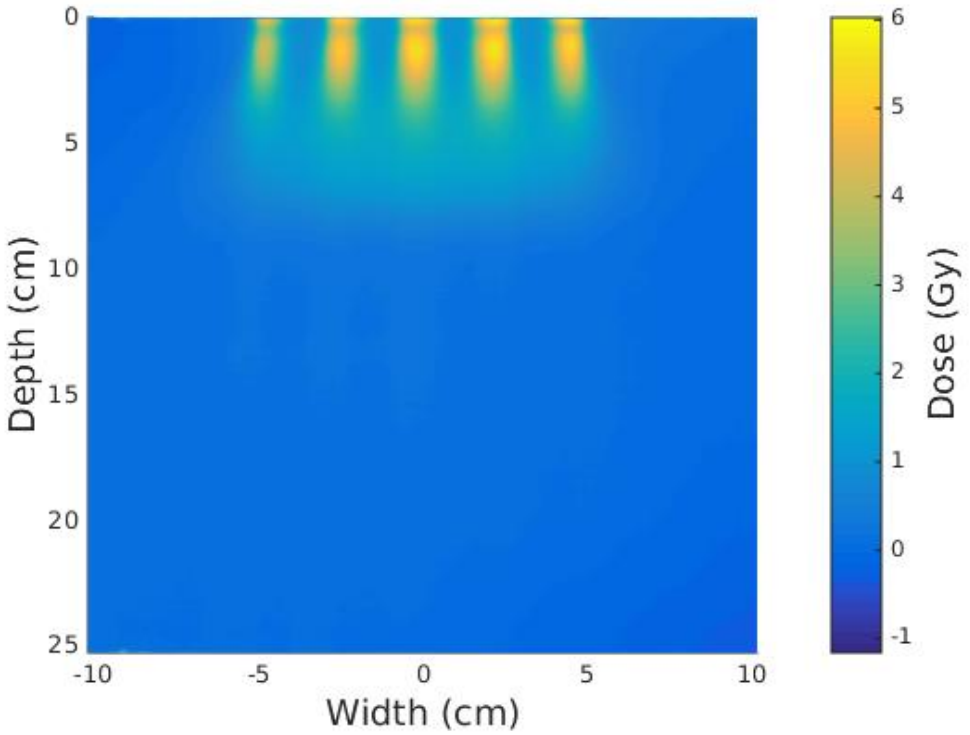

Figure 2.6: Film measurement results from using 18 MeV electrons with the 10 mm hole size collimator.

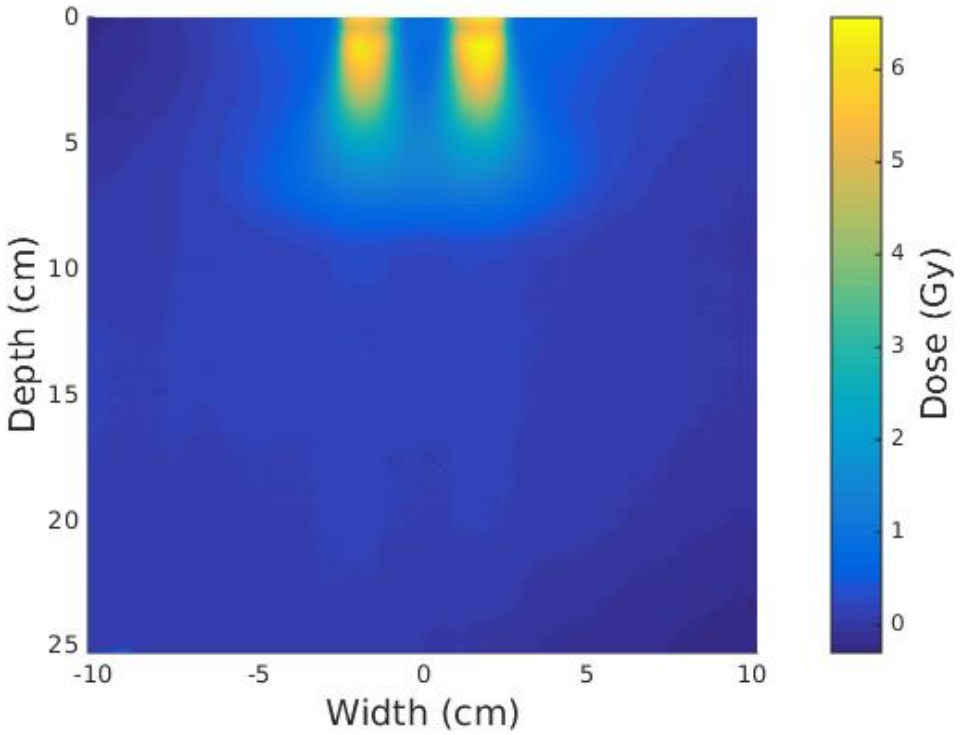

Figure 2.7: Film measurement results from using 18 MeV electrons with the 15 mm hole size collimator.

Figures 2.8-2.10 show the comparable results for 22 MeV electrons, which are similar to the 18 MeV case but with more dose delivered to deeper depths.

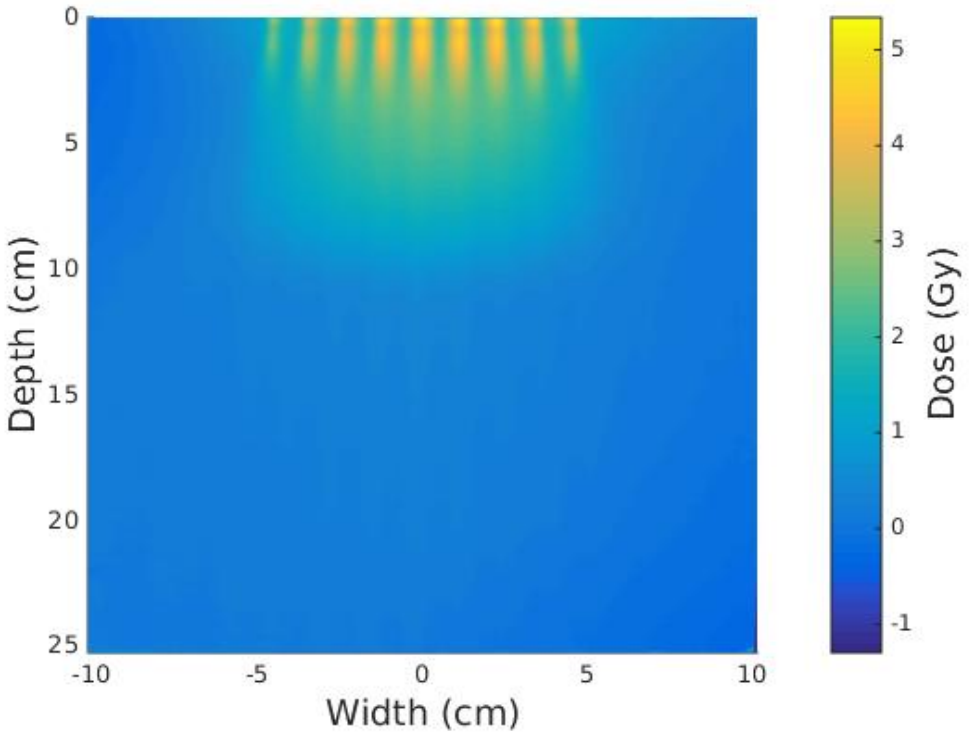

Figure 2.8: Film measurement results from using 22 MeV electrons with the 5 mm hole size collimator.

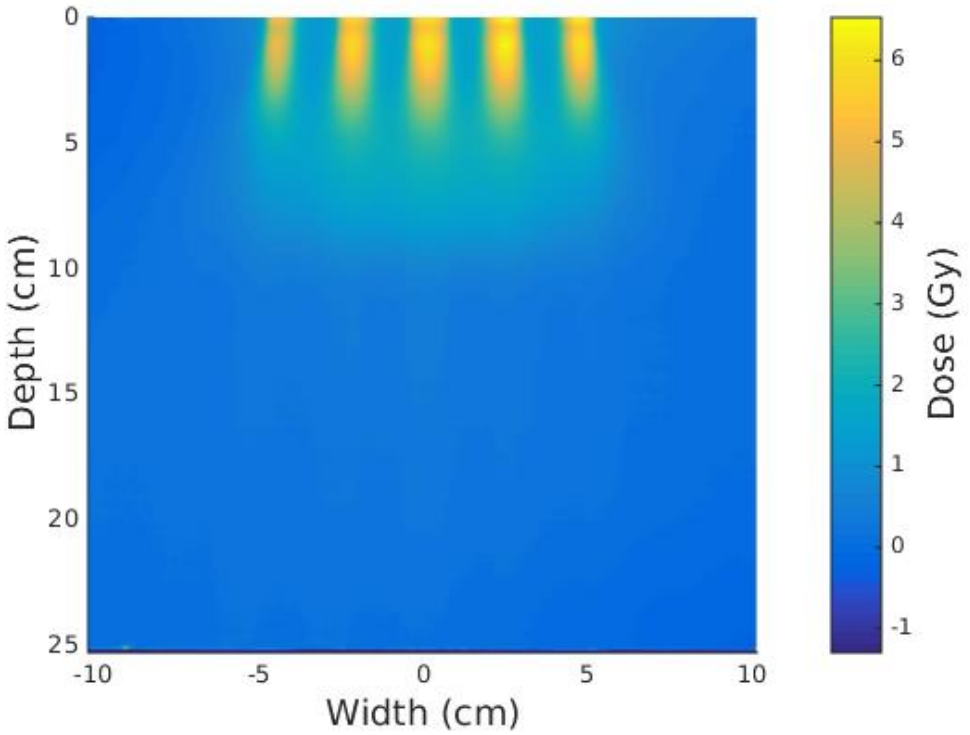

Figure 2.9: Film measurement results from using 22 MeV electrons with the 10 mm hole size collimator.

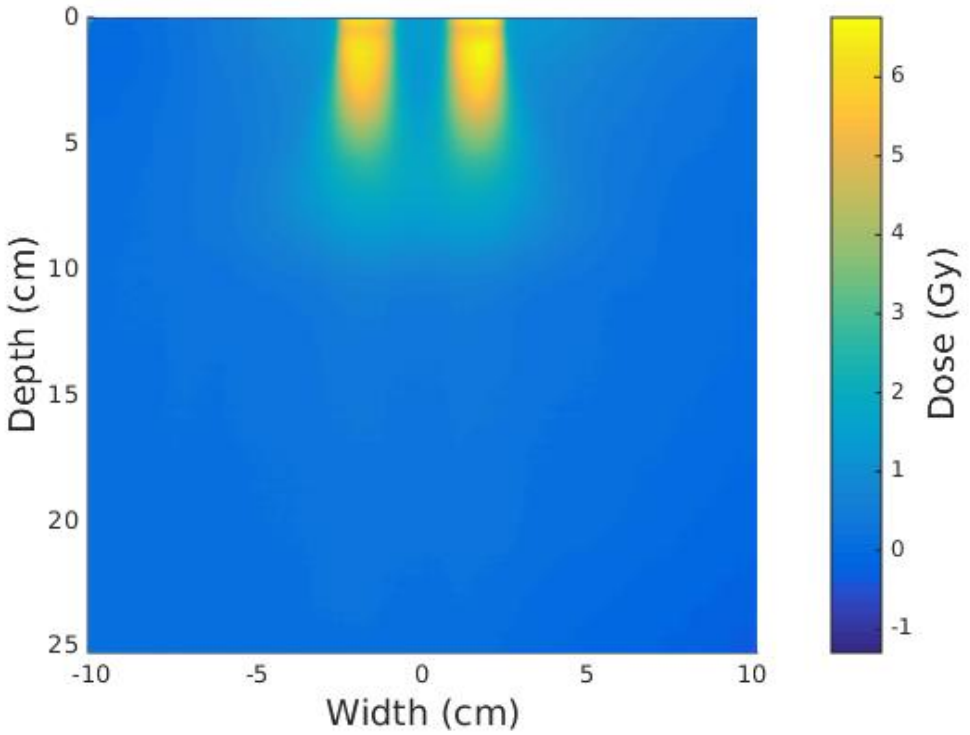

Figure 2.10: Film measurement results from using 22 MeV electrons with the 15 mm hole size collimator.

As seen in Figures 2.11 and 2.12, the smaller hole sizes caused the dose distribution to shift towards the surface when compared to an open beam; D_{80}, depth of 80% dose, is 6 or 7 cm for 18 and 22 MeV electrons respectively for an open beam, while for the 5 mm hole collimator, this is reduced to 1.8 and 2 cm, respectively.

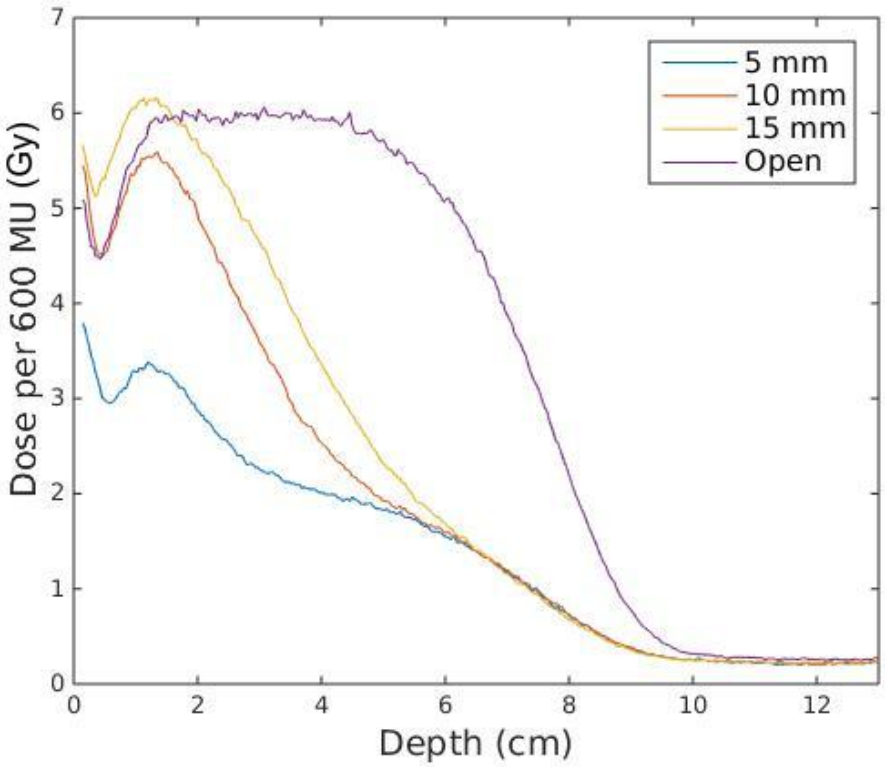

Figure 2.11: Depth dose curves for each collimator compared to the 10x10 open field for 18 MeV electrons. The dose curve for the 15 mm collimator appears to be shifted, which may be the result of a misalignment of the film when it was placed or when it was scanned.

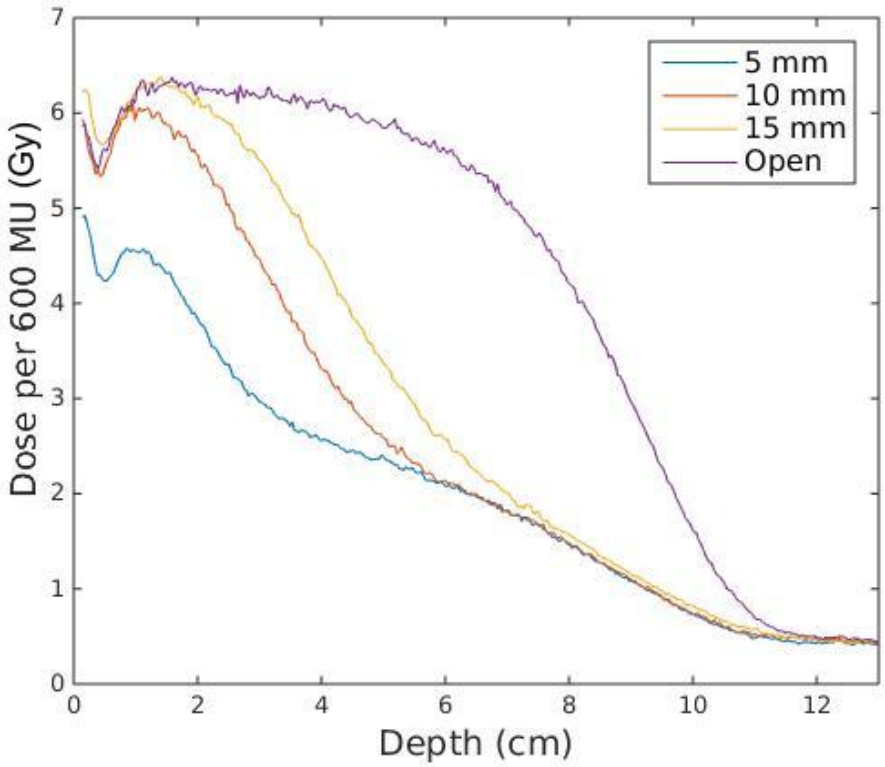

Figure 2.12: Depth dose curves for each collimator compared to the 10x10 open field for 22 MeV electrons.

The doming from the beam divergence and the asymmetry from the misalignment were both greater than expected. In particular, while the positioning of the collimator in the electron cone was precise enough that no misalignment was noticeable during a visual inspection, there was a 30% difference in dose at 2 cm for the 5 mm hole collimator between the rightmost and leftmost beams for the 22 MeV electron beam.

Figures 2.13-2.18 show cross-sectional (crossline) slices of the dose distribution along with plots of the PVDR as a function of depth for the 18 and 22 MeV cases. For all of these, the max PVDR is defined as ratio between the dose rate of the central peak divided by the dose rate of the valley closest to the center, while the mean PVDR is the average dose rate of the peaks divided by the average dose rate of the valleys. The PVDR shows a strong dependence on the beam diameter (or perhaps more accurately, the center-to-center spacing which happens to be proportional to the hole diameter), with relatively low values

for the 5 mm holes (a max of 2.5 and 2.2 for the 18 and 22 MeV cases, respectively) and higher values for the 15 mm beams (7.5 and 5, for 18 and 22 Mev, respectively). In all cases, the highest PVDR appears near or at D_{max}.

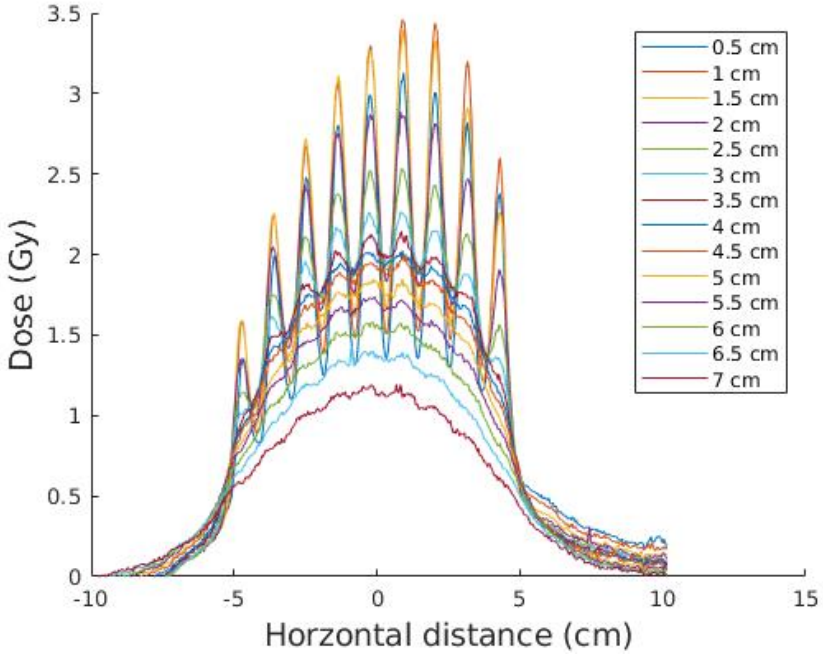

(a)

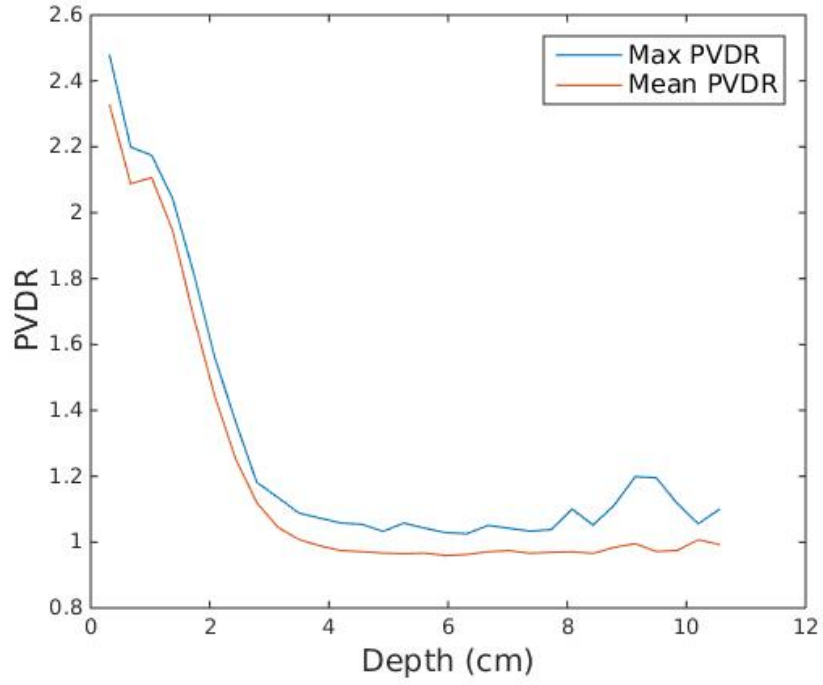

(b)

Figure 2.13: Cross-sectional dose distributions at various depths (a) and the PVDR as a function of depth (b) for 18 MeV electrons through the 5 mm collimator.

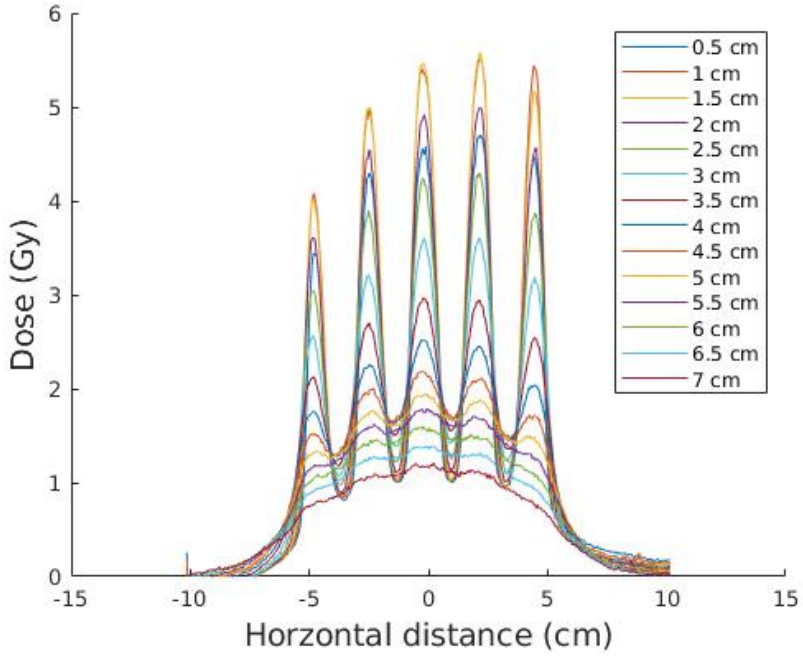

(a)

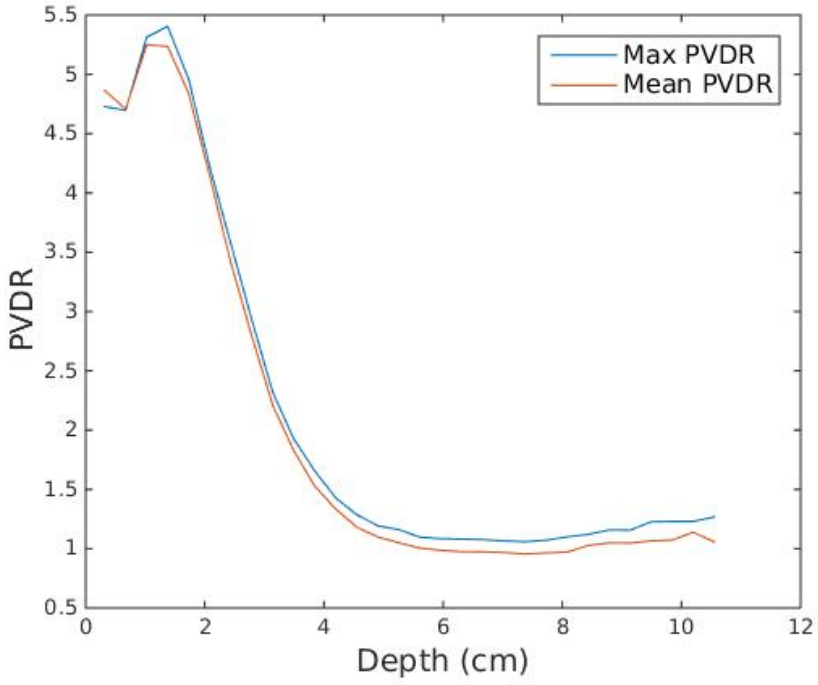

(b)

Figure 2.14: Cross-sectional dose distributions at various depths (a) and the PVDR as a function of depth (b) for 18 MeV electrons through the 10 mm collimator.

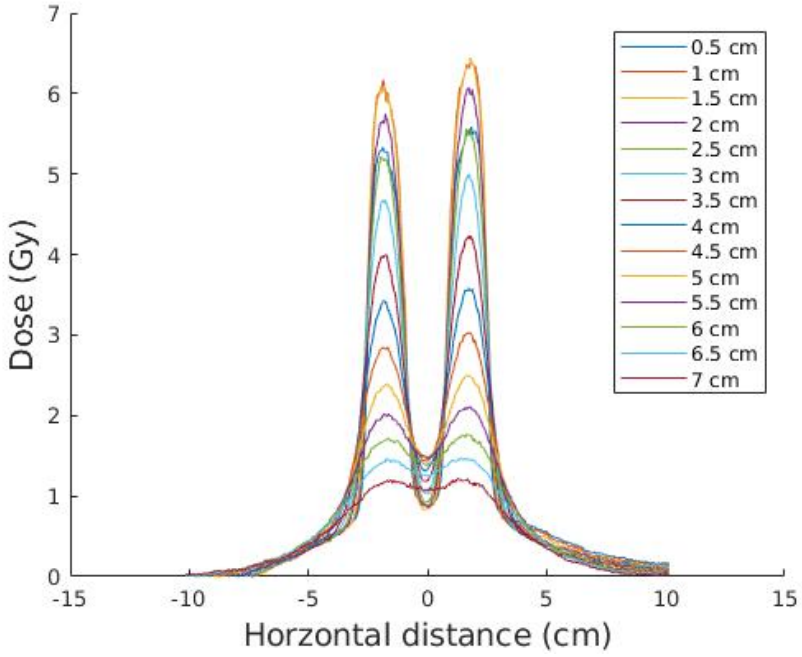

(a)

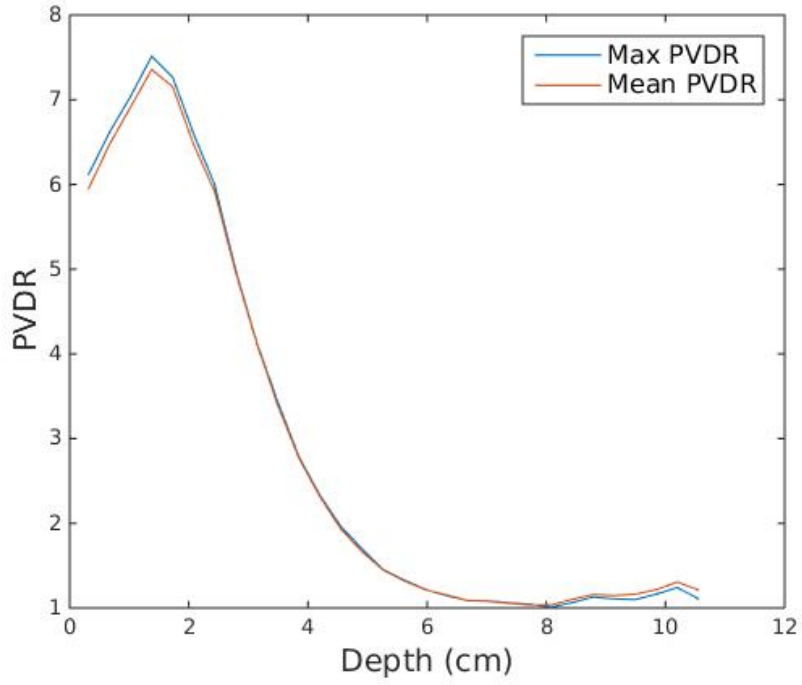

(b)

Figure 2.15: Cross-sectional dose distributions at various depths (a) and the PVDR as a function of depth (b) for 18 MeV electrons through the 15 mm collimator.

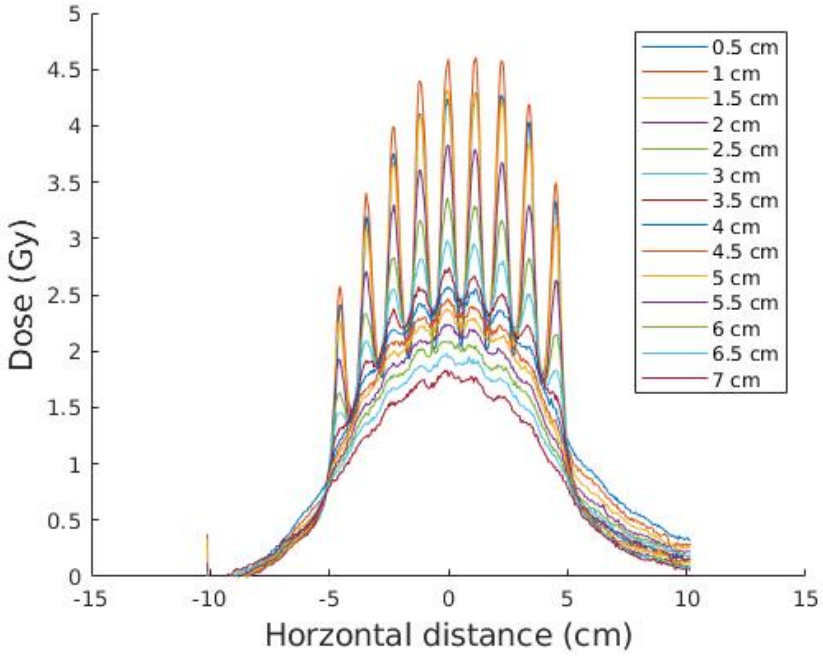

(a)

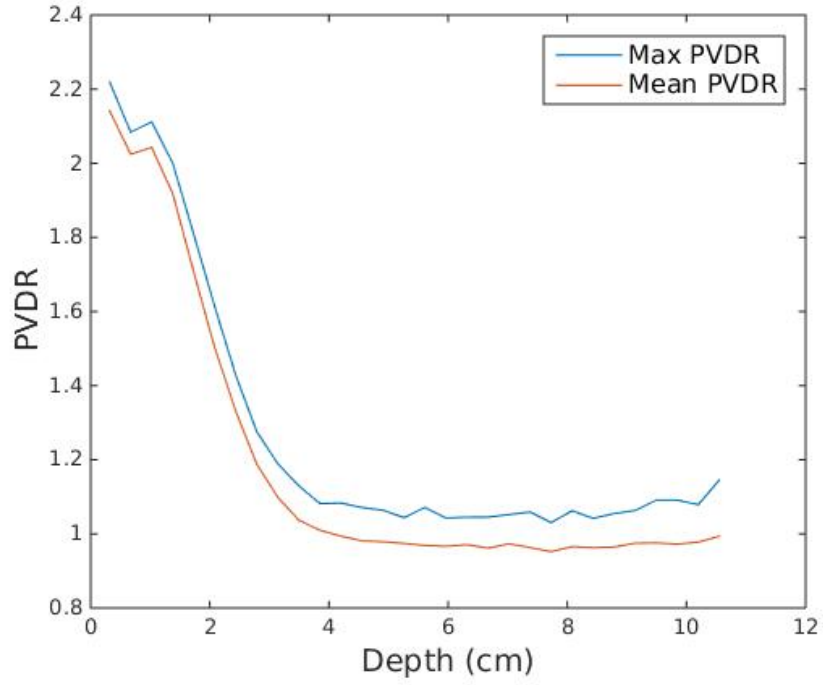

(b)

Figure 2.16: Cross-sectional dose distributions at various depths (a) and the PVDR as a function of depth (b) for 22 MeV electrons through the 5 mm collimator.

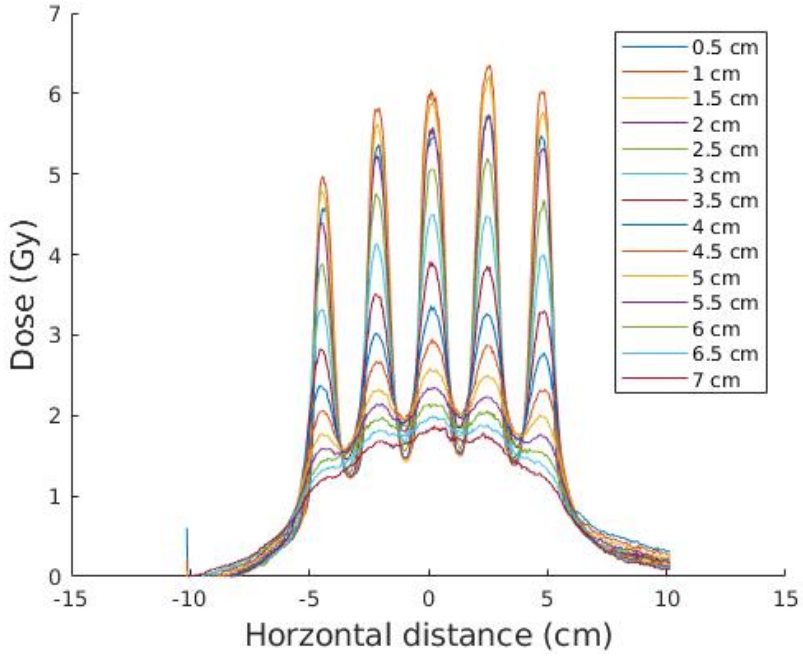

(a)

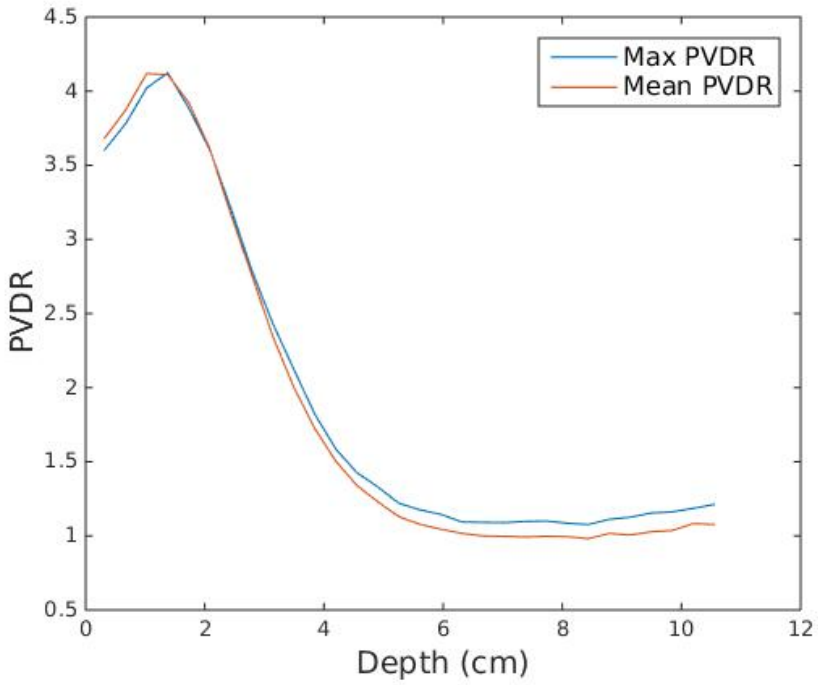

(b)

Figure 2.17: Cross-sectional dose distributions at various depths (a) and the PVDR as a function of depth (b) for 22 MeV electrons through the 10 mm collimator.

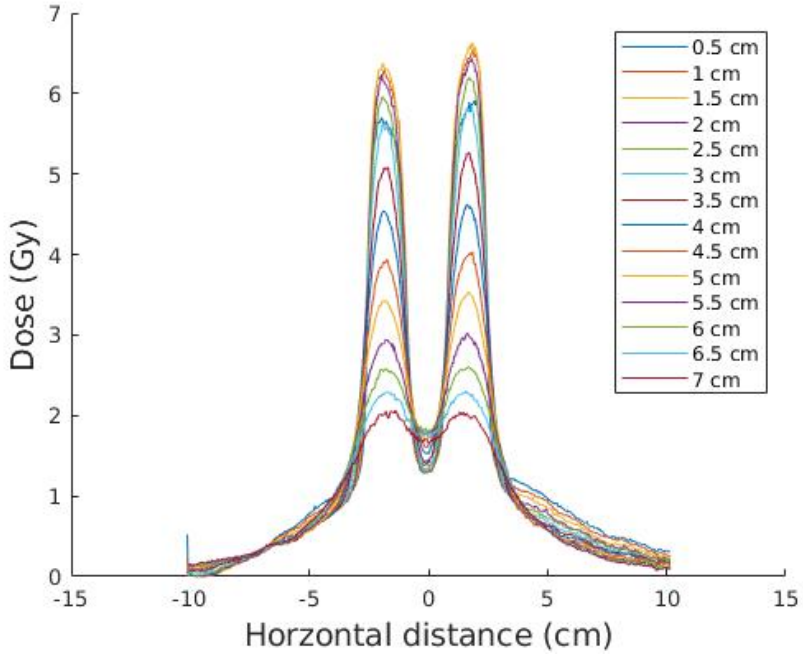

(a)

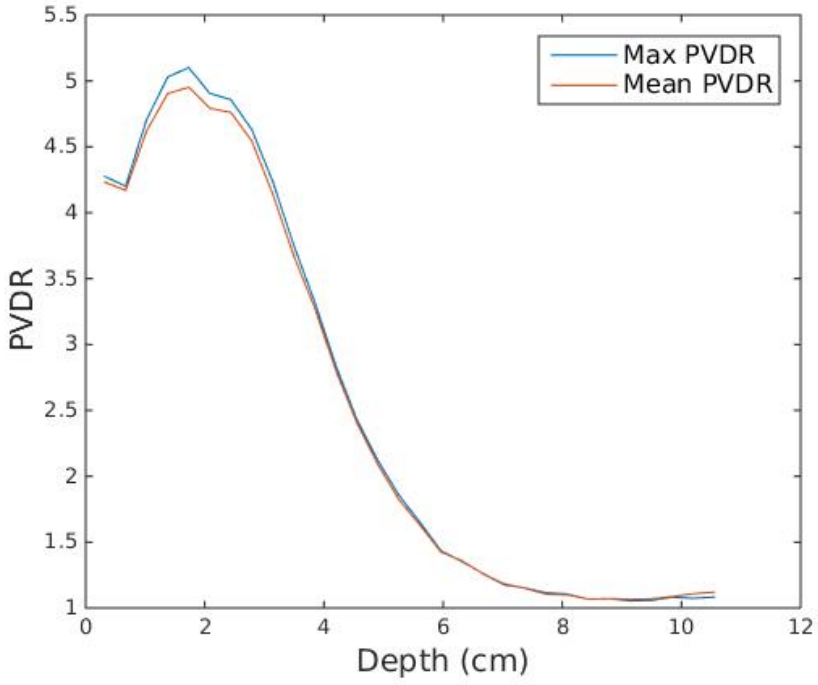

(b)

Figure 2.18: Cross-sectional dose distributions at various depths (a) and the PVDR as a function of depth (b) for 22 MeV electrons through the 15 mm collimator.

From both the cross-sectional and PVDR plots, it can be seen that the electron beams begin to lose definition rapidly upon entering the water phantom, creating a relatively homogenous dose distribution at deeper depths. Even at the surface, the PVDR is fairly low, and only exceeds the PVDR for standard GRID photon treatments (5) in three cases; the 10 mm collimator for 18 MeV and the 15 mm collimator for both energies. The PVDRs for the 22 MeV cases are lower that those for the 18 MeV cases primarly due to the higher valley doses found in the former. This is likely due to increased leakage through the collimator (from electrons deflected to such an angle where they do not pass through the full thickness of the collimator) and/or increase bremmstralung contamination.

2.3.1 Conclusions

While the electron dose distributions perform well in two of the target areas, relatively uniform dose distribution at the target depth and low exit dose, it is unlikely that this method could ultimately be used for clinical treatments. One area of concern is the PVDR; as mentioned, the PVDR is lower than that found in MV GRID treatments for all but a few of the conditions. This alone is not enough to disqualify this method of electron GRID treatment, as clinical experience has shown that MV GRID does show clinical benefit even with PVDRs of only 5, and larger center-to-center spacings could be used to increase the PVDR. However, the dose rate fall-off as a function of depth is also higher for electrons when compared to MV beams, something that would likely be exacerbated by increasing the hole spacing. As a result, the dose rate in-beam quickly (within 5 cm of the surface) becomes comparable to the ”shielded” dose rate at the surface. This would mean that, for any treatment volume that extends deeper than 5 cm, the entire surface would necessarily receive a clinical dose of radiation, which would severely inhibit the recovery effects that are the reason one would use GRID therapy. Considering that GRID therapy is characteristically used for bulky tumors, it is unlikely that a tumor that would benefit from GRID therapy would be less than 5 cm in thickness. This dependance of the effective treatment

depth on the beam diameter also indicated that reducing the beam diameter below 5 mm would not be practical.

It is possible that having a divergent collimator could alleviate some of these issues. The use of a divergent collimator would flatten the dose distribution by reducing the electron loss through the peripheral holes, which also would increase the dose rate at deeper depths. However, to properly match the divergence one would need a separate collimator for each energy and cone size, as the "virtual source point", and therefore the divergance angle, is dependant on both of this factors. Additionally, the collimator could then be made to be somewhat thicker, which could lead to better shielding and therefore better PVDRs near the surface. Creating a collimator with such holes is difficult, however, and the improvements may not be enough to make this clinically useful.

CHAPTER 3

RADIOISOTOPE-BASED PHOTON MINIBEAMS

3.1 Motivation

With the electrons applications limited to highly specific cases, and with the inability to effectively reduce the beam size below the 5 mm diameter limit recommended by Hopewell et al [2], a different radiation source was needed to produce small and clinically useful beams. Photon-emitting radioisotopes seemed to be the best next option for a variety of reasons. First, modern radiotherapy linear accelerators almost never go below 6 MV for their photon energies. With the small beam diameter and center-to-center distances (relative to current MV GRID treatment) the leakage between beams due to energetic Compton electrons would be too high, resulting in poor PVDRs. While lower energy linear accelerators are technically feasible and would give some advantages (explored in the next chapter), we determined that a gamma-emitting radioisotope based approach would be and option. The thought was also that if the isotope system proved to be effective, it could be developed into a treatment system with a low upfront cost when compared to linear accelerators, which could then be used to administer effective radiation treatments in currently underserved areas. Also, from a research perspective, it would be much easier to gain access to a radioisotope source to perform verification measurements compared to a low energy MV system. The physical size of the source could also be set to the same diameter as the collimator hole to easily create a beam of the desired size. As shown in the electron measurements, if the holes in a collimator used with an accelerator do not accurately match the divergence of the beam, the intensity at the edges of the field is greatly reduced relative to the center.

3.2 Methods

3.2.1 Parameter selection

The first, and arguably the most important, parameter that was set was the particular radioisotope that would be used as the gamma source. Due to the limited number of gamma emitters with useful photon energies and reasonably long half-lives, only three main isotopes were initially investigated; Co-60, Cs-137, and Ir-192. While it has been commonly used as a teletherapy source, Cs-137 was quickly eliminated for two major reasons; its low specific activity and radiological safety risk. As the desired beam diameter was only 3 mm, the isotope used must have a high enough specific activity to deliver a clinically useful dose rate even with such a small source size. Cesium, in the commonly used form of CsF, is also relatively easy to disperse, making it a less than ideal source from a radiological safety standpoint. While cobalt has a higher specific activity than cesium, its high energy photons make shielding requirements are significantly higher compared to the other two sources. This is particularly an issue with regards to the collimator thickness in the direction of the patient. More collimator material is needed in order to adequately shield the regions out of the beams, but the further the sources are moved from the patient, the lower the beam intensity (and therefore the dose rate) due to the $1/r^2$ drop off. The high energy photons would also lead to poor PVDRs. Despite these disadvantages, ^{60}Co, it was still considered as a viable option. ^{192}Ir's high specific activity was predicted to give a high dose rate even with a physically small source, though its correspondingly short half life would necessitate frequent replacement of the sources in a treatment device. The major advantages of ^{192}Ir are from its relatively low mean gamma energy of approximately 350 keV, which requires much less shielding and also leads to higher PVDRs.

With the sources set, it was then possible to start investigated other necessary parameters, such as the collimator material and thickness, and the center-to-center spacing of the beams. To predict the effects of changing these various parameters on the resulting

dose distributions without needing to physically construct a wide variety of collimators, MCNP6 was used to model various conditions. To further decrease the number of variables that needed to be changed, the collimator hole diameter was set at 3 mm (though this was later changed to 2 mm) and the source thickness was set such that self attenuation was capped at 50%; that is, that half of the photons produced in the top of the source would be expected to make it through the source into the collimator holes. This corresponded to a thickness of 2 mm and 15 mm for the ^{192}Ir and ^{60}Co sources, respectively.

3.2.2 MCNP simulations of isotope minibeams

3.2.2 Parallel minibeams

The geometric configuration of the parallel minibeams and the water phantom included in the MCNP6 simulations is shown in Figure 3.1. As shown, there are seven minibeams with their corresponding sources arranged in a hexagonal geometry. The source and the collimator hole have the same diameter of 3 mm. In order to compare different collimator designs, each design was assessed based on its PVDR at the surface and its dose rate at a depth of 10 cm. As a minimum requirement, the collimator would have to allow a dose of 20 Gy to be delivered to a depth of 10 cm while not exceeding a dose of 1 Gy in the valley region at the surface. This requirement was based on a combination of the maximum single fraction dose typically used in standard GRID therapy and the study by [4] showing decreased tissue recover for valley doses above 1 Gy.

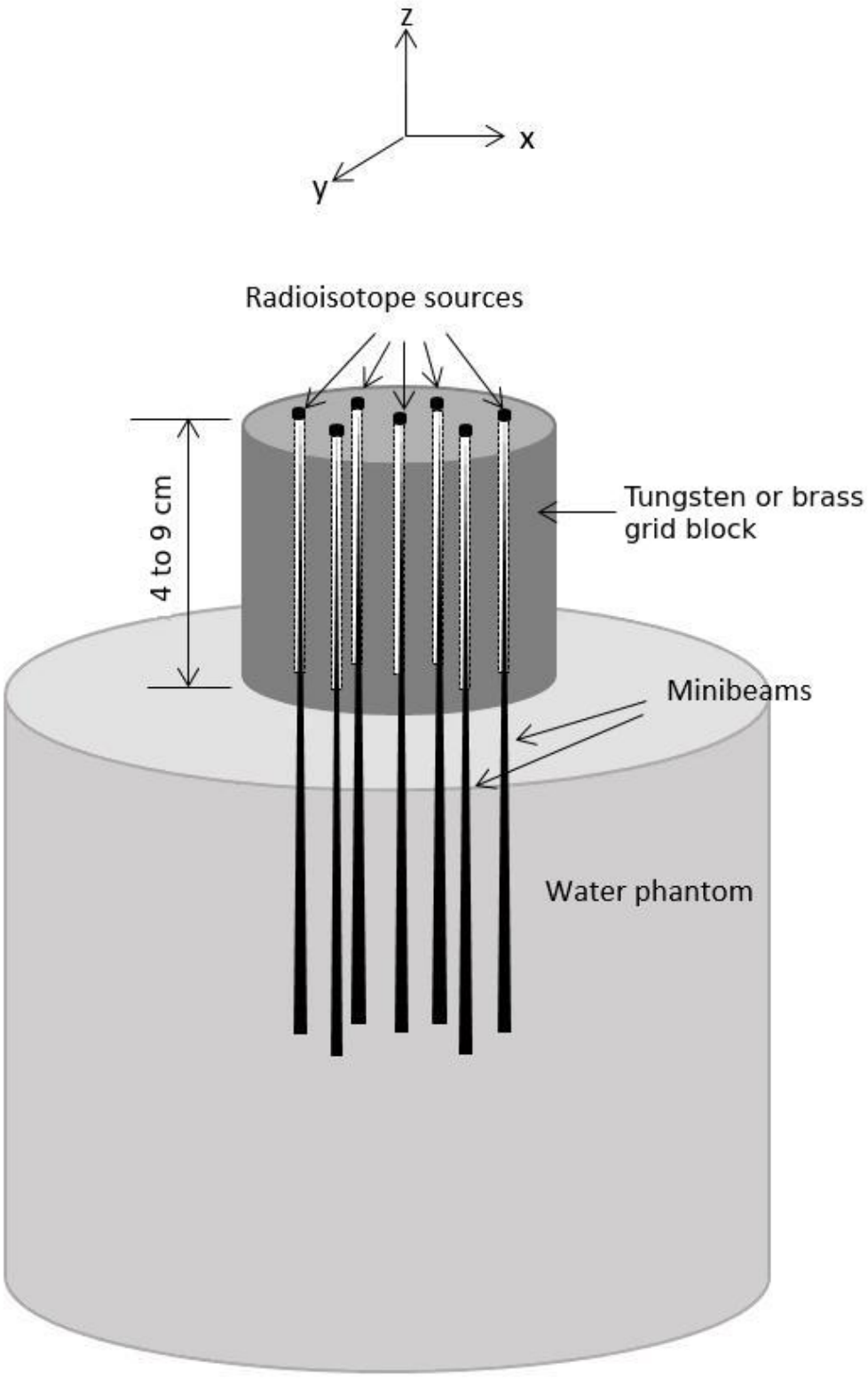

Figure 3.1: The geometric configuration of the parllel minibeams and the water phantom that were included in the MCNP6 simulation.

Initially, all simulations were done using a type 3 superimposed mesh tally, which measured the energy deposited in an array of $0.5\times0.5\times0.5$ mm voxels (units of MeV/cm^3/source particle) which could be easily converted to a dose rate (using the density of water and the activity of the source, this can be converted to Gy/min using the Equation 3.1.

$$\dot{D} = M * \rho * A(Ci) * 3.7 \times 10^{10} \frac{Bq}{Ci} * y * 1.60218 \times 10^{-13} \frac{J}{MeV} * 1000 \frac{g}{kg} * 60 \frac{s}{min} \quad (3.1)$$

Where M is the tally result, ρ is the density of the tally material, A is the activity in Curies, and y is the mean photons per decay of the radioisotope.

Because of the radial symmetry of the collimator, only two beams needed to be simulated per collimator; one in-plane and one out-of-plane (i.e. the solid beams shown in Figure 3.2). The other beams could then be accounted for using shifts corresponding to the chosen center-to-center distance. While this approach gives an excellent visualization of the dose distribution, it has significant drawbacks. Because of the small size of the voxels needed to give sufficient spatial resolution to adequately represent the lateral dose profile of the minibeams, a large number of particles need to be run to reduce the uncertainty to an acceptable level, especially in the valley region. Since this would require an unacceptable amount of computer time, a different approach was needed in order to optimize the collimator parameters.

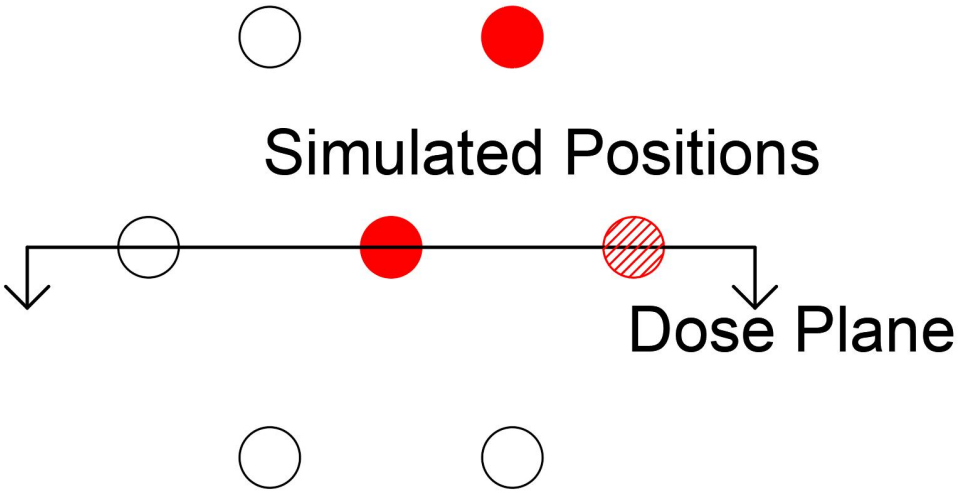

Figure 3.2: Cross-sectional view of simulated beam geometry at the source plane. Solid beams were simulated for both the parallel beam and converging beam geometries, while the hashed beam was additionally simulated for the converging beam geometries.

Again making use of the radial symmetry of the collimator, a series of concentric ring tally volumes (with radii corresponding to half the source radius, half the center-to-center distance, and the full center-to-center distance) were used at specific depths instead of using the superimposed mesh. Using this geometry, 10 collimator thicknesses (4 to 9 cm, steps of 0.5 cm) and 8 center-to-center distances (6 to 14 mm, steps of 1 mm), and two collimator materials (tungsten and brass) were investigated, for a total of 160 combinations. In addition, F6 (i.e. kerma) tallies were used instead of +F6 (i.e. the absorbed dose tally) in the valley region. The combination of using larger tally volumes and F6 tally drastically reduced the uncertainty of the valley dose from 40% to approximately 3% with 10^7 particle histories. The use of F6 tally was justified by the fact that the range of the Compton electrons is mostly shorter than the tally size.

3.2.2 Convergent minibeams

The geometric configuration of the convergent minibeams and the water phantom that were included in the MCNP6 simulation is shown in Figure 3.3. In this simulation, the same

collimator thickness and material were used as in the parallel beams. However, a new center-to-center distance was needed to account for the new beam orientations. For the convergent case, the premature intersection of the beams due to the beam divergence was more of a concern when picking the center-to-center distance than the PVDR. Since the effective center-to-center distance changes as a function of depth for the convergent beams, the ring volumes used in the previous geometry needed to be modified to account for this. Two additional tally volumes were also included, one at 9.5 cm and one at 10.5 cm, to verify that the highest dose rate was indeed being delivered to the target depth of 10 cm. A diagram of this geometry can be seen in Figure 3.3. Again, taking advantage of the symmetry of the problem, only three beams needed to be simulated to calculate the full dose distribution: the central beam , an on-plane diagonal, and an off-plane diagonal (i.e. the two solid and one hashed beams shown in Figure 3.2).

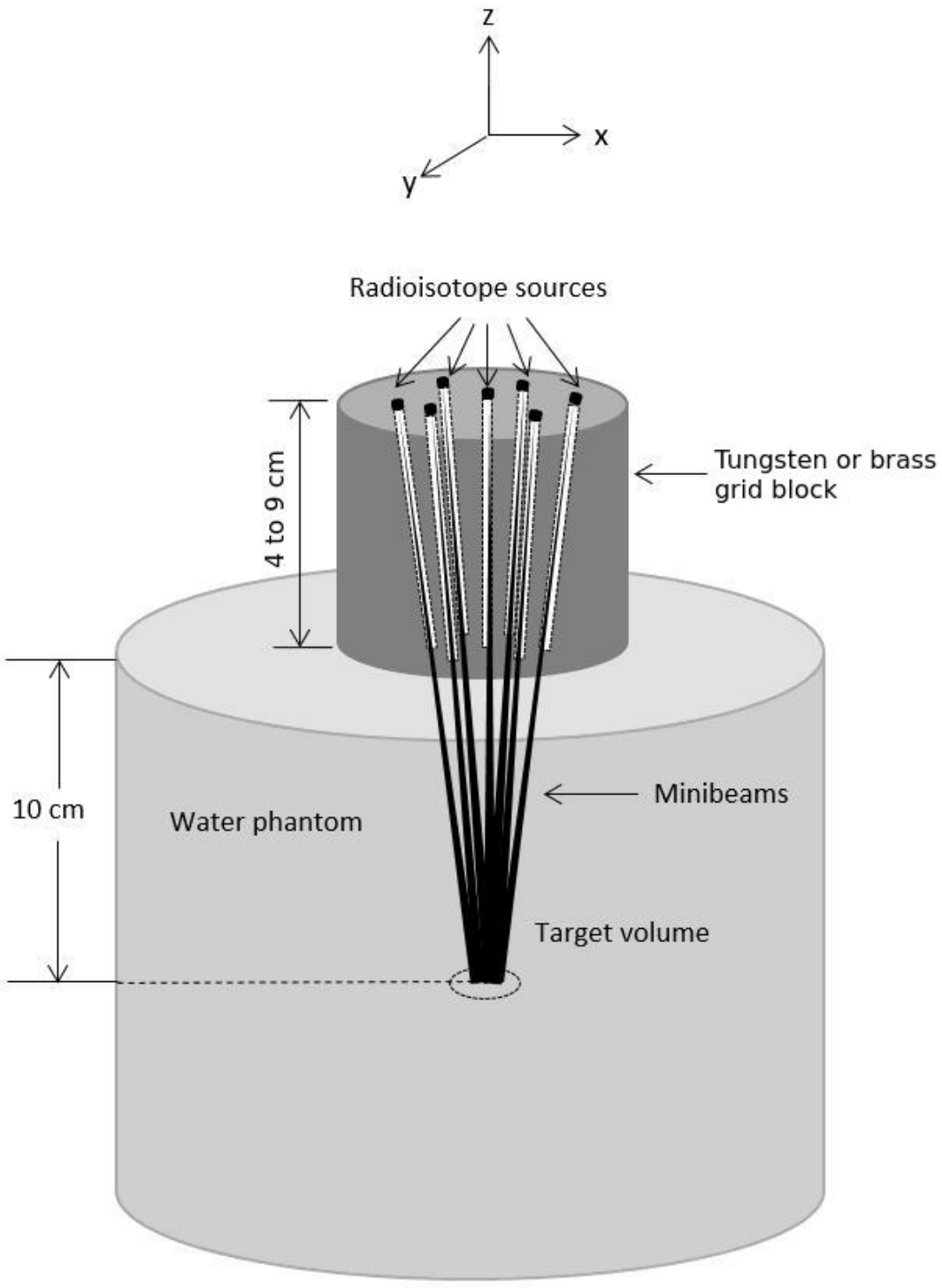

Figure 3.3: Convergant geometry collimator. As with the parallel case, the collimator thickness, center-to-center distance, and hole diameter were all varied throughout the course of this work.

3.2.3 Maximum achievable activity

One important parameter for determining the dose rate is the maximum achievable activity, or MAA, of the sources. ^{192}Ir is produced by exposing ^{191}Ir to a high thermal neutron flux in a nuclear reactor. Because a non-negligible fraction of the ^{192}Ir produced will decay or be converted to ^{193}Ir while the source is still being irradiated, the MAA for ^{192}Ir corresponds to when the production rate and the depletion rate of the ^{192}Ir are equal. The amount of ^{192}Ir present in a source can be calculated as a function of irradiation time and neutron flux using Equation 3.2:

$$\begin{aligned} N_{192}(t_i) &\cong N_{192}(t_{i-1}) + N_{191}(t_{i-1})\sigma_{191}\phi_n\Delta t - N_{192}(t_{i-1})(\lambda_{192} + \sigma_{192}\phi_n)\Delta t \\ &= N_{191}(t_{i-1})\sigma_{191}\phi_n\Delta t + N_{192}(t_{i-1})\left[1 - (\lambda_{192} + \sigma_{192}\phi_n)\Delta t\right] \end{aligned} \tag{3.2}$$

Where N_{191} and N_{192} are the number of atoms of ^{191}Ir and ^{192}Ir, respectively, at a given time point, either the previous time step t_{i-1} or current time step t_i with a step length of Δt, σ_{191} and σ_{192} are the microscopic thermal absorbtion cross-sections of ^{191}Ir and ^{192}Ir, respectively, and λ_{192} is the decay constant for ^{192}Ir.

Using Equation 3.2, one can find the MAA and necessary irradiation times for the thermal neutron fluxes found in various isotope production reactors. While Equation 3.2 is also applicable to convert a sample of Co-59 to Co-60, the time needed to reach MMA for ^{60}Co is too long to be practical. This is mainly due to the long half life of 5.2 years for ^{60}Co. Because of this, the maximum irradiation time for producing high activity ^{60}Co sources was set to sixty days.

3.2.4 Shielding calculations

As an exercise to demonstrate the feasibility of storing such high activity sources in a hospital, simulations were done to find what size of lead pig would be needed to reduce

the dose rate to below 5 mrem/hr one foot (30 cm) from the surface of the container. This level was chosen as it is the threshold for an area being classified as a radiation area. The more conservative public dose limit of 2 mrem/hr was not used as it was assumed anyone entering the room would be hospital personnel with personal dosimetry or a patient who is about to undergo treatment. An F5 tally was used to minimize the computational time needed to run the shielding simulations.

3.2.5 Physical measurements

To try to verify the ^{192}Ir simulations, physical measurements were conducted using an ^{192}Ir HDR source at Cancer Centers of America's facility in Newnan, Georgia to compare against MCNP6 simulations of the same geometry using the same tally types and the same source parameters (where applicable). The HDR system was a Varisource iX (Varian, Palo Alto, CA) Two tungsten collimators were fabricated (that is, 3 mm holes were bored through two pieces of tungsten), each with a thickness of 3 cm. From the simulation, a single piece of tungsten was deemed sufficient to produce a nicely collimated beam, and the use of a single collimator eliminated the potential error from a misalignment. By attaching a guide tube to the collimator, it was possible to position the source above the hole to approximate the geometry of the proposed GRID collimator design. The dummy source from the afterloader was used to find the source position needed to center the source above the hole. The actual experimental setup is shown in Figure 3.4.

Using the dose rates obtained from the simulation, the source was placed in the active position (that is, centered above the collimator hole) for a total of 7792 seconds, which was calculated to deliver 20 Gy to D_{max}, the maximum dose to which the film was sensitive. This was done to maximize the dose in the valley region in an attempt to bring it above the 0.1 Gy minimum detectable dose limit in as many areas as possible.

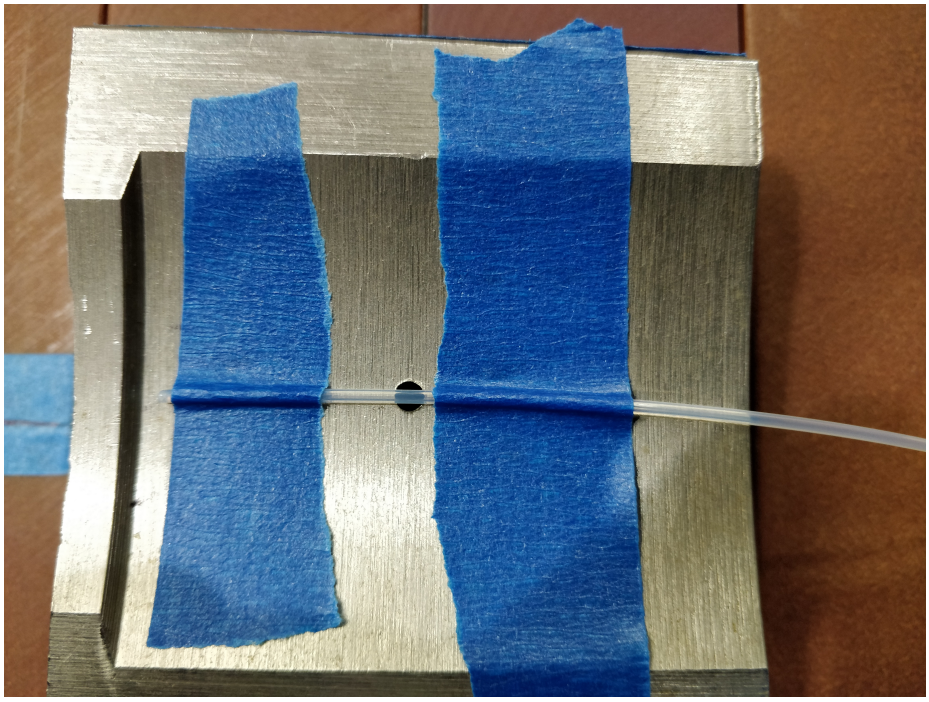

(a)

(b)

Figure 3.4: Set up for the ^{192}Ir measurements. (a) shows the alignment of the HDR guide tube with the 3 mm diameter hole in the collimator. (b) shows a zoomed out view of the setup, including the afterloader.

The OD of the film was converted to dose using the commercial software FilmQA Pro (Ashland Inc., Covington, KY). A set of 7 calibration film strips were produced using the Varian iX linear accelerator at Georgia Tech, using doses of 0.0, 0.5, 1.0, 4.0, 8.0, 16.0, and 20.0 Gy. These values were selected both to cover the full range of doses expected on the experimental film and to increase (roughly) exponentially to provide better data points for the fit. The OD to dose conversion formula is below:

$$d(D) = a + b/(D - c) \tag{3.3}$$

where $d(D)$ is the OD of the film at dose D and a,b,c are fitting parameters.

Figure 3.5 shows the calibration process, with the calibration film loaded into FilmQA Pro. As can be seen in the figure, each color channel has a different response function. In general, the red channel is the most accurate for low doses, the blue channel for high doses, and the green for doses between the two extremes.

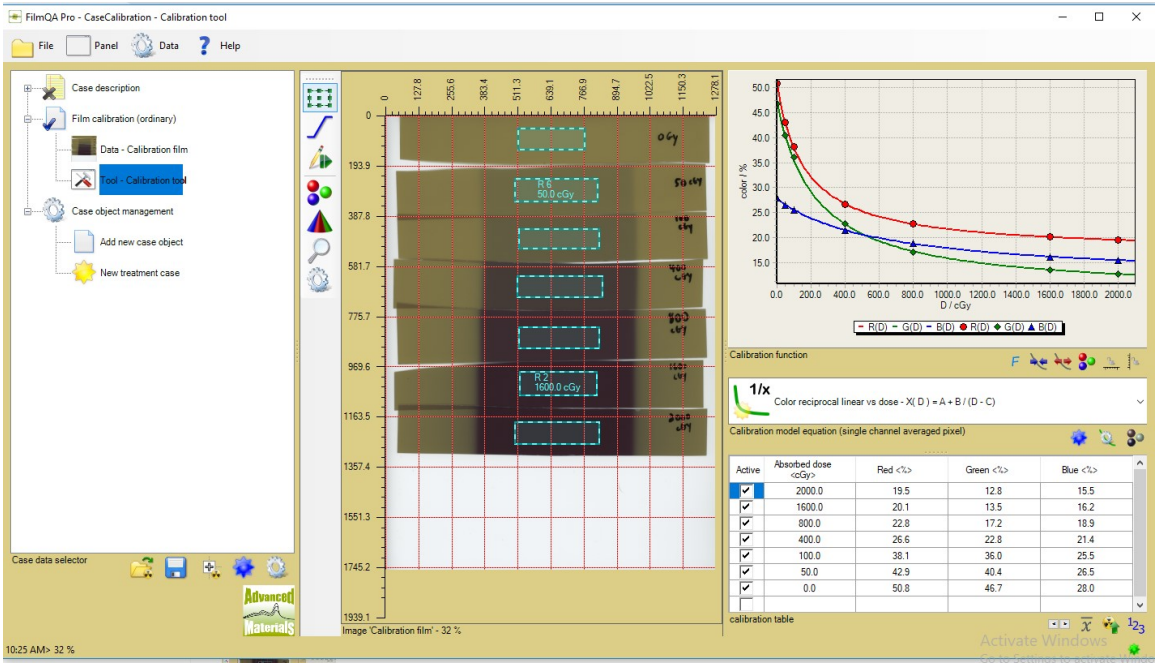

Figure 3.5: Calibration film loaded into the film reading software FilmQA Pro. The center window shows the calibration film which provides 7 calibration points used to generate the functions shown on the right.

3.3 Results

3.3.1 Ir-192 minibeams

3.3.1 Maximum achievable activities

Figure 3.6 shows the time-dependent growth and depletion of the quantities of ^{191}Ir and ^{192}Ir inside a nuclear reactor based on a flux (ϕ_n) of 1.0x10^{15} neutrons cm^{-2} s^{-1}. As shown, t_{max} for ^{192}Ir is around 230 hours (9.5 days). Table 3.1 shows the MAAs cm^{-3} of ^{192}Ir for ϕ_n ranging from 1.0x10^{14} to 2.0x10^{15} neutrons cm^{-2} s^{-1} as well as the corresponding t_{max}. As shown, both the MAA and the corresponding t_{max} vary with ϕ_n. Specifically, the MAA increases as ϕ_n increases and it is also achieved with a shorter irradiation time, t_{max}. As such, high flux reactors are favored over the low flux reactors to produce higher activity ^{192}Ir sources and with a shorter turnaround time. If one takes the nominal ϕ_n of 1.0x10^{15} neutrons cm^{-2} s^{-1}, which is available at the High Flux Isotope reactor (HFIR) at the Oak Ridge National Laboratory (ORNL) [17], and the feed material with an initial ^{191}Ir atomic number density of 5.69x10^{22} atoms cm^{-3}, Table 3.1 shows that the MAA cm^{-3} of ^{192}Ir is 1.765x10^{9} MBq and it is achieved with merely 9.5 days in the reactor. Accordingly, the MAAs of ^{192}Ir for the 3mmx2mm disk source used in the MCNP6 calculations can be calculated as $\frac{1.765 \times 10^9}{cm^3}\pi(0.15cm)^2(0.2cm) = 2.495 \times 10^7 MBq \cong 674.3Ci$.

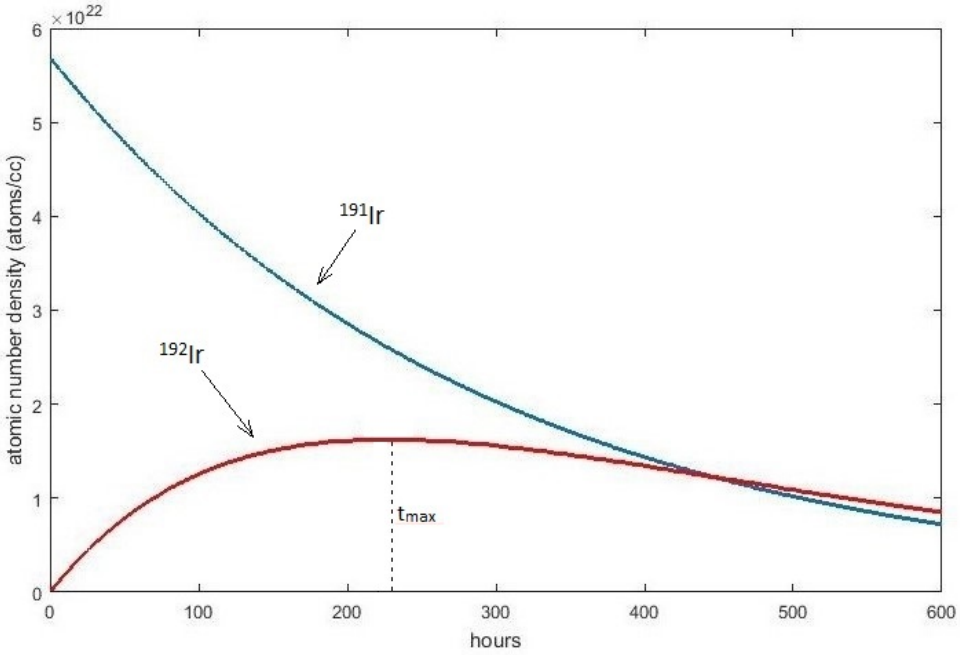

Figure 3.6: Time-dependent growth and depletion of the quantities of ^{191}Ir and ^{192}Ir inside a nuclear reactor based on ϕ_n of 1.0x10^{15} neutrons cm^{-2} sec^{-1}.

Table 3.1: The MAAs cm^{-3} of ^{192}Ir and the corresponding irradiation times for various thermal neutron fluence rates.

ϕ_n (neutrons cm^{-2} s^{-1})	MAA (Mbq cm^{-3})	Irradiation time (days)
1.0x10^{14}	1.310x10^{9}	71.9
2.0x10^{14}	1.524x10^{9}	41.3
4.0x10^{14}	1.669x10^{9}	22.4
6.0x10^{14}	1.721x10^{9}	15.4
8.0x10^{14}	1.754x10^{9}	11.7
1.0x10^{15}	1.765x10^{9}	9.5
2.0x10^{15}	1.809x10^{9}	4.8

3.3.1 Minibeam dose distributions obtained from MCNP6

Ultimately, none of the brass collimators were able to give sufficiently high PVDRs at the surface and a high enough in-beam dose rate at 10 cm depth to deliver 10 Gy to a target at

10 cm depth while delivering less than 4 Gy to the valley region at the surface. Because of this, tungsten was used as the sole collimator material. For tungsten, the ideal thickness was found to be 5.5 cm, as any increase past point reduced the dose rate while only giving a negligible increase in the PVDRs. The following results all use these collimator parameters.

Using the ^{192}Ir activity obtained in the previous section, it is possible to calculate the dose rate and dose distribution in the water phantom. Figure 3.7 shows dose distribution from a single beam. By using superposition, it was possible to use this distribution to construct the expected dose distributions from using different center-to-center distances, an example of which can be seen in Figure 3.8. While this method gives a good visualization of the dose distribution, it can not be used to calculated the PVDR, as the low relative photon fluence in the valley leads to high error ($>$30%) in this region (compared to the $<$2% error in beam). As mentioned in the methods section, this problem was solved by using concentric ring tally volumes. The PVDRs for different center-to-center spacings can be seen in Table 3.2, while Table 3.3 shows the corresponding dose rates.

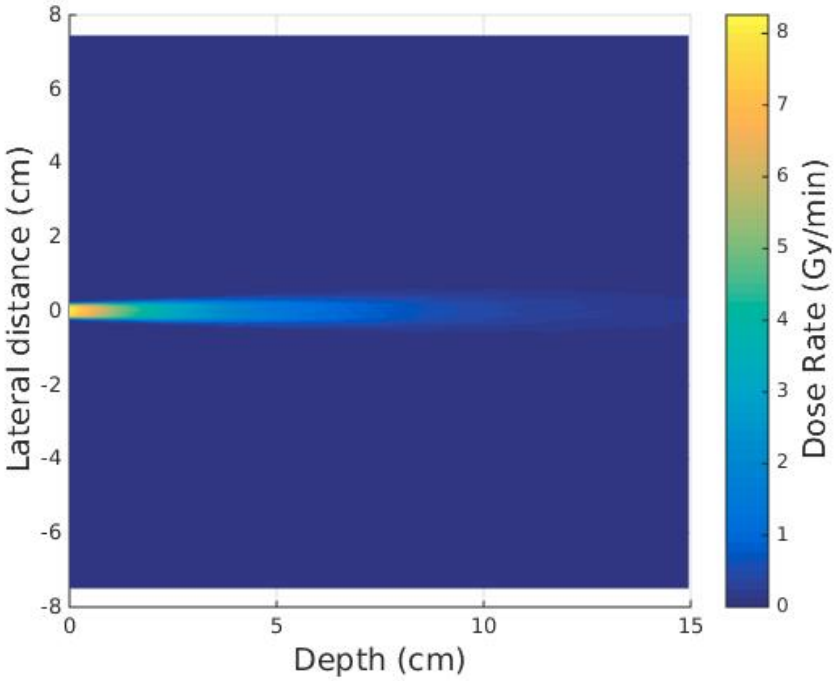

(a)

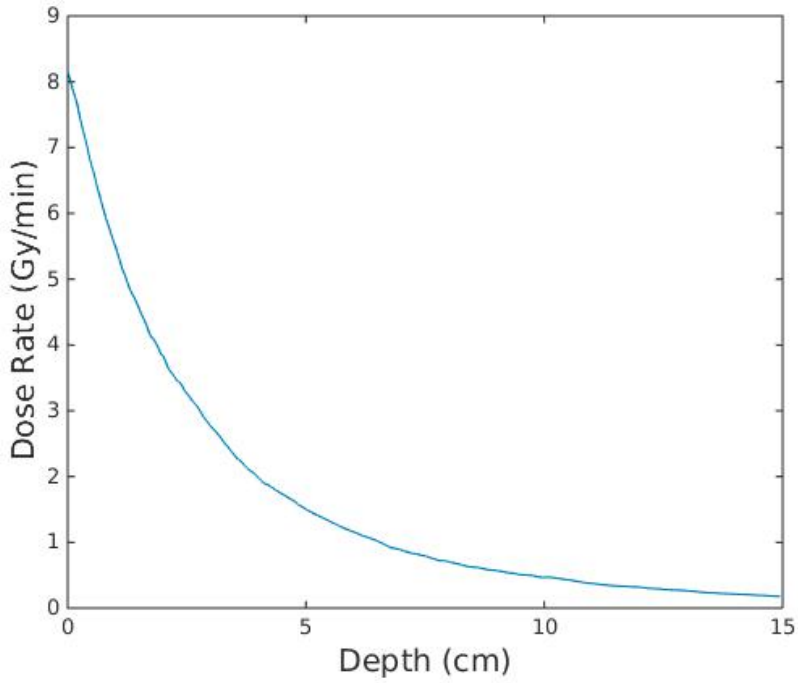

(b)

Figure 3.7: MCNP6 results of the single 3 mm minibeam characteristics for ^{192}Ir: (a) the 2-D in-phantom dose profile, and (b) the in-phantom depth-dose distribution along the beam centerline.

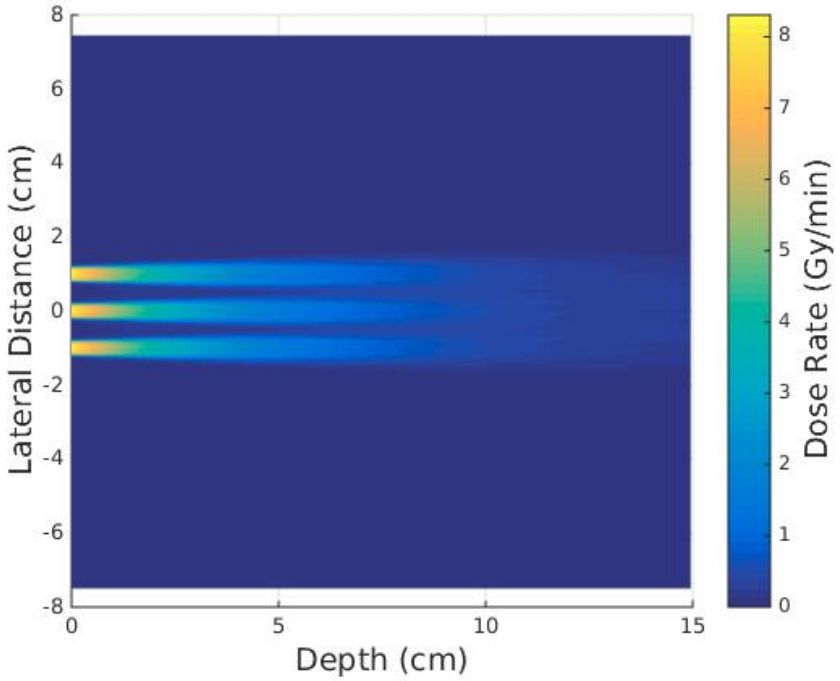

(a)

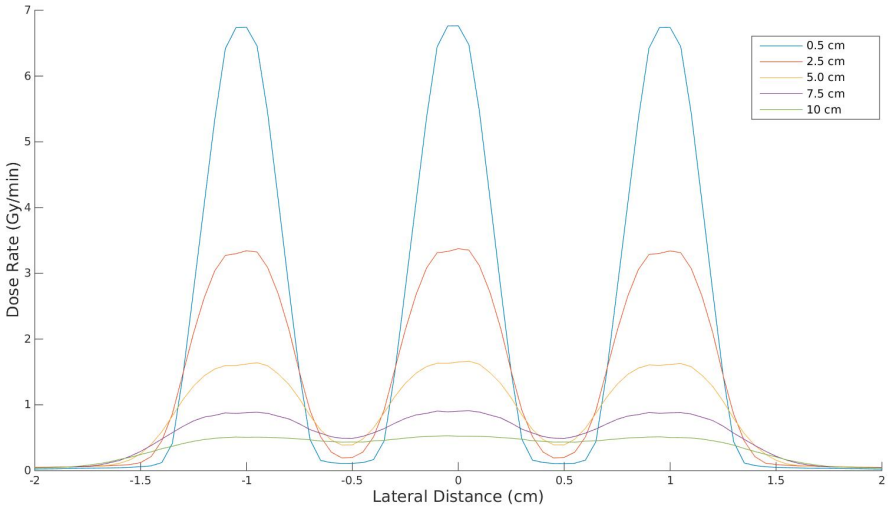

(b)

Figure 3.8: MCNP6 results of the superposition of 7 parallel 3 mm ^{192}Ir minibeams with a c-t-c of 8 mm : (a) the 2-D in-phantom dose profile, and (b) the cross-sectional dose distributions

Table 3.2: The PVDRs at various depths in the water phantom produced by a hexagonal array of parallel 3-mm (in diameter) ^{192}Ir minibeams of various c-t-c distances.

Depth in phantom (cm)	PVDR			
	6 mm c-t-c	8 mm c-t-c	10 mm c-t-c	12 mm c-t-c
0.5	26.2	58.8	90.8	182.4
2.5	2.7	17.5	31.1	56.9
5.0	0.77	2.3	10.4	27.7
7.5	0.67	0.94	2.1	15.0
10.0	0.96	0.75	1.1	7.0

Table 3.3: The dose rates at various depths in the water phantom produced by a hexagonal array of parallel 3-mm (in diameter) ^{192}Ir minibeams of various c-t-c distances.

Depth in phantom (cm)	Dose Rate (Gy/min)			
	6 mm c-t-c	8 mm c-t-c	10 mm c-t-c	12 mm c-t-c
0.5	8.24	8.14	8.11	8.10
2.5	3.88	3.85	3.87	3.78
5.0	1.87	1.82	1.81	1.73
7.5	1.14	0.97	0.94	0.86
10.0	1.01	0.57	0.52	0.46

Compared to the electron GRID investigated earlier, the ^{192}Ir minibeams offer a marked increased in PVDR, though a similarly sharp drop of the dose rate with depth. The reason for this drop off is different however; for the electrons, it is caused primarily by lateral scattering by the electrons out of the main beam-line while for the ^{192}Ir beams it is caused primarily by the $1/r^2$ effect. With the collimator placed 0.2 cm from the surface and a collimator thickness of 5.5 cm, the ratio of the dose rate at a depth of 0.5 cm to that at 10 cm depth is $\frac{1/(5.7cm+0.5cm)^2}{1/(5.7cm+10cm)^2} \approx 6.41$, while the ratio for an accelerator based system with a source to surface distance (SSD) of 100 cm (such as megavoltage or electron GRID RT)

is $\frac{1/(100cm+0.5cm)^2}{1/(100cm+10cm)^2} \approx 1.21$. While this does not account for the full drop-off (using a mean gamma energy of 371.5 keV, the dose rate ratio from attenuation is $\frac{e^{-0.11cm^{-1}\times 0.5cm}}{e^{-0.11cm^{-1}\times 10cm}} \approx 2.83$), it is a major contributing factor. Increasing the distance between the collimator and the phantom surface would decrease the dose fall off in the phantom, but at the cost of decreasing the already low absolute dose rate and increasing the spot size at the surface.

On the topic of spot size, it can be seen from Figure 3.7 that even though the collimator hole size is 3 mm, the beam FWHM at the surface is about 5 mm, which was identified as the largest hole diameter thought to still give a significant radiobiological advantage. Because of this, these results were re-run using a 2 mm source and hole size to decrease the spot size at the surface.

3.3.1 Reduced source size, Ir-192

The main result of this reduction in size was a decrease in the total activity of each ^{192}Ir source. From the reduction in source volume, the source activity changed from 674.3 Ci to 299.7 Ci. Additionally, the range of c-t-c spacings investigated was changed from 6, 8, 10, 12 mm to 4, 6, 8, 10 mm to account for the smaller hole size. Other than these changes, the simulations and analysis were conducted identically to those run previously.

Figure 3.9 shows the single beam 2D dose distribution and PDD for this new geometry, a parallel to Figure 3.7. As one would expect from the over 50% reduction in source activity, the dose rate drops by a similar amount, going from about 8 Gy min^{-1} to 3.5 Gy min^{-1} at the surface. However, the spot size at the surface does drop below the 5 mm diameter limit.

Figure 3.10 shows the results corresponding to Figure 3.8, though using a reduced center-to-center spacing of 8 mm instead of 10 mm. As with the single beam results, the main difference is the reduction in the dose rate seen throughout the distribution. Table 3.4 shows the PVDRs for various depths using different center-to-center spacings, while Table 3.5 shows the corresponding dose rates.

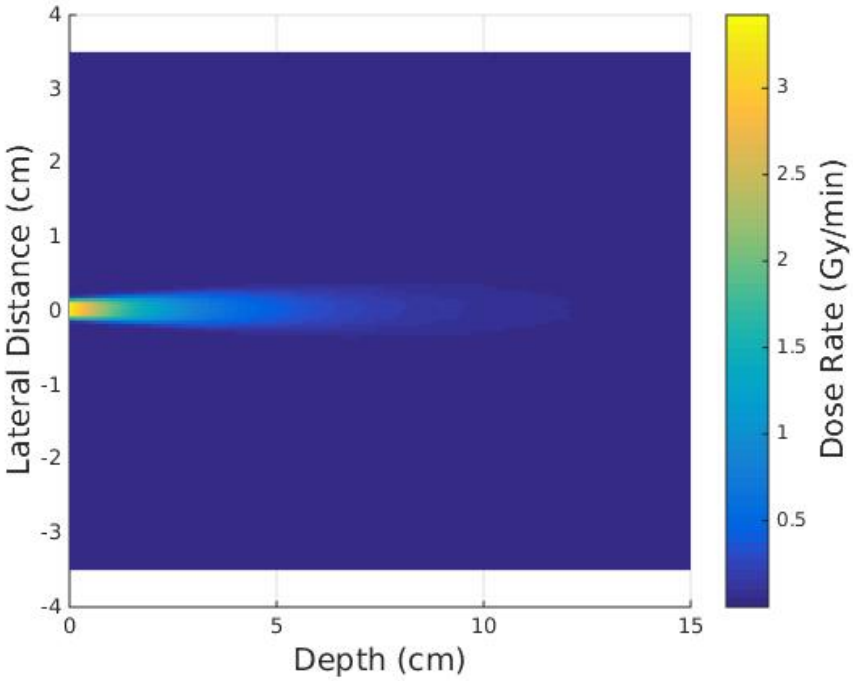

(a)

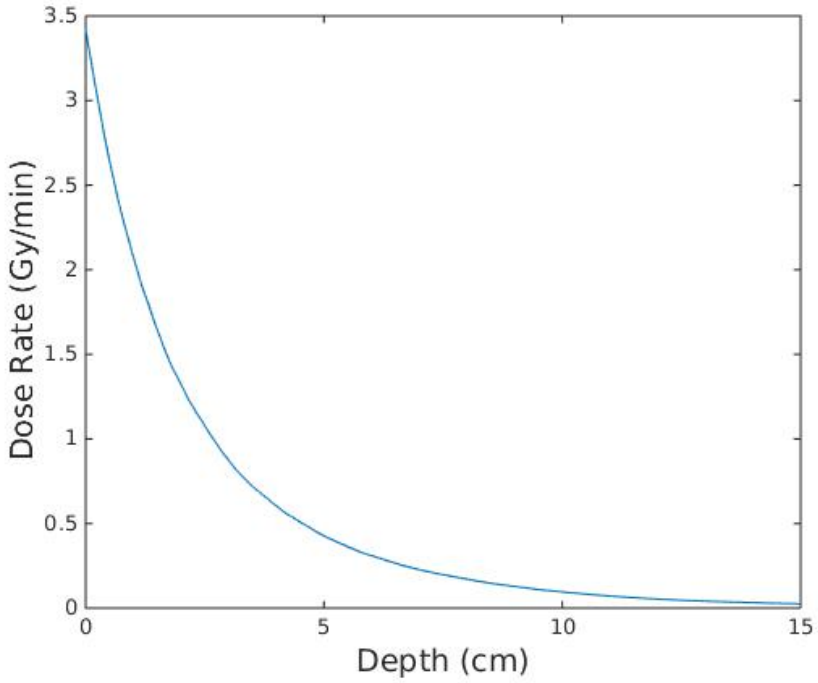

(b)

Figure 3.9: MCNP6 results of the single 2 mm minibeam characteristics for ^{192}Ir: (a) the 2-D in-phantom dose profile, and (b) the in-phantom depth-dose distribution along the beam centerline.

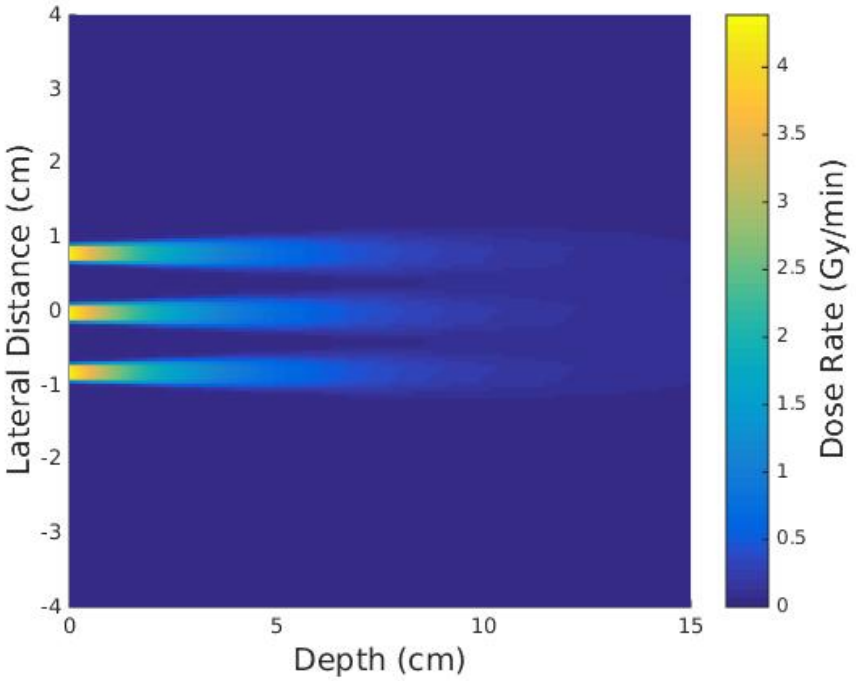

(a)

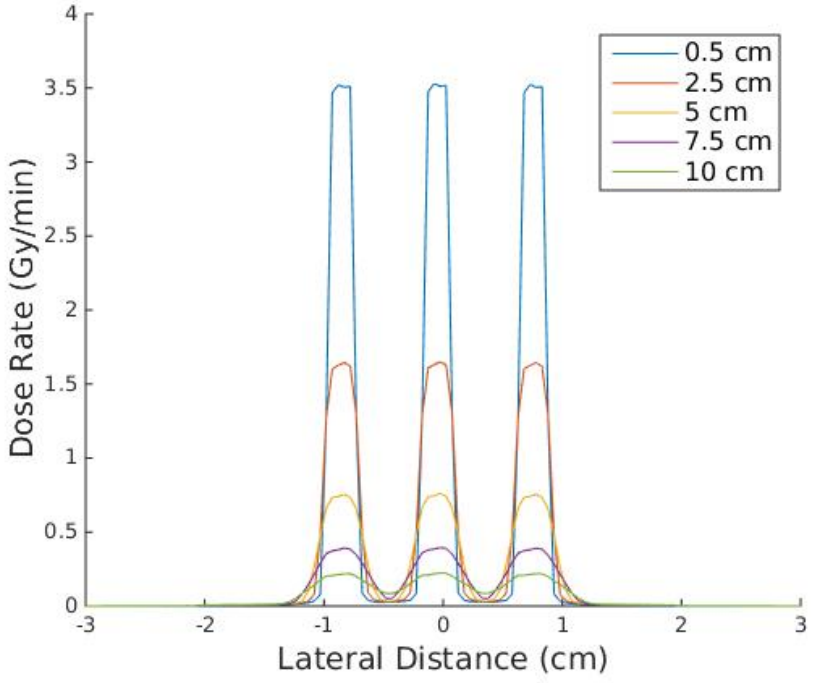

(b)

Figure 3.10: MCNP6 results of the superposition of 7 parallel 2 mm ^{192}Ir minibeams with a c-t-c of 8 mm : (a) the 2-D in-phantom dose profile, and (b) the cross-sectional dose distributions

Table 3.4: The PVDRs at various depths in the water phantom produced by a hexagonal array of parallel 2-mm (in diameter) ^{192}Ir minibeams of various c-t-c distances.

Depth in phantom (cm)	PVDR			
	4 mm c-t-c	6 mm c-t-c	8 mm c-t-c	10 mm c-t-c
0.5	26.4	87.24	154.0	210.5
2.5	2.37	29.8	59.5	87.2
5.0	0.78	4.82	24.4	41.4
7.5	0.67	1.30	6.94	21.2
10.0	0.95	0.83	1.90	7.96

Table 3.5: The dose rates at various depths in the water phantom produced by a hexagonal array of parallel 2-mm (in diameter) ^{192}Ir minibeams of various c-t-c distances.

Depth in phantom (cm)	Dose Rate (Gy/min)			
	4 mm c-t-c	6 mm c-t-c	8 mm c-t-c	10 mm c-t-c
0.5	3.62	3.60	3.59	3.61
2.5	1.69	1.67	1.68	1.70
5.0	0.81	0.78	0.77	0.77
7.5	0.49	0.40	0.40	0.39
10.0	0.43	0.23	0.22	0.22

3.3.2 Co-60 minibeams

3.3.2 Maximum achievable activity

Similarly to the iridium calculations, the maximum achievable activities were calculated for a variety of neutron fluxes. Table 3.6 shows these MMAs.

Table 3.6: The MAAs cm^{-3} of ^{60}Co and the corresponding irradiation times for various thermal neutron fluence rates.

ϕ_n (neutrons cm^{-2} s^{-1})	MAA (Mbq cm^{-3})	Irradiation time (days)
1.0x10^{14}	1.281x10^{8}	2876
5.0x10^{14}	2.322x10^{9}	1108
1.0x10^{15}	2.650x10^{8}	674

Because of the the long half-life of ^{60}Co, reaching the maximum achievable activity takes considerably longer than for ^{192}Ir, taking at a minimum of 674 days, or almost two years, compared to the maximum of 71.9 days for iridium. This makes it impractical to aim for this maximum level of activity. Instead, it is better to chose some reasonable amount of time, such as 60 days, that provides an acceptable level of activation. Using this irradiation time of 60 days and a ϕ_n of 5.0x10^{14} n cm^{-2} s^{-1} gives a nominal MMA of 1.466x10^{8} Mbq cm^{-3}. Using this and a source size of 3mmx15mm, the activity can be calculated as $\frac{1.466 \times 10^8}{cm^3}\pi(0.15cm)^2(1.5cm) = 1.554^7 MBq \cong 420Ci.$

3.3.2 Dose distribution

As with the ^{192}Ir, none of the brass collimators were able to give sufficiently high PVDRs at the surface and a high enough in-beam dose rate at 10 cm depth to deliver 10 Gy to a target at 10 cm depth while delivering less than 4 Gy to the valley region at the surface. Tungsten was used as the collimator material though ideal thickness increased to 8 cm.

Again, the MMA can be used to calculate the dose rate and distribution of the ^{60}Co minibeams. Figure 3.11 shows the dose distribution and the PDD curve for a single cobalt beam. While the dose rate fall off is still significant, it is not as severe as in the ^{192}Ir case, likely due to reduce attenuation of the beam because of the higher mean photon energy. This increased penetrative ability does come with a downside, namely increased leakage through the collimator leading to a lower PVDR at the surface than the ^{192}Ir case.

These PVDRs can be seen in Table 3.7, as well as in Figure 3.12, which shows the dose distribution resulting from the superposition of seven beams. While not nearly as high as for the iridium beams, the PVDRs are still comparable or greater than those in MV treatments.

The PVDRs, shown in Table 3.7, are a fair bit lower than those for the comparable ^{192}Ir case, while the dose rates, shown in Table 3.8, are similar, abet with slightly lower dose rates at the surface and slightly high dose rates at deeper depths.

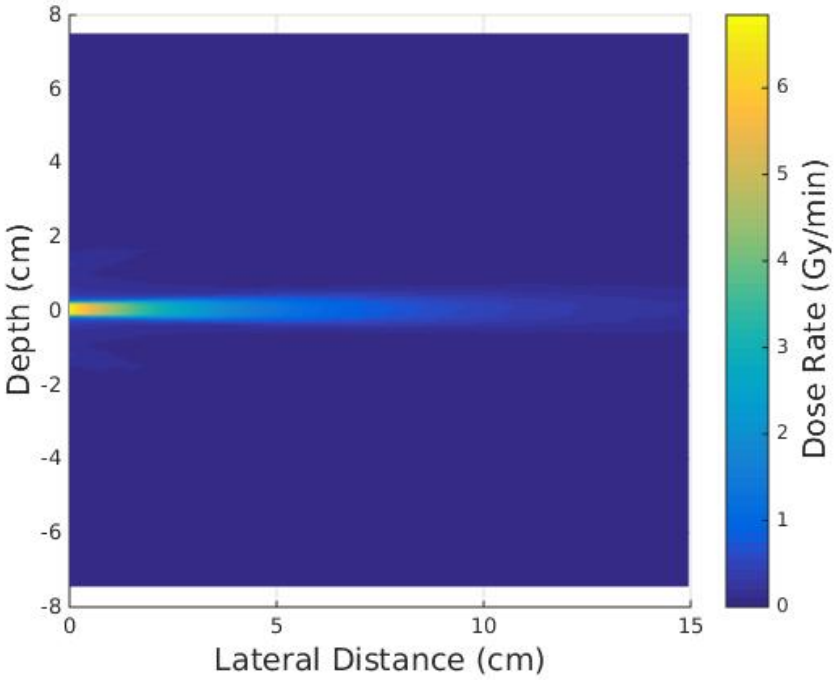

(a)

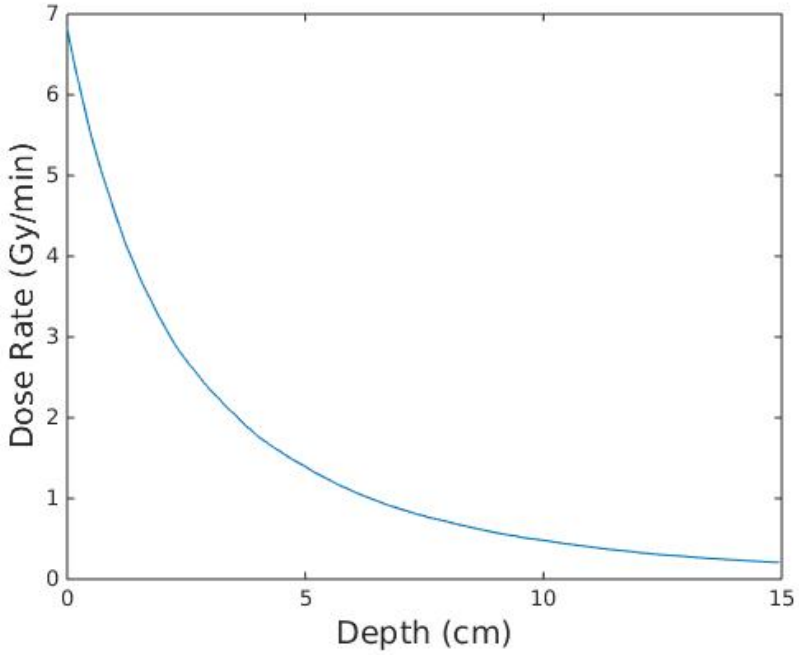

(b)

Figure 3.11: MCNP6 results of the single 3 mm minibeam characteristics for ^{60}Co: (a) the 2-D in-phantom dose profile, and (b) the in-phantom depth-dose distribution along the beam centerline.

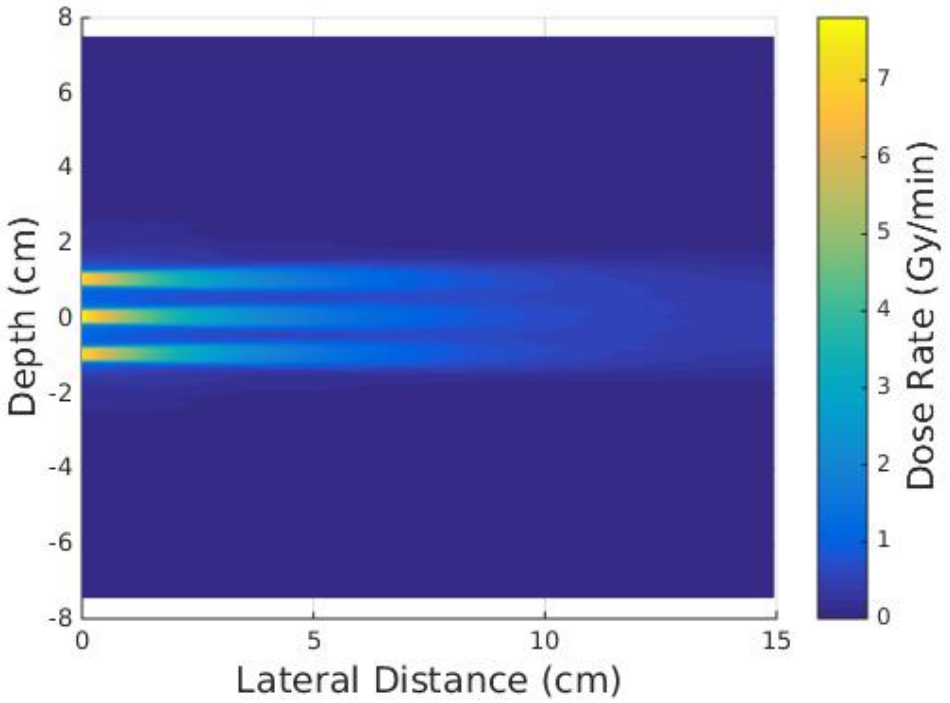

Figure 3.12: MCNP6 results of the superposition of 7 parallel 3 mm ^{60}Co minibeams with a c-t-c of 10 mm : (a) the 2-D in-phantom dose profile, and (b) the cross-sectional dose distributions

Table 3.7: The PVDRs at various depths in the water phantom produced by a hexagonal array of parallel 3-mm (in diameter) ^{60}Co minibeams of various c-t-c distances.

Depth in phantom (cm)	PVDR			
	6 mm c-t-c	8 mm c-t-c	10 mm c-t-c	12 mm c-t-c
0.5	9.98	22.02	33.82	44.30
2.5	3.77	12.73	24.00	36.55
5.0	1.22	5.09	12.81	20.87
7.5	0.79	1.90	6.01	12.07
10.0	0.73	1.10	2.55	6.18

Table 3.8: The dose rates at various depths in the water phantom produced by a hexagonal array of parallel 3-mm (in diameter) ^{60}Co minibeams of various c-t-c distances.

Depth in phantom (cm)	Dose Rate (Gy/min)			
	6 mm c-t-c	8 mm c-t-c	10 mm c-t-c	12 mm c-t-c
0.5	7.93	7.68	7.65	7.63
2.5	4.68	4.62	4.61	4.62
5.0	2.78	2.71	2.69	2.69
7.5	1.84	1.70	1.68	1.09
10.0	1.37	1.15	1.09	1.06

3.3.2 Reduced source size, Co-60

As with the ^{192}Ir results above, using 3 mm diameter sources and collimator holes led to a surface spot size above 5 mm in diameter. Again, the simulations were re-run using 2 mm diameter sources to reduce the spot size below this threshold. In the case of the ^{60}Co, the activity per source was subsequently reduced from 420 Ci to 186.7 Ci. And, as with the ^{192}Ir case, the c-t-c spacings investigated were changed from 6, 8, 10, and 12 mm to 4, 6, 8, and 10 mm. Figure 3.13 shows the new single beam distribution while Figure 3.14 shows the distribution from the full array of seven beams. The new PVDR and dose rate results can be seen in Tables 3.9 and 3.10, respectively.

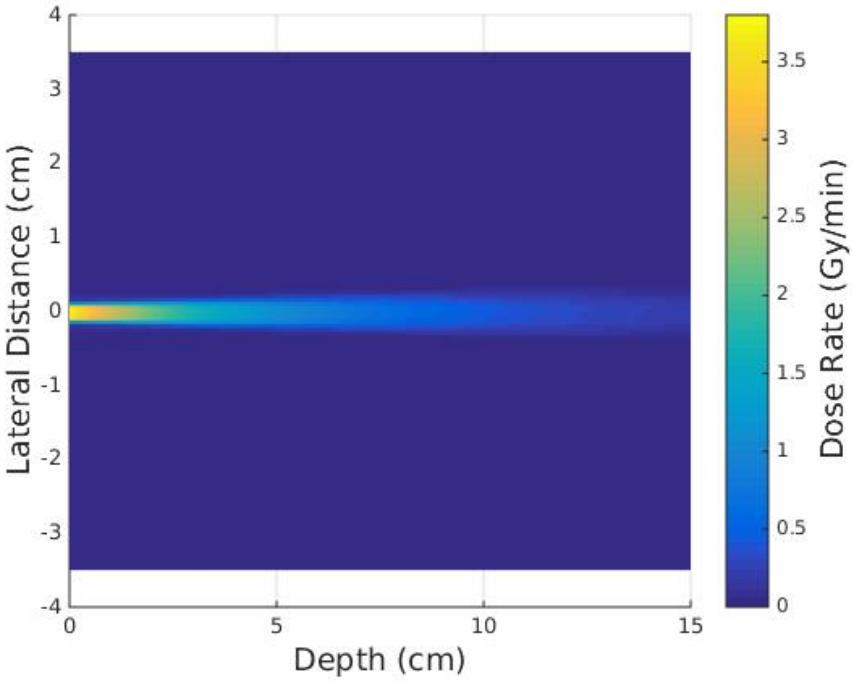

(a)

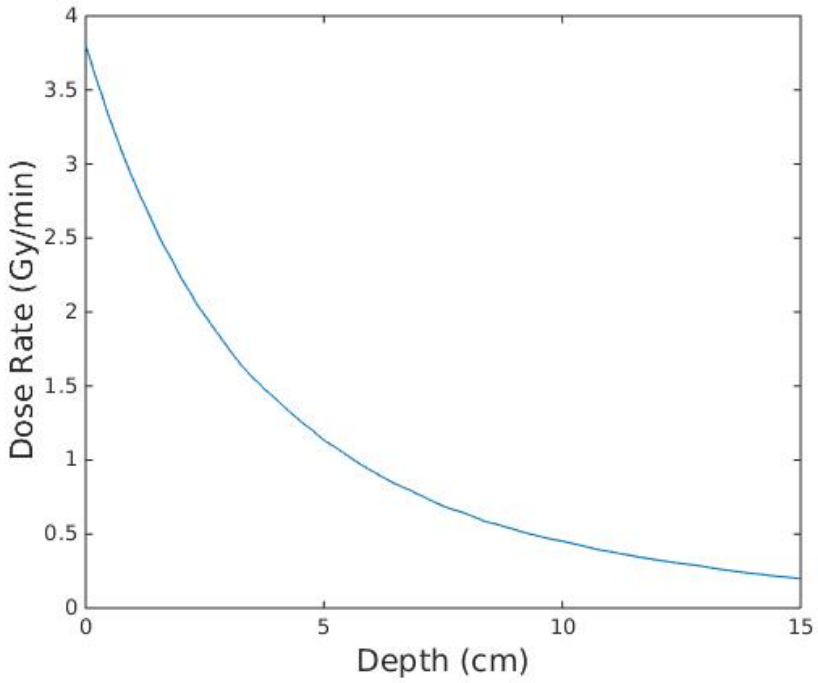

(b)

Figure 3.13: MCNP6 results of the single 2 mm minibeam characteristics for ^{60}Co: (a) the 2-D in-phantom dose profile, and (b) the in-phantom depth-dose distribution along the beam centerline.

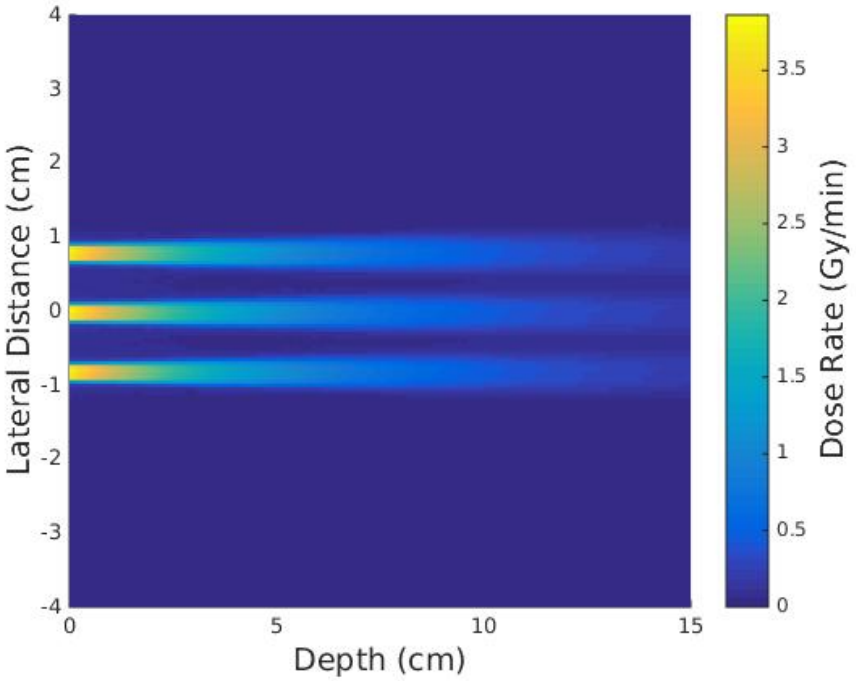

(a)

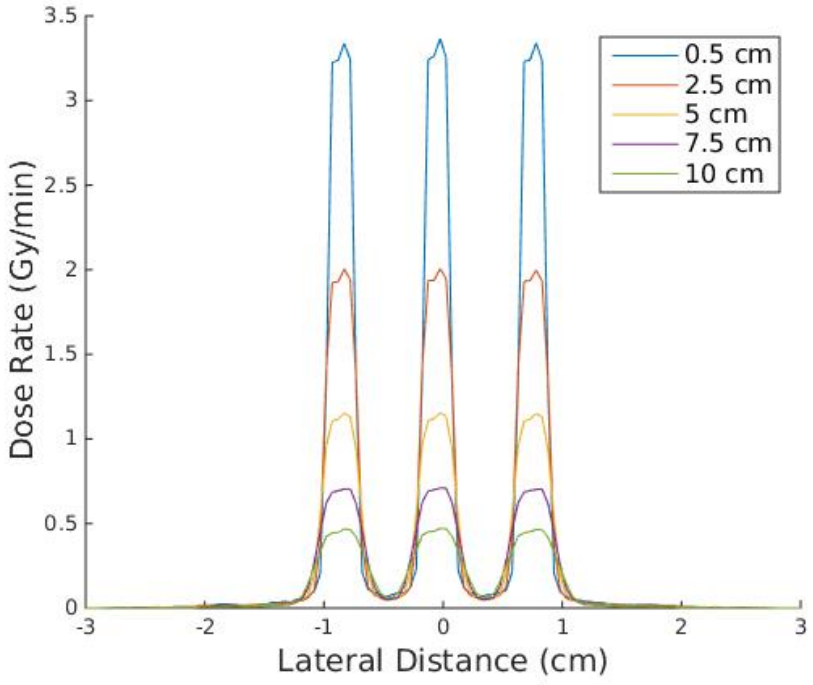

(b)

Figure 3.14: MCNP6 results of the superposition of 7 parallel 2 mm ^{60}Co minibeams with a c-t-c of 8 mm : (a) the 2-D in-phantom dose profile, and (b) the cross-sectional dose distributions

Table 3.9: The PVDRs at various depths in the water phantom produced by a hexagonal array of parallel 2-mm (in diameter) ^{60}Co minibeams of various c-t-c distances.

Depth in phantom (cm)	PVDR			
	4 mm c-t-c	6 mm c-t-c	8 mm c-t-c	10 mm c-t-c
0.5	10.17	34.8	56.1	75.3
2.5	3.37	21.4	44.4	64.4
5.0	1.21	8.96	25.8	42.5
7.5	0.79	3.32	13.4	27.4
10.0	0.72	1.58	6.50	16.4

Table 3.10: The dose rates at various depths in the water phantom produced by a hexagonal array of parallel 2-mm (in diameter) ^{60}Co minibeams of various c-t-c distances.

Depth in phantom (cm)	Dose Rate (Gy/min)			
	4 mm c-t-c	6 mm c-t-c	8 mm c-t-c	10 mm c-t-c
0.5	3.41	3.32	3.31	3.31
2.5	2.02	1.98	1.97	1.97
5.0	1.20	1.15	1.14	1.14
7.5	0.79	0.72	0.70	0.70
10.0	0.58	0.47	0.46	0.45

3.3.3 Shielding requirements

The MCNP6 results indicated that, for the maximum activity of 2,100 Ci (i.e. 300 $\times$ 7) of ^{192}Ir, 9.6 cm of lead would reduce the dose rate to 4.55 ($\pm$ 0.21) mrem hr^{-1} at 30.5 cm (or 1 ft) from the surface of the container. This would make the lead container 31.5 kg, which should be a manageable weight at a clinical setting.

Comparatively, for the maximum activity of 1306.9 Ci of ^{60}Co, it would take 24 cm of lead to reduce the dose rate to the same amount. Such a container would have a mass of

984 kg.

As shielding requirements for the treatment device will likely be similar (to prevent excess dose outside of the target area), a ^{60}Co system may have to be fixed, much like current Gamma Knife (Elekta) machines. However, an ^{192}Ir treatment device would be light enough to mount onto a robotic arm to allow for more flexibility in treatment position, more similar to a Cyber Knife unit (Accuray).

3.3.4 Film measurements

As mentioned above, the film measurements were converted to dose using the commercial software FilmQA Pro, produced by Ashland Inc. During the initial comparison, there was a large discrepancy between the absolute dose measurements from the film and the dose calculated from the simulations. This was traced back to a geometry error in defining the source in the MCNP6 input file; the radii of the source and surrounding wire were not converted from mm to cm. As this geometry was specific to just this test case and not the other isotope based simulations used in this work, this had no impact on the validity of the other simulations. After correcting this issue and re-running the simulation, the discrepancy was greatly reduced, but not entirely eliminated. Several other attempts were made to eliminate this difference, including changing the tally type to +F6 and tracking the secondary electrons (in essence, changing from tallying kerma to energy deposited) and expanding the ^{192}Ir spectrum used to include all lines with yields over 0.1% per decay (from a simplified spectrum only including lines with yields above 1%). However, none of these gave results closer to those obtained from the films. Also, the new simulation revealed that the dose delivered to a depth of 0.5 cm was approximately 48 Gy, well above the film's dose limit, so a comparison could no longer be made between the simulation and the film measurement at this depth.

Even with the remaining discrepancies, the simulated and experimental results align well, particularly in high dose regions. Comparisons between the simulated and experi-

mental results can be seen in Figures 3.15 - 3.22.

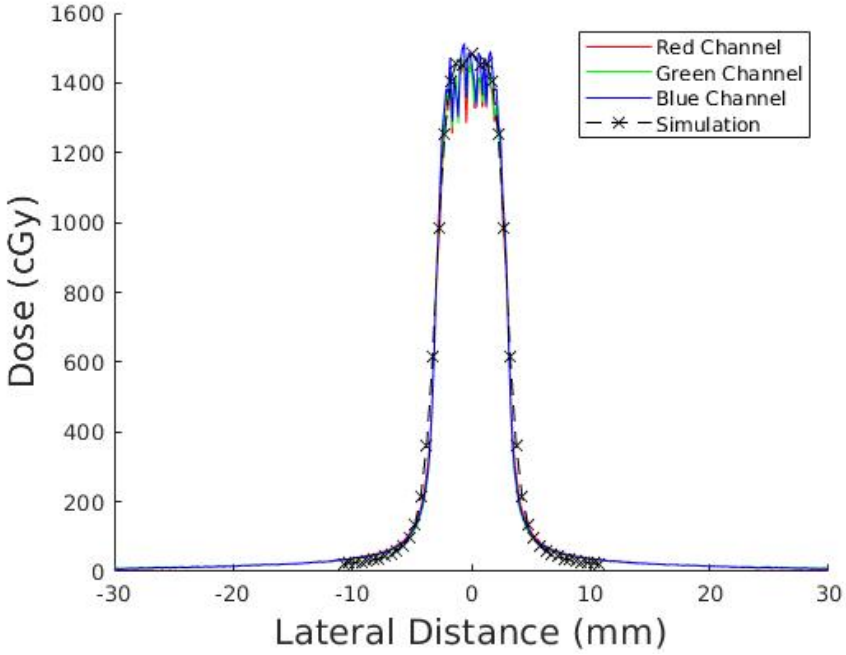

(a)

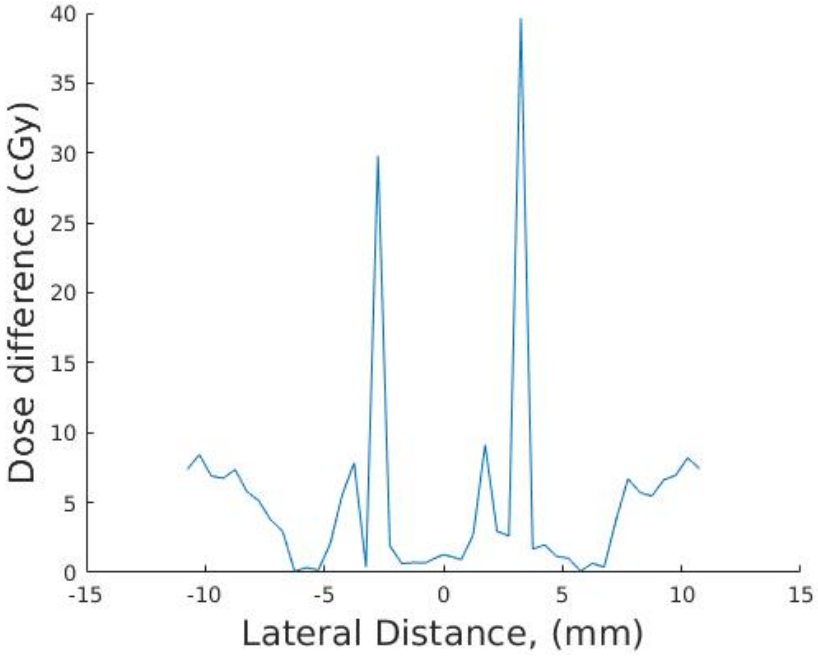

(b)

Figure 3.15: Comparison of simulation and film doses for the ^{192}Ir physical measurements at a depth of 25 mm. (a) shows the absolute doses obtained from both methods while (b) shows the dose difference between the MCNP6 and the film results.

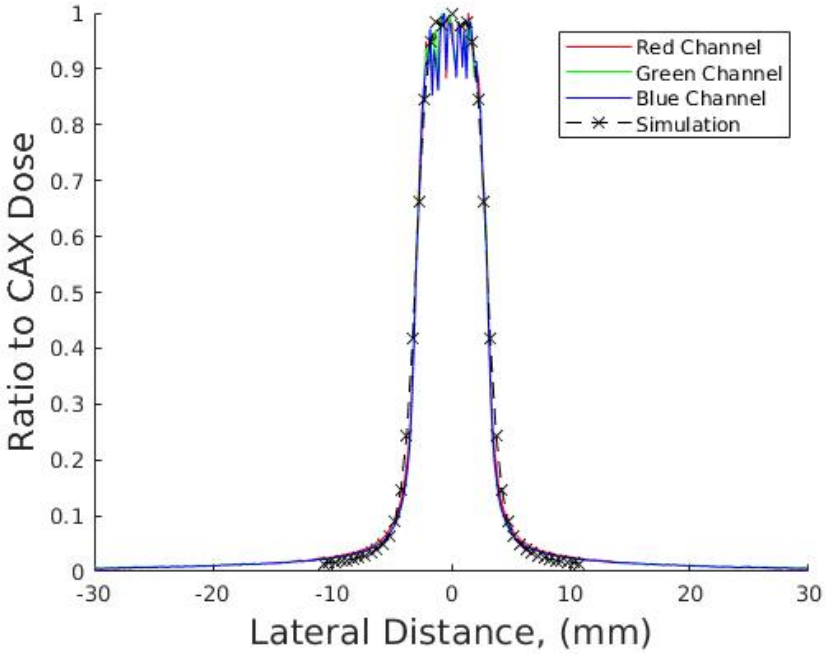

(a)

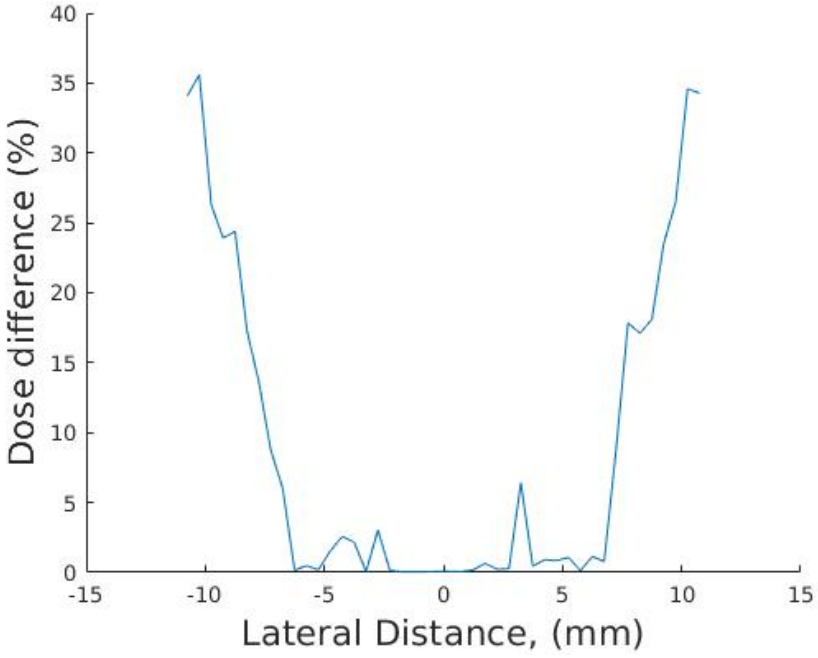

(b)

Figure 3.16: Comparison of simulation and film relative doses for the ^{192}Ir physical measurements at a depth of 25 mm. (a) shows the relative doses (normalized to dose at central axis) obtained from both methods while (b) shows the percent dose difference between the MCNP6 and the film results.

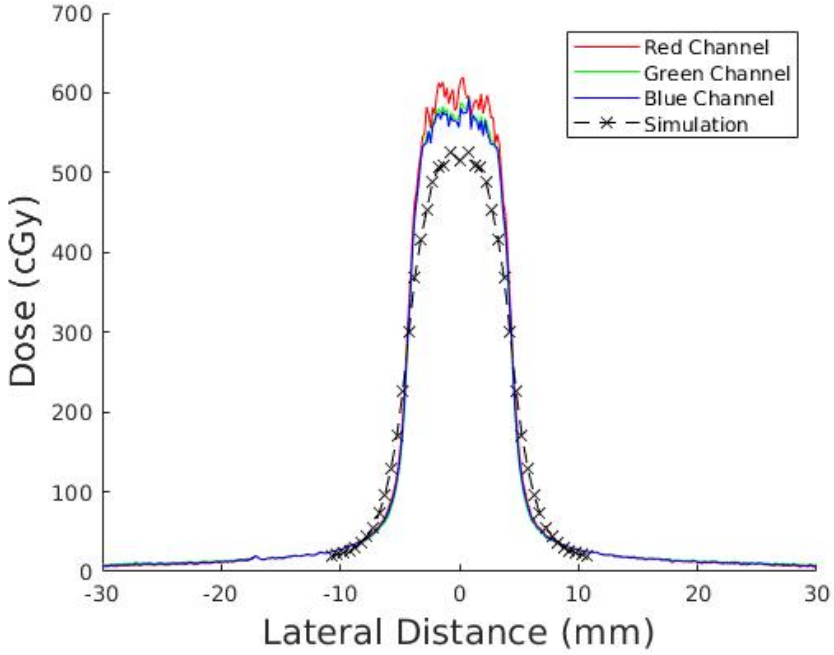

(a)

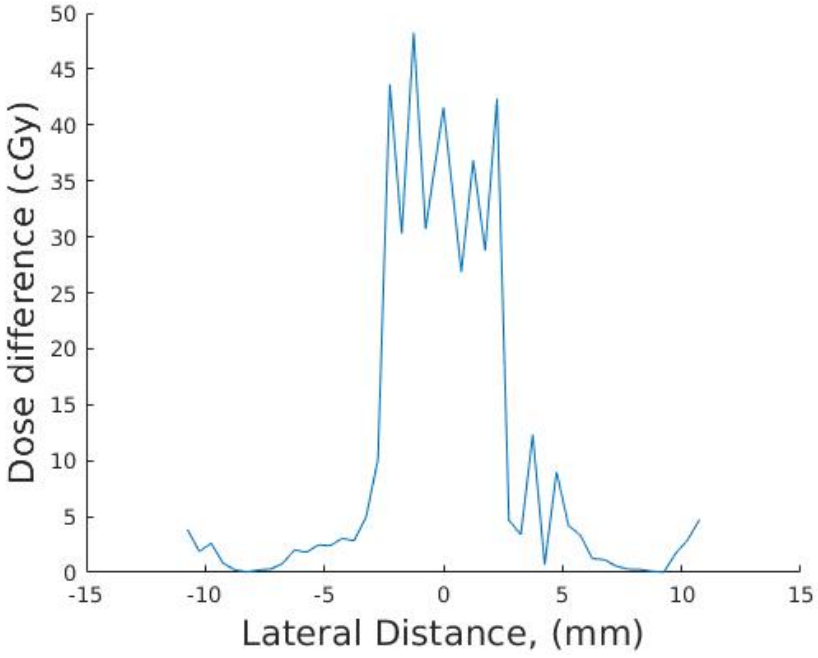

(b)

Figure 3.17: Comparison of simulation and film doses for the ^{192}Ir physical measurements at a depth of 50 mm. (a) shows the absolute doses obtained from both methods while (b) shows the dose difference between the MCNP6 and the film results.

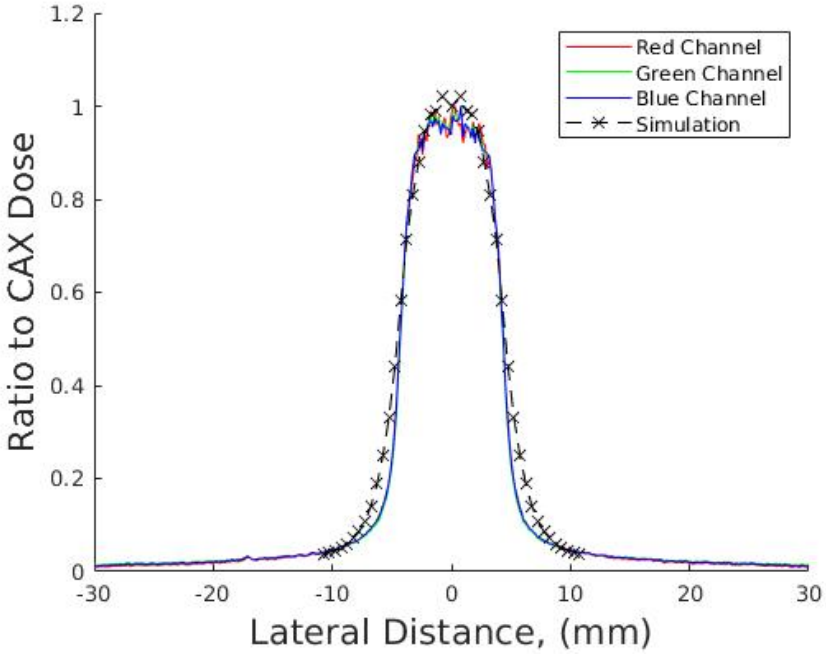

(a)

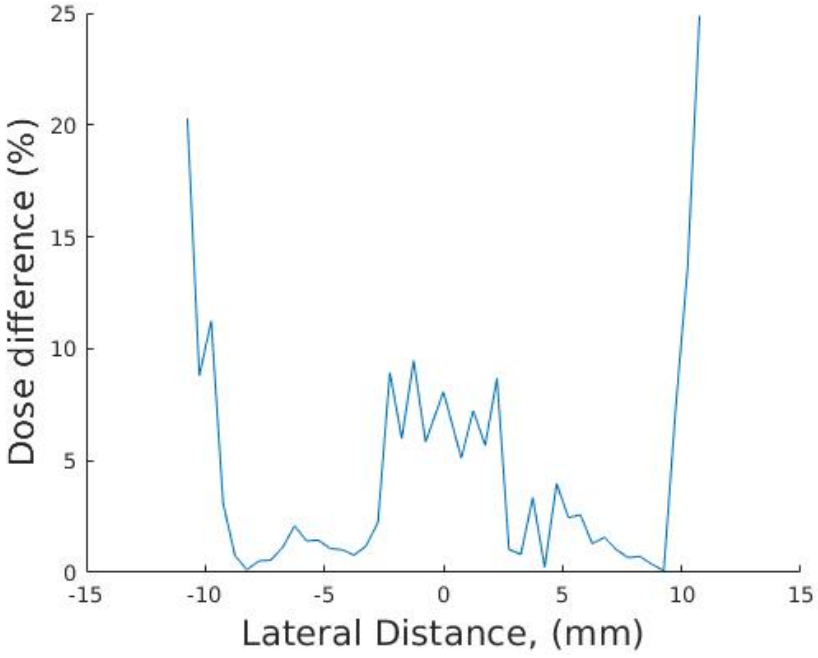

(b)

Figure 3.18: Comparison of simulation and film relative doses for the ^{192}Ir physical measurements at a depth of 50 mm. (a) shows the relative doses (normalized to dose at central axis) obtained from both methods while (b) shows the percent dose difference between the MCNP6 and the film results.

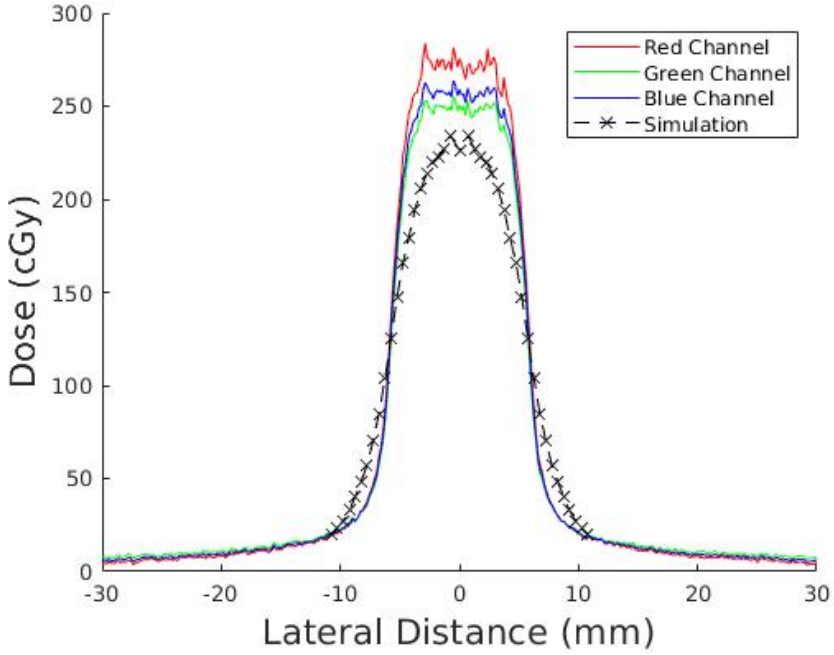

(a)

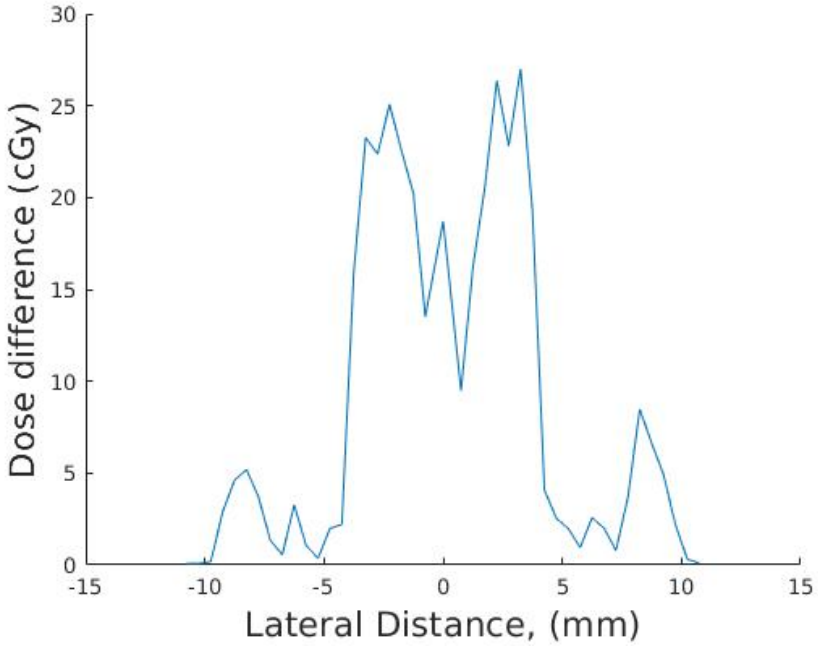

(b)

Figure 3.19: Comparison of simulation and film doses for the ^{192}Ir physical measurements at a depth of 75 mm. (a) shows the absolute doses obtained from both methods while (b) shows the dose difference between the MCNP6 and the film results.

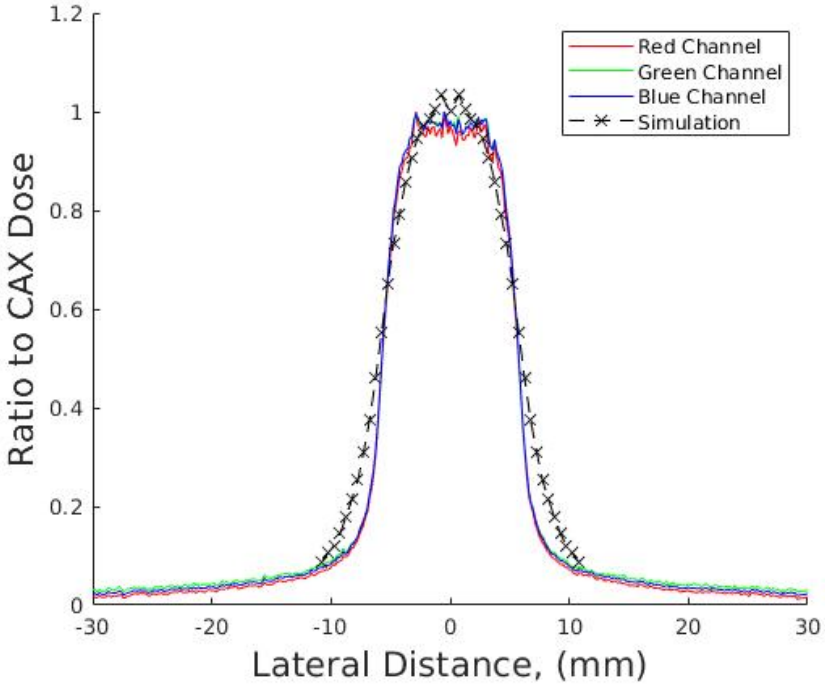

(a)

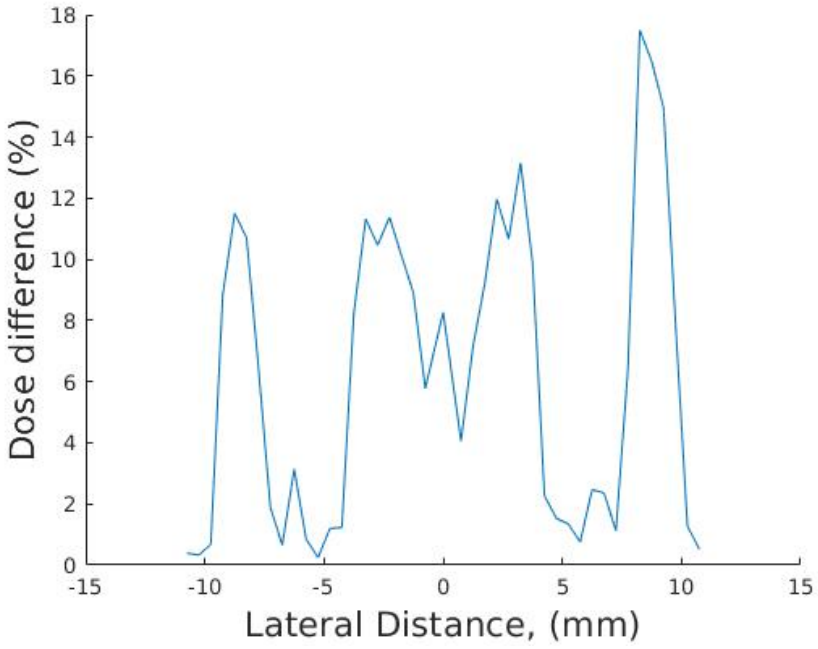

(b)

Figure 3.20: Comparison of simulation and film relative doses for the ^{192}Ir physical measurements at a depth of 75 mm. (a) shows the relative doses (normalized to dose at central axis) obtained from both methods while (b) shows the percent dose difference between the MCNP6 and the film results.

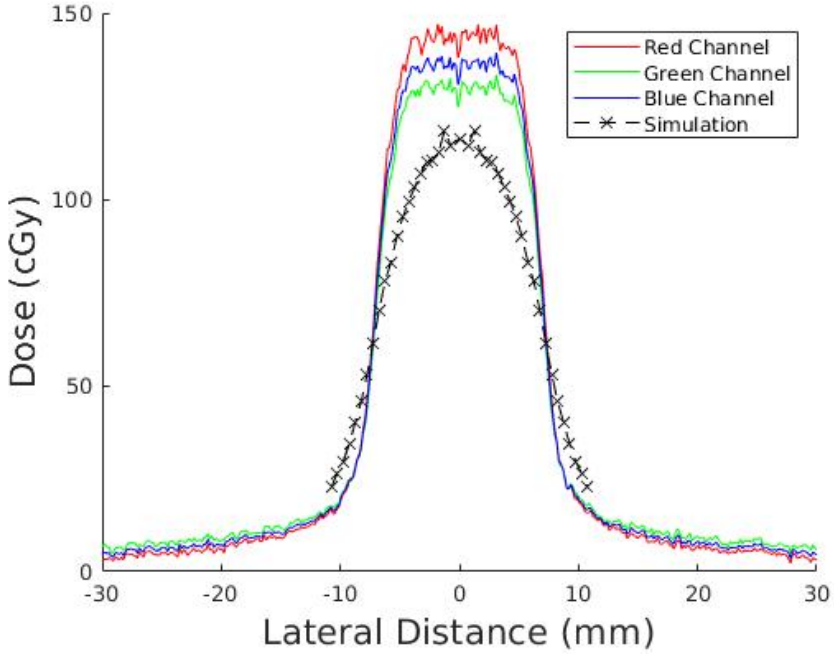

(a)

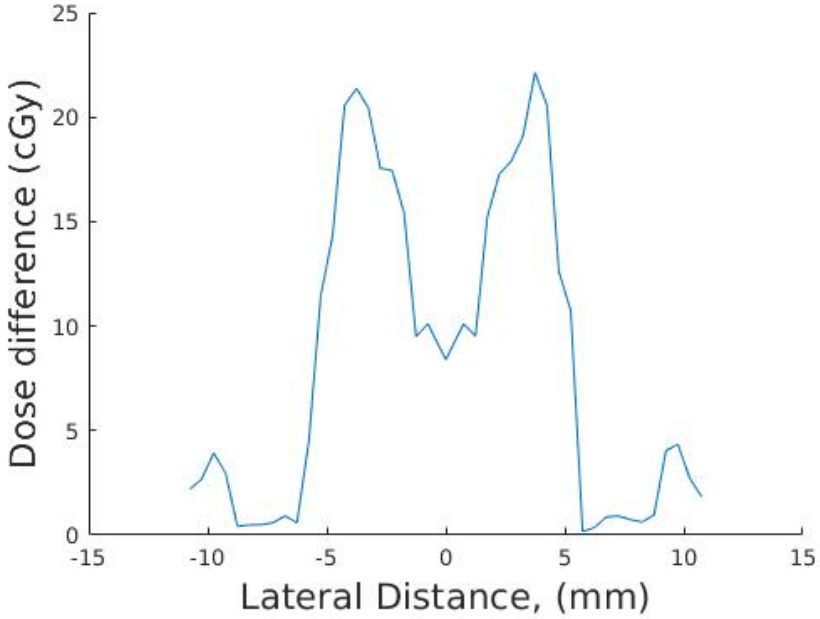

(b)

Figure 3.21: Comparison of simulation and film doses for the ^{192}Ir physical measurements at a depth of 100 mm. (a) shows the absolute doses obtained from both methods while (b) shows the dose difference between the MCNP6 and the film results.

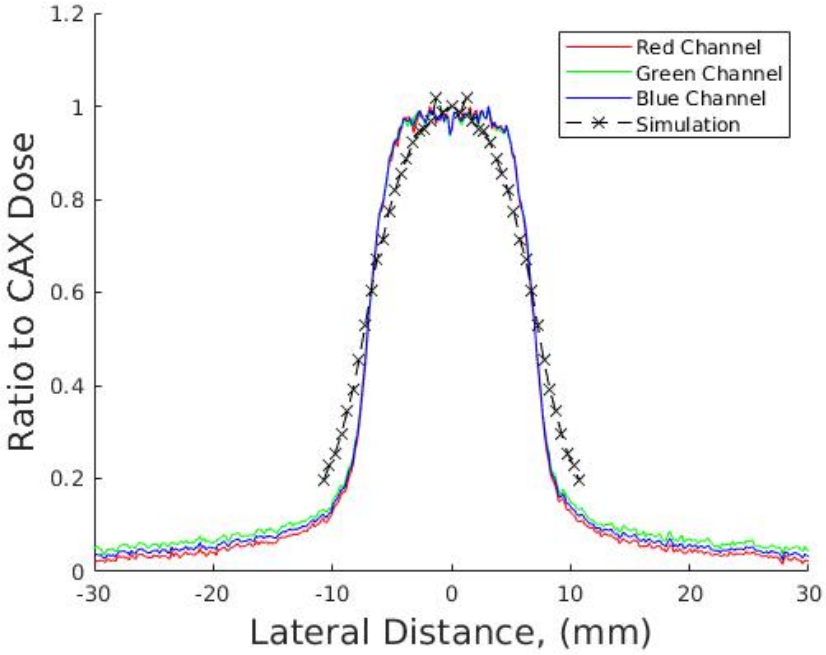

(a)

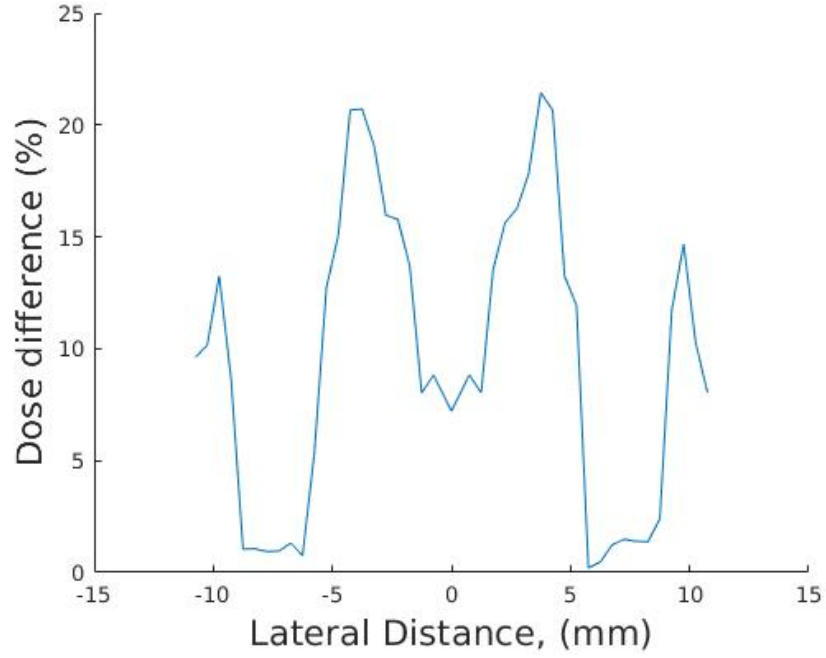

(b)

Figure 3.22: Comparison of simulation and film relative doses for the ^{192}Ir physical measurements at a depth of 100 mm. (a) shows the relative doses (normalized to dose at central axis) obtained from both methods while (b) shows the percent dose difference between the MCNP6 and the film results.

There are several potential causes for these discrepancies. The simplest, and most likely, is some geometric difference between the true experimental setup and the simulation. While as much care was taken to make the set up as exact as possible, based on the small size of the source and beam, even small deviations in the geometry between the measurement and simulation could cause noticeable differences. Another possibility could be an averaging effect caused by the tally volume size in the simulation. While the film has a high spatial resolution, with a pixel size of 0.17 mm, it is difficult to use tally volumes this small in the simulation for two reasons. The first is that the smaller the tally volume, the more difficult it becomes to get good statistics, especially in the valley region where the photon flux is already low. The other is that, as mentioned earlier, to decrease the error and drastically increase the run time the simulation is set up to tally kerma instead of energy deposited directly. While this is a good approximation for larger tally volumes, as the secondary electron range is small relative to the tally volume, once the tally volume dimensions approach the electron range, this approximation breaks down.

Overall, the simulations generally appear to underestimate the central axis dose and overestimate the valley dose. If these same discrepancies hold true for the simulations used elsewhere in this chapter, then this would mean that the calculated dose rate and PVDRs would be underestimated. Since the general motivation was to maximize both of these values, this would imply that the "real" system would outperform the simulations.

3.4 Conclusions

3.4.1 Parallel geometry

While the initial hope was that the maximum achievable activity for each of the sources would deliver a high dose rate, allowing for the use of lower activity sources to be feasible, the simulations ultimately showed this to be false. In fact, it appears that even when using the highest possible source activities, ranging from 200-300 Ci per source, the dose rate is still not high enough for the parallel geometries for this to be used as a feasible treatment

technique. From a practicality standpoint, the seven sources need to treat an area with a diameter of up to 2 cm already would require over a kiloCurie of activity. While less than the activity contained in a single GammaKnife unit, this would still pose an issue due to the high activity per source.

Furthermore, even assuming a source could be procured for each beam line, it would take approximately 25 minutes to deliver 10 Gy to a depth of 10 cm using the ^{60}Co sources and 50 minutes to deliver the same dose with the ^{192}Ir sources. To avoid blurring the beams and degrading the PVDR of the treatment, the patient would have to be prevented from moving even fractions of a millimeter for this duration, a difficult task at best and an impossible one at worst.

However, an accelerator based approach could potentially avoid both of these issues. As the beam could be turned on and off, regulatory restrictions would not be as severe and gating could potentially be used to minimize the effect of motion. The beam current could also be modulated to adjust the dose rate and, at least for megavoltage beams, the bremsstralung production would be forward directed. While more difficult from a technical prospective, these potential advantages prompted investigation into the potential dose distributions from a 2 MV system.

3.4.2 Convergent geometry

While the parallel geometry produced a sub-optimal dose rate, the convergent geometry gave dose rates at the target above 3 Gy/min for the ^{60}Co system (while the ^{192}Ir system gave a respectable dose rate of 1.5 Gy/min, the cobalt system is superior in both the ratio of dose at the surface to at depth and in the isotope half-life). With a dose rate on par with GammaKnife and using a similar total activity of cobalt (abet spread across a smaller number of sources), this system could conceivably be used for SBRT style treatments of small tumors. There is a potential trade-off between the ^{192}Ir-based and ^{60}Co-based minibeams. While the ^{192}Ir system requires less shielding, and therefore would be light enough to be

mounted onto a robotic arm for treatment flexibility (similar to the CyberKnife), the short half-life of ^{192}Ir requires the sources be replaced every few months. The ^{60}Co system, while it requires significantly more shielding and likely has to be fixed (similar to the GammaKnife), the longer half-life only requires the sources be replaced every few years.

CHAPTER 4
MV MINIBEAMS

4.1 Motivation

While the isotope minibeams did offer a good PVDR at the surface, low dose rate for the parallel case and the small treatment volume for both cases severely limits the clinical applications of these designs. Since it would be impossible to remedy these limitations using a radioisotope, the possibility of using a bremsstrahlung source was also investigated. By controlling the beam current, one could adjust the dose rate, and changes in the electron energy could be used to modify the mean energy of the source. As mentioned in the previous chapter, the use of an accelerator also means the beam could be turned on and off quickly, which could allow for the treatment to be gated, that is, only have the treatment beam on when the patient is in a certain position. Doing this could prevent the dose distribution from becoming blurred by something like respiratory motion, which would help preserve the PVDR of the treatment.

While 6 MV was the lowest energy bremsstrahlung spectrum physically available, using MCNP6 it was possible to generate lower energy spectra by simulating a beam of electrons incident on a custom designed target. Conversely, while it would be relatively easy to conduct a physical measurement for a 6 MV beam, creating an accurate beam model (in terms of energy spectrum and divergence) for the Varian linear accelerator would be highly difficult, involving careful tuning of the electron energy and of the exact size and composition of parts in the head of the machine, as Varian does not regularly release this proprietary information. As this type of work has frequently been the primary focus of publications or theses [51, 52, 53, 54] and these simulations would not give much more information compared to the physical measurement, it was deemed beyond the scope of this project.

4.2 Beam parameter selection

While in the isotope cases, only the collimator parameters needed to be set, for bremsstrahlung minibeams, the source parameters, such as the electron energy, target thickness, and filter design also need to be set. While in theory, all of these parameters could be tuned to fully optimize the PVDR and dose rate, simulating the production of bremsstrahlung photons is computationally expensive. With the wide variety of combinations possible, I determined that this optimization was beyond the scope of this work and instead selected values for each of these parameters based on justifications from the literature, discussed in detail below.

4.2.1 Electron beam energy and current

Arguably the most important parameter, the electron energy used to generate the beam defines the energy spectrum of the resulting bremsstrahlung photons as well as the photon yield. As the PVDRs of the isotope treatments were inline with what we hoped, we wanted something with a similar mean energy to minimize the modifications to the collimator. As the mean energy of a bremsstrahlung beam is one-third of the maximum energy [55], I chose a 2 MeV beam, to give a mean photon energy of 667 keV, roughly halfway between the mean energies of ^{192}Ir and ^{60}Co.

Similar to the maximum achievable activity of the isotope sources, it is important to find the maximum feasible current that could be used for this type of accelerator to find the dose rate. As a conservative estimate, the data sheet for the modified Varian Clinac-6 accelerator at the University of Maryland [56]. From the sheet, the 2 MeV beam has a peak current of 440 mA, with a pulse width of 3 μs and a pulse repetition rate of up to 300 pulses per second. This gives an effective steady state current of

$$440\,mA \times 3 \times 10^{-6}\,s \times 300\,\frac{pulses}{second} = 0.396\,mA$$

to be used for the dose rate calculations.

4.2.2 Target and filter thickness

The target material was chosen to be tungsten for the same reasons most bremsstrahlung targets are made of tungsten; its high Z increases the photon yield for a given photon energy, and its high melting point means it can absorb the large amount of energy from the electrons that is not converted to photons. The target thickness was chosen to be 1.1 times the CSDA range of the electrons. This was chosen to make sure the electrons would be fully stopped in the target and to give a small degree of filtration. For 2 MeV electrons, the CSDA range as given by NIST [57] is $1.613\,g/cm^2$ which, using a density of tungsten of $18.7\,g/cm^3$, gives a range of $0.086\,cm$ and a target thickness of $0.095\,cm$. For the filter, little was known about what thickness would be "optimal" for this type of setup. As the main concern was reducing superfluous surface dose from low energy x-rays, I determined that any filter that would cut out these photons would be acceptable. The filter was set to be 2 mm of aluminum, which did a good job of filtering out x-rays below 50 keV, as evaluated using the spectrum measured using a energy binned F4 tally.

4.3 Geometry

4.3.1 2 MV beams

With the beam parameters set, the next step was to set the geometry for the collimator used to shape the beams. This collimator design was chosen to be the same as the ^{60}Co, tungsten of a thickness of 8 cm, to simplify the comparison between the different modalities. As the 2 MV beam would have a lower mean energy but a higher max energy than the ^{60}Co source, I determined that this thickness should give comparable levels of shielding. As with the second stage of the isotope simulations, the beam diameter was set to be 2 mm. The center-to-center distances evaluated were also the same, 4, 6, 8, and 10 mm, with a 12 mm case added as well. The geometry, as loaded into MCNP can be seen in Figure 4.1.

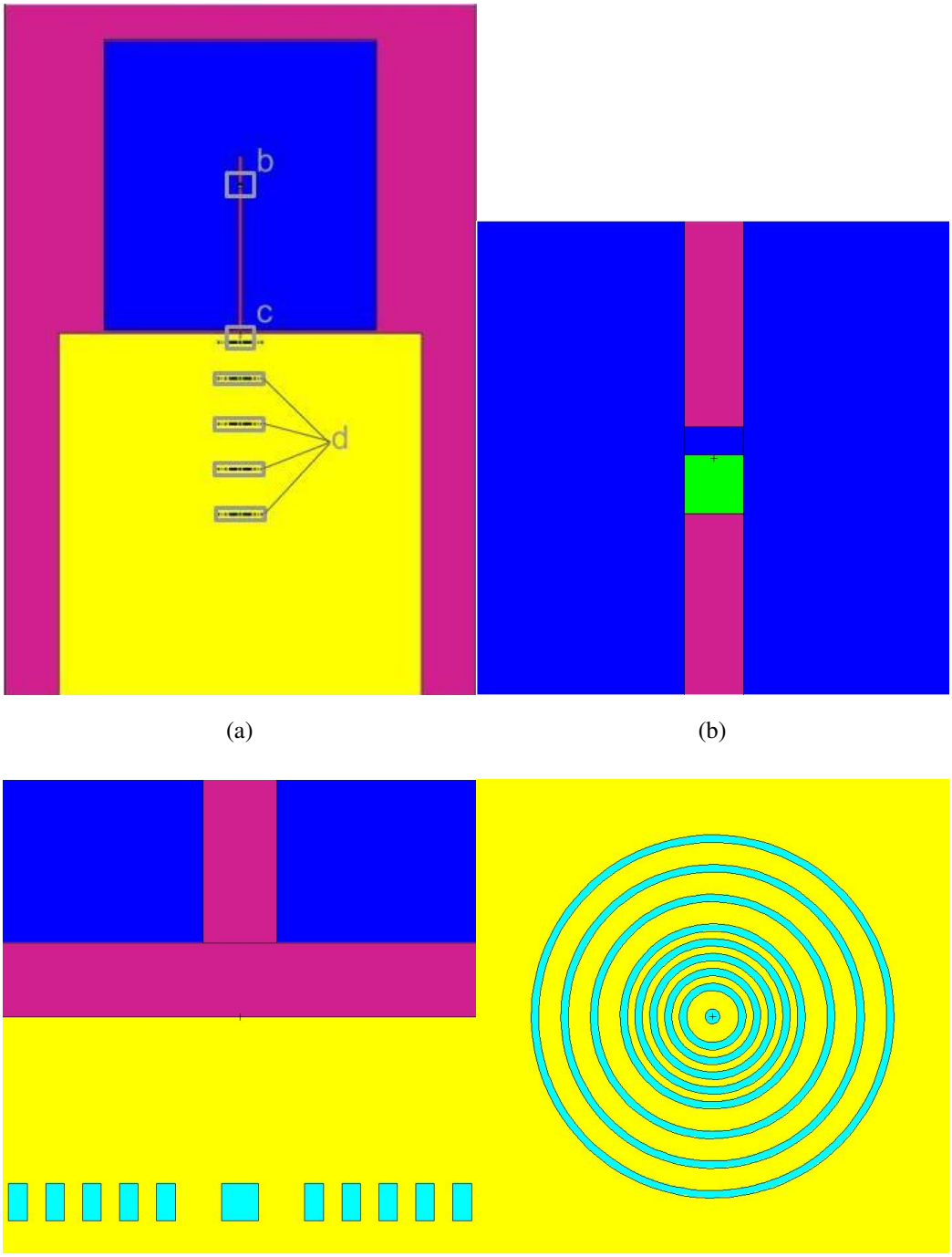

(a) (b)

(c) (d)

Figure 4.1: MCNP geometry for the 2 MV simulations: (a) the main geometry, (b) detail of the target, (c) detail of the beam exit and (d) detail of the tally volumes. For all images, blue represents tungsten (target and collimator), yellow represents water, cyan represents the tally volumes (also water), purple represents air, and green represents aluminum.

The tallies used for the MV case are the same as those used in the isotope case, which

is to say F6 kerma tallies.

4.3.2 6 MV beam

As the 6 MV portion was a physical measurement instead of a simulation, the geometry details were more restrained. For the irradiation, both of tungsten collimators that were initially fabricated for the ^{192}Ir measurements were used. Each collimator is 3 cm thick with a 3 mm diameter hole. The film setup was almost identical to the electron measurement, with a piece of radiochromic film sandwiched in the center of 4 30x30x5 cm slabs of solid water. The setup can be seen in Figure 4.2. The MV imager was used to verify the hole alignment with the centerline of the solid water prior to the film being placed. The film was then irradiated using 2000 MU and a 4x4 cm field. The field size was chosen to not extend beyond the edges of the collimator and is the smallest field size for which there is a MU to dose conversion factor given in the calculation book created when the linear accelerator was commissioned. 2000 MU was used as under calibration conditions, this would deliver a maximum dose of 20 Gy to the film, the maximum dose to which the film is sensitive. While due to the reduced field size (4x4 instead of 10x10, even before the collimation to a 3 mm beam) it was highly unlikely that the dose would reach this level, I determined it would be better to not risk overexposing the film.

The film was then scanned using a Epson v700 scanner and imported into FilmQA Pro (Ashland Advanced Materials) for analysis. The calibration curve obtained for the the ^{192}Ir measurements was again used to convert from optical density to dose.

4.4 Results

4.4.1 2 MV simulations

Tables 4.1 and 4.2 show the PVDRs and dose rates, respectively, for the 2 MV system for different center-to-center spacings. As with the isotope systems, the PVDR increases with increased center-to-center spacing while the dose rate remains relatively unaffected. The

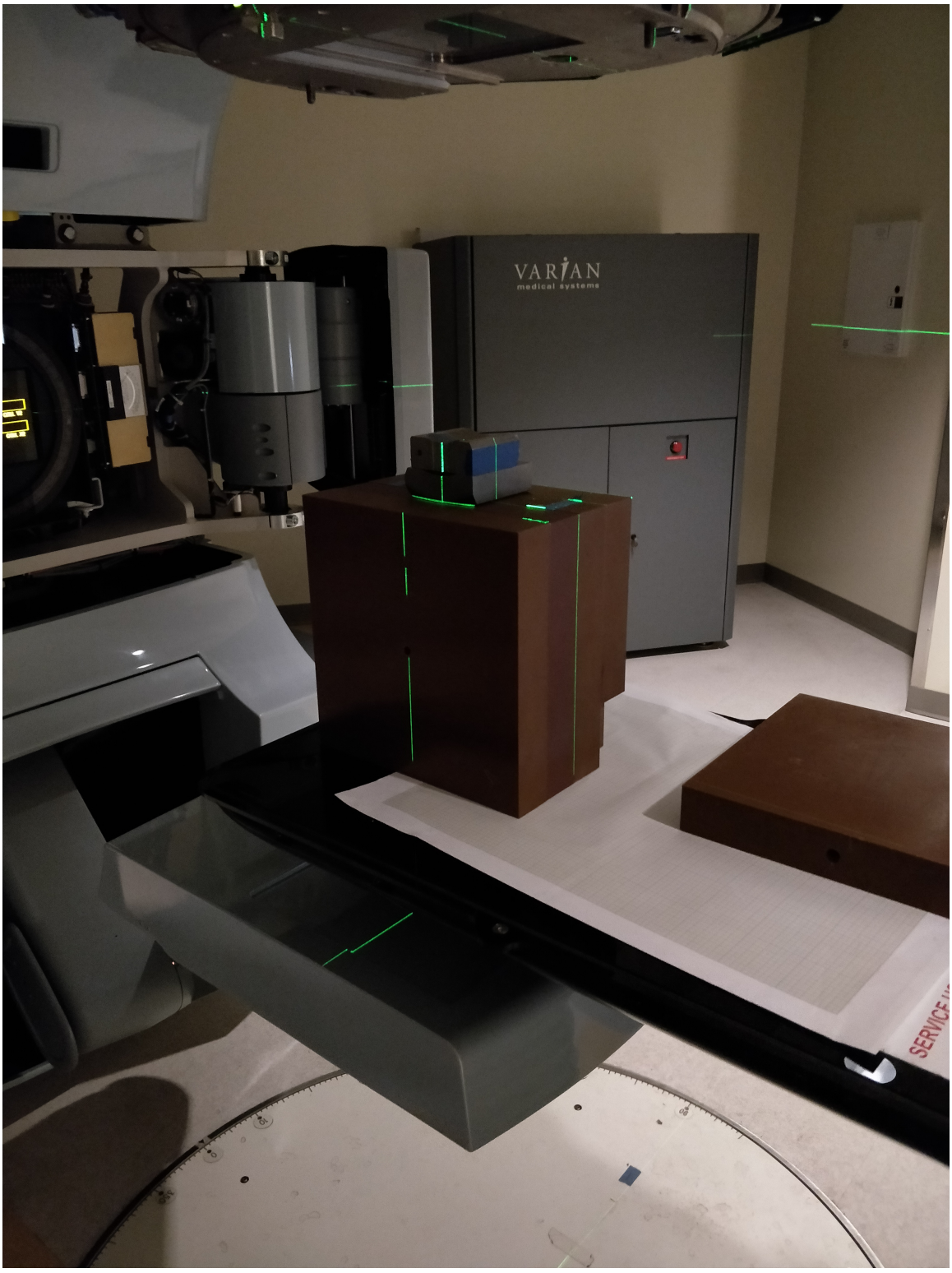

Figure 4.2: Set up for the 6 MV irradiation. The MV imager was used as a secondary check to verify the alignment between the two halves of the collimator. The solid water was set to be at 100 SSD.

dose rate for each beam is significantly higher for the 2 MV beam compared to the isotope based cases, with a dose rate at depth of approximately 7 Gy/min. However, based on the proposed design of the system where an electron beam is scanned across each collimator hole, each of which holds a target, this is truly the dose rate in a single beam, so the effective dose rate (the dose rate averaged over the full treatment time) would approximately be the values in the table divided by the number of beams used for treatment. These dose rates include the contribution from cross-talk from adjacent beams, so the dose rate would be slightly lower for holes on the edge.

Table 4.1: PVDR results obtained with MCNP6 for different center-to-center spacings from the 2 MV beam

Depth in phantom (cm)	PVDR				
	4 mm c-t-c	6 mm c-t-c	8 mm c-t-c	10 mm c-t-c	12 mm c-t-c
0.5	22.7	59.3	94.2	130.5	165.9
2.5	7.1	31.9	56.8	77.0	101.3
5.0	1.3	13.4	31.6	49.3	60.7
7.5	0.7	4.6	17.8	29.9	43.7
10.0	0.6	1.5	8.7	19.0	27.4

Table 4.2: Beam centerline Dose rate per beam using maximum current (0.4 mA) for different center-to-center spacings from the 2 MV simulations

Depth in phantom (cm)	Dose rate (Gy/min)				
	4 mm c-t-c	6 mm c-t-c	8 mm c-t-c	10 mm c-t-c	12 mm c-t-c
0.5	77.3	76.6	76.3	76.1	76.1
2.5	42.7	42.1	41.9	41.7	41.7
5.0	22.9	22.2	22.0	21.9	21.8
7.5	13.5	12.7	12.5	12.4	12.4
10.0	8.9	7.7	7.5	7.4	7.4

As an example, assuming a prescription dose of 15 Gy to 10 cm and using the 8 mm c-t-c spacing, this leads to a treatment time of 2 minutes per beam. If we limit treatment time to 30 minutes, not including set up time, this means that the largest number of beams that could be used is 15. Using Equation 4.1, which gives the number of holes, N, needed to treat an area with radius r using a hexagonal array with a center-to-center spacing of ctc, this would treat an area with a radius somewhere between 1-2 c-t-c distances, or between 8 and 16 mm.

$$N = 1 + 6 \times \sum_{n=1}^{i} n$$
$$where\ i = \left\lfloor \frac{r}{ctc} \right\rfloor \tag{4.1}$$

And while the dose in-beam at the surface would receive a high dose of 152.6 Gy, the valley region would only receive 1.6 Gy due to the high PVDR.

4.4.2 6 MV film measurements

While FilmQA Pro does not output a 2D dose map, Figure 4.3 shows the film itself after irradiation. The film was irradiated with a 4x4 field, the extend of the field can be seen around the main beam as a slight darkening, caused by leakage through the collimator. Compared to the ^{192}Ir film, the beam remains well defined throughout the entire length of the film.

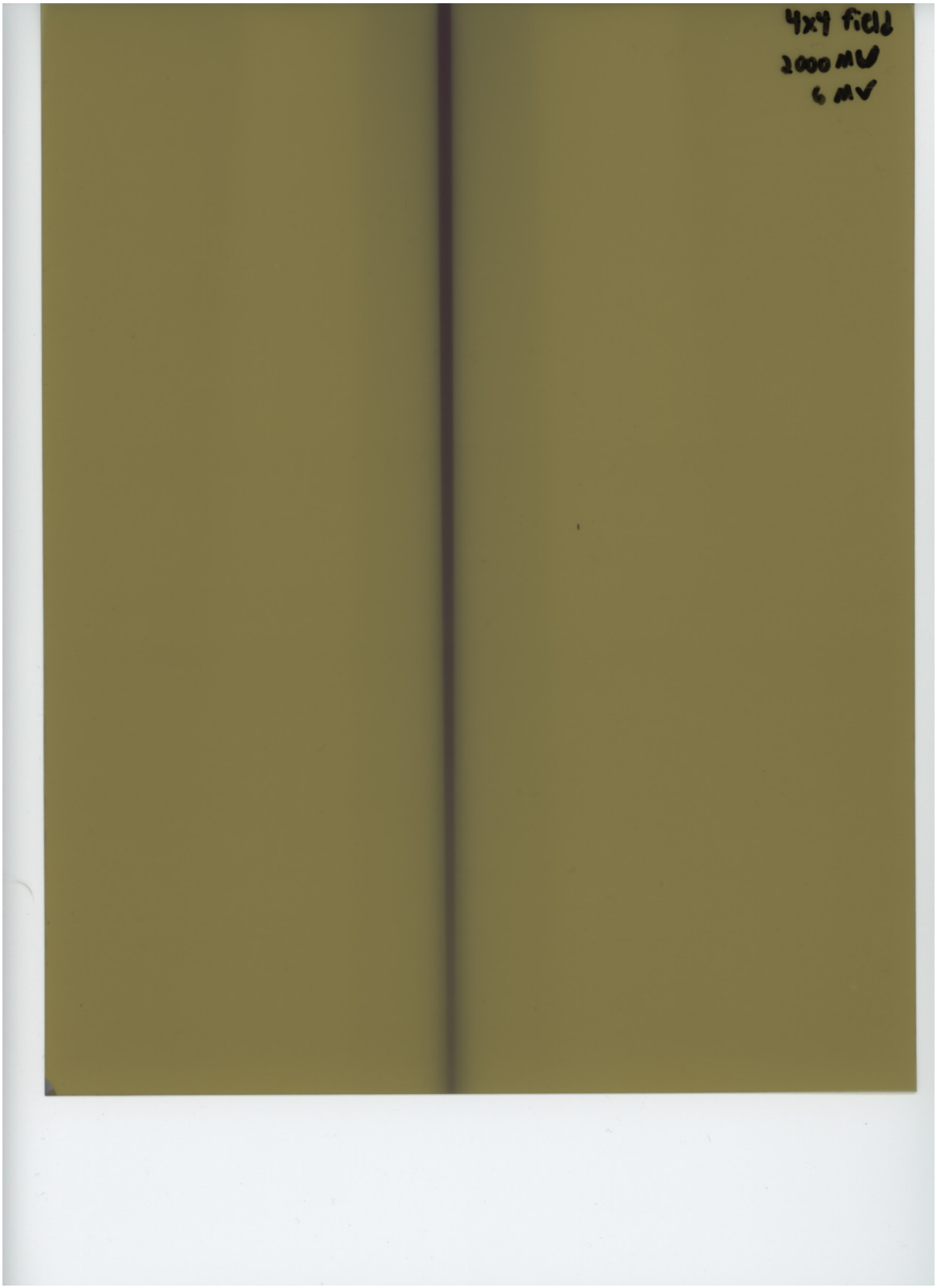

Figure 4.3: 6 MV film, post irradiation

For the 6 MV films, the PVDRs were calculated by dividing the dose at center-line by the dose measured at a distance equal to half of the center-to-center distance off axis. For all of these measurements, the dose was averaged over 10 pixels to reduce the influence of noise on the results. Based on the film resolution, this averaged over a distance of 0.3 mm, which is small relative to the beam size. The PVDR results can be seen in Table 4.3. The PVDR results were based on superpositions of the single hole results obtained from film measurement.

Table 4.3: PVDR results obtained from film measurement for different center-to-center spacings from 6 MV film irradiation

Depth in phantom (cm)	PVDR			
	6 mm c-t-c	8 mm c-t-c	10 mm c-t-c	12 mm c-t-c
0.5	6.0	8.1	9.7	10.7
2.5	4.9	6.6	8.2	9.5
5.0	5.1	7.3	9.3	11.0
7.5	5.5	7.7	9.9	11.8
10.0	5.2	7.3	9.4	11.3
12.5	4.7	6.7	8.8	10.6
15.0	4.1	5.8	7.5	9.0
17.5	3.8	5.3	6.9	8.5
20.0	3.2	4.5	5.9	7.4

As the films were irradiated to 2000 MU using a dose rate of 600 MU/min, the doses measured from the film were divided by $\frac{2000\,MU}{600\,MU/min} = 3.33\,min$ to give the dose rate in Gy/min. The dose rate at various depths can be seen in Table 4.4.

Table 4.4: Beam centerline dose rate (using 600 MU/min)

Depth (cm)	Dose rate (Gy/min)
0.5	2.00
2.5	1.58
5.0	1.50
7.5	1.38
10.0	1.19
12.5	1.05
15.0	0.91
17.5	0.77
20.0	0.60

4.5 Discussion

4.5.1 2 MV beams

From a PVDR standpoint, the 2 MV beams performed quite well, with similar PVDRs to the ^{60}Co at the surface. As with the ^{60}Co, the PVDR stayed fairly high throughout the volume of interest which, while not necessarily an issue, would not give a close to uniform dose to a tumor volume. As current MV GRID treatments give beneficial clinical results with lower PVDRs and similarly non-uniform dose to the tumor volume while using larger beam sizes, it is likely that the dose distribution resulting from the 2 MV beams would result in at worst comparable clinical results and at best similar tumor control with increased healthy tissue recovery. As with the photon-emitting radioisotope cases, the divergence of the beam causes the dose profile to be close to uniform at certain depths for particular center-to-center distances, which could be used to deny a tumor at these depths any advantage from the spatial fractionation of the dose. As touched on in the results section, the dose rate, while it appears to be sufficiently high from Table 4.2, is of somewhat more concern. This stems from that the given dose rate is per beam, not for the overall system, meaning that the time needed to deliver the prescription dose using the given dose rates would need to be multiplied by the number of beams, as the electron beam would need to be scanned across each of the targets in series. While this is doable for small field sizes, as mentioned

earlier the number of holes increases by the function given by Equation 4.1.

This means that the treatment time will increase proportionally with this function, again leading to drastically increased treatment times for larger fields. As with the isotopes, this restriction on the dose rate limits the applicability of the system, but at least the MV system has the potential of having short treatment times for small fields and does not require the use of multiple kiloCuries of radioactive sources.

4.5.2 6 MV beam

While not a significant improvement from current MV GRID, the PVDRs obtained from the 6 MV treatment were up to two times higher than the current practice. Of course, this does come with some caveats. The ratio of center-to-center spacing to beam diameter (which is proportional to the closed to open ratio of the collimator) is higher in almost all cases investigated in the work (2-4 for 6 to 12 mm c-t-c) than for the GRID collimators produced today, which have a ctc:diameter ratio of 2. For the 6 mm c-t-c beams, the minibeam PVDR is approximately equal to the standard GRID block. Additionally, the collimator used in this study has a density thickness of approximately 112.2 g/cm^2 ($18.7\,g/cm^3 \times 6\,cm$) and a Z of 74, while the standard brass GRID block produced by .decimal (Sanford, FL) has an approximate density thickness of 65.2 g/cm^2 ($8.55\,g/cm^3 \times 7.62\,cm$) and a Z_{eff} of approximately 30. Based on this, one would expect the tungsten collimator to give a higher PVDR than the brass.

The dose rate, as is the norm for this work, is concerning. While standard MV GRID collimator has a output factor of approximately 0.89 (that is, the dose to D_{max} for a given number of MU is 89% of what it would be with an open field). Comparatively, the output factor for the 3 mm beam size is 0.38 (using the reduced D_{max} depth of 0.8 cm for the 3 mm beam), a comparative 57% decrease in output. This would lead to treatment times that were approximately twice as long, which would mean there would be a greater risk of patient motion that would blur the minibeams. However, this treatment time would still

be shorter than GRID treatments administered using the MLC, which are on average 5 times longer than treatments administered with a static block [18, 23]. Given this, it is potentially feasible to use a GRID block with 3 mm holes from a dosimetric prospective, though practically it would be challenging for the reasons mentioned below.

4.6 Conclusions

Both of the MV minibeam techniques evaluated do show some promise for clinical application. In both cases, the PVDRs at the surface were at or above the values found for clinically used MV GRID treatments, which implies that the normal tissue recovery would at worst be the same as these treatments. As shown in Hopewell et. al. [2], we have reason to believe that the smaller beam size of 2-3 mm would lead to a radiobiological advantage. The dose rate, while not as high as hoped, is still high enough in most cases (excluding large fields for the 2 MV beams) to be clinically viable, as the treatment times would be less than for those MLC administered GRID treatments [18, 23, 16]. However, the technical implementation for both would be challenging. The 2 MV beams would require the development of a 2 MeV electron accelerator that would also need to be capable of steering the beam onto the targets located at the top of each collimator hole. Each of these targets would also need to be cooled to assure that the incident electron beam did not melt either the target or the attached filter. Furthermore, due to the small beam size, performing calibration measurements for such a system would be difficult, and would almost certainly require the use of radiochromic film. While the makers of the EBT3 film used in this work assure measured dose accuracy within 1% [47], the practice standards set by the American Association of Physicists in Medicine (AAPM) specify that only an ion chamber in water should be used for calibrating clinical linear accelerators [58]. Another concern for both would be machining the tungsten collimators. The collimators would likely have to be machined in at least two separate parts, as even the 3 cm tungsten pieces stretched the limits of the machine shop, requiring tens of minutes for each piece and two drill bits as one broke

during the process. To cover a treatment area of 10x10 cm would require a minimum of 64 holes (using a c-t-c of 12 mm) all the way up to 625 holes (for 4 mm c-t-c) or 256 holes (for 6 mm c-t-c). In the case of the 6 MV collimator, these holes would have to be divergent to match the beam coming from the linear accelerator (to avoid the ”doming” effect shown for the smaller electron hole sizes in chapter 2), adding another degree of complexity. One way around this problem could be to switch the collimator material to something that would be easier to machine, such as brass or Cerrobend. The tradeoff would be either increased leakage (due to a decrease in both the Z_{eff} and the density thickness) if the thickness was kept the same, or decreased output if the collimator thickness was increased due to the $1/r^2$ effect (for the 2 MV case, as the targets would be moved further from the surface) and reduce solid angle (for both). Should future research look into developing these systems for applied clinical use, identifying a new collimator material and design that would minimize the drawbacks of not using tungsten should be a high priority.

CHAPTER 5
CONCLUSIONS AND FUTURE WORK

5.1 Conclusions

Overall, the methodologies explored in this work showed some promise, though in each case this was tempered by several limitations. For the electron GRID, the PVDRs obtained were on the order of those achieved in commercial MV GRID treatment systems, and the lateral scattering of the electrons did lead to a more uniform dose below the skin surface. However, while the electrons did meet the goal of minimizing exit dose, and therefore theoretically sparing any radiosensative structures below the treatment volume, the effective treatment depth was also reduced to a point that would make treating the entire volume of a bulky tumor difficult at best and impossible at worst. Still, there are theoretically some cases where this could be applied, though the restrictions on what would make an ideal case (a tumor that is bulky in two dimensions but is relatively thin in the depth dimension and is located above an organ-at-risk) are more limiting than was initially hoped.

For the radioisotope-based photon minibeams, it was indeed possible to create 2-3 mm diameter beams with relatively high PVDRs using both ^{192}Ir and ^{60}Co. Unfortunately, the dose rate obtained with the majority of the configurations investigated was relatively low, around 0.4-0.6 Gy/min, and the treatment of even a small area would require kiloCuries worth of the isotopes. The convergent ^{60}Co geometry showed the most promise of all of the cases, with a respectable dose rate of approximately 3 Gy/min in the target volume, and the use of less activity than a GammaKnife unit (abet spread across significantly fewer sources).

Finally, the MV minibeams followed a similar pattern as the isotopes, achieving excellent PVDRs but hampered by low effective dose rates. The 2 MV minibeams additionally

added in a large degree of technical complexity, as a 2 MeV electron accelerator would not only have to be produced, but would need to have a steering system accurate enough to quickly scan between an array of 2 mm targets. The 6 MV measurement did show some promise, though again hampered by a low dose rate relative to the typical dose prescription for GRID treatments. Still, as a modification of an existing clinical treatment, it also would almost certainly be the easiest to bring into use for patient treatments.

5.2 Future work

As noted above, the two most promising areas for future work would be the convergent ^{60}Co isotope treatment and the 6 MV GRID collimator. In the case of the ^{60}Co system, likely future directions would be to evaluate the feasibility of obtaining and handling the activity of sources needed to make the system work and/or look into expanding the number of beam lines to both lower the dose per beam and lower the activity per source. Ideally, the largest number of beam lines that still would allow for the system to be able to change position around the patient would be used, as the more beam lines the less difficult there would be in handling any individual source, but using so many as to make the machine fixed would render it effectively identical to existing GammaKnife units.

For the MV minibeams, the main challenge would be to find a way to machine a properly divergent collimator. As mentioned in Chapter 4, even machining a single straight hole through half of the effective thickness of the tungsten collimator took a considerable amount of time and effort. As such, it is likely a different, more easily machined collimator material would be used instead (with hopefully minimal trade off in the PVDR and dose rate). The other issue would be to find the ideal trade-off in positioning of the collimator, as if it is brought closer to the head of the machine, the hole size would need to be decreased to assure the projection on the patient's skin does not exceed 5 mm while positioning it closer to the patient would require a more complex mounting apparatus and would introduce concerns about collisions with the patient.

Appendices

APPENDIX A

DATA PROCESSING

A.1 Electron film analysis code

```
function [out,len,wid]=Film2Dose(fname,channel,energy)

calMUs=600; %MUs used to generate the films

switch channel %color channel to be read; red is best for dose used
    case 'R'
        idx=1;
    case 'G'
        idx=2;
    case 'B'
        idx=3;
    otherwise
        error('Channel input must be R, G or B')
end

switch energy
    case 15
        energyname = 'GaTech_3003RC.tif';
        MU2Gy=.01009; %MU to gray conversion from TEC3
                      %calc book for 10x10 field
    case 18
```

```
        energyname = 'GaTech_13003RC.tif';
        MU2Gy=.01017;
    case 22
        energyname = 'GaTech_23003RC.tif';
        MU2Gy=.01029;
    otherwise
        error('Energy not used')
end

Gy=calMUs*MU2Gy; %converts MUs to grays

caldata=imread(energyname);
caldata=im2double(caldata(:,:,idx));
[mc,nc]=size(caldata);
%caldata=ones(mc,nc)-caldata;
%caldata=caldata-backg;
calLen=linspace(0,25.3,nc+1);
calLen=calLen(1:end-1);
calPDD=caldata(ceil(mc/2),:);
tablePDD=electronPDDs(energy);
newCal=[zeros(length(tablePDD),1) .01*Gy*tablePDD(:,2)];
%tablePDD is in percent, hence the .01

for r=1:length(tablePDD)
    [~,ix]=min(abs(calLen-tablePDD(r,1)));
    newCal(r,1)=calPDD(ix);
    % newCal is [OD dose] with repeats
```

```
end

allUnique=unique(.01*Gy*tablePDD(:,2));
%finds all the unique dose levels
finalCal=[zeros(length(allUnique),1) allUnique];

for q=1:length(allUnique)
    holder=newCal(newCal(:,2)==allUnique(q),1);
    finalCal(q,1)=holder(1);
end

finalCal(2:end+1,:)=finalCal;
finalCal(1,:)=[0 0];

%data=AlignFilm(fname);
%cftool(finalCal(:,1),finalCal(:,2));

if energy==22
    yholder=newCal(9:end,2);
    xholder=newCal(9:end,1);
    [fitresult gof]=createFit(xholder,yholder);
elseif energy==18
    yholder=newCal(16:end,2);
    xholder=newCal(16:end,1);
    [fitresult gof]=createFit(xholder,yholder);
else
    [fitresult gof]=createFit(finalCal(:,1),finalCal(:,2));
```

```
end

data=imread([fname '.tif']);
cdata=im2double(data(:,:,idx));
[m,n]=size(cdata);
%cdata=ones(m,n)-cdata;
%cdata=cdata-backg;
%cdata(cdata<0)=0;
out=reshape(fitresult(cdata),m,n);

if m>n
    len=linspace(0,25.3,m+1);
    len=len(1:end-1)';
    wid=linspace(0,20.32,n+1);
    wid=wid(1:end-1)';
    wid=wid-wid(round(length(wid)/2));
else
    len=linspace(0,20.32,m+1);
    len=len(1:end-1)';
    len=len-len(round(length(len)/2));
    wid=linspace(0,25.3,n+1);
    wid=wid(1:end-1)';
end
figure;
surf(wid,len,out,'EdgeColor','none');
view(90,90)
h1=colorbar;
```

```
xlabel('Depth (cm)','FontSize',14)
ylabel('Width (cm)','FontSize',14)
ylabel(h1,'Dose (Gy)','FontSize',14)
xlim([min(wid) max(wid)]);
ylim([min(len) max(len)]);
%title(['Dose using ' num2str(calMUs) ' MUs']);
figure;
out2=100*out/Gy;
surf(wid,len,out2,'EdgeColor','none');
view(90,90)
colorbar
xlabel('Depth (cm)')
ylabel('Width (cm)')
title('Percent of max dose');
figure;
title('Film to dose conversion');
subplot(1,2,1)
imshow([fname '.tif']);
title('Film')
subplot(1,2,2)
surf(wid,len,out,'EdgeColor','none');
view(0,90)
h1=colorbar;
h1.Label.String='Dose (Gy)';
title('Dose')
xlim([0 25.3]);
ylim([0 20.32]);
```

```
set(gca,'XTickLabel',{});
set(gca,'YTickLabel',{});
end

function [fitresult, gof] = createFit(x, y)
%CREATEFIT(X,Y)
%  Create a fit.
%
%  Data for 'untitled fit 1' fit:
%      X Input : x
%      Y Output: y
%  Output:
%      fitresult : a fit object representing the fit.
%      gof : structure with goodness-of fit info.
%
%  See also FIT, CFIT, SFIT.

%  Auto-generated by MATLAB on 02-Jun-2016 15:44:44


%% Fit: 'untitled fit 1'.
[xData, yData] = prepareCurveData( x, y );

% Set up fittype and options.
% opts = fitoptions( 'Method', 'NonlinearLeastSquares' );
% opts.Display = 'Off';
% opts.StartPoint = ;
```

```
ft = fittype( 'a+b/(x-c)', 'independent', 'x', 'dependent', 'y' );



% Fit model to data.
[fitresult, gof] = fit( xData, yData, ft, 'StartPoint',
     [0.54630955549147 0.0211108546124322 0]);

% Plot fit with data.
figure( 'Name', 'Calibration Curve' );
h = plot( fitresult, xData, yData );
legend( h, 'Dose vs. Optical Density', 'Calibration Curve', 'Location',
% Label axes
xlabel('Optical Density');
ylabel('Dose');
grid on
end
```

A.2 Code for writing, running, and analyzing MCNP code for Ir-192 minibeams

```
function MCNPwriterP(coll,c2c,shape,varargin)
collThickness=7.5;
NPS=100000000;
if length(varargin)==1
    sourceS=varargin{1};
else
    sourceS=coll;
end
standOff=0;
```

```
collDen=9.4;
coll=coll*(collThickness/(standOff+collThickness));
currentFolder=pwd;
if standOff~=0
    if exist([pwd '/' num2str(standOff*10) 'mmST'],'dir')~=7
        mkdir([pwd '/' num2str(standOff*10) 'mmST'])
    end
    currentFolder=[pwd '/' num2str(standOff*10) 'mmST'];
end
cd('/home/labuser/MCNP/MCNP_CODE/MCNP6')
delete('out*')
delete('runt*')
res=.05;
if strcmpi(shape(1),'t') || strcmpi(shape(1),'s')
    type='T';
    % Opens and writes file for center beam
    fname1=['IrCenterBeam' num2str(ceil(coll)) 'mmTP.txt'];
    mdata1=['IrCenter' num2str(ceil(coll)) 'mmTubeP'];
    fid=fopen(fname1,'w');
    fprintf(fid,['Center beam,' num2str(ceil(coll)) 'mm Tube Collimato
        ' num2str(c2c) 'mm C2C spacing P\n'...
    fprintf(fid,'c Cell Card\n');
    fprintf(fid,'1 1 -0.001225  -1 2 3 IMP:p=1 IMP:e=0\n');
    fprintf(fid,'2 2 -1  -2 IMP:p=10 IMP:e=10\n');
    fprintf(fid,['3 3  -' num2str(collDen) '  -3 5 6 IMP:p=0 IMP:e=0\n
    fprintf(fid,'4 1 -0.001225  -4 5 IMP:p=1 IMP:e=0\n');
    fprintf(fid,'5 4 -22.56  -5 IMP:p=1 IMP:e=0\n');
```

```
fprintf(fid,'6 0     1  IMP:p=0 IMP:e=0\n');
fprintf(fid,['7 3  -' num2str(collDen) '  -6 4 5 IMP:p=1 IMP:e=0\n
fprintf(fid,'\n');
fprintf(fid,'c Surface Card\n');
fprintf(fid,['1 RPP  -10 10  -10 10  -10 ' num2str(10+standOff+2*co
     ' $ air\n']);
fprintf(fid,'2 RPP  -5 5  -5 5 -5 10 $ water\n');
fprintf(fid,['3 RPP  -2.5 2.5  -2.5 2.5  ' num2str(10+standOff) '
     ' num2str(10+standOff+2*collThickness) ' $ collimator\n']);
fprintf(fid,['4 RCC  0 0 ' num2str(10+standOff) '  0 0 ' num2str(co
      ' num2str(coll/20) ' $ hole\n']);
fprintf(fid,['5 RCC  0 0 ' num2str(10+collThickness-.1+standOff) '
      num2str(sourceS/20) ' $ source\n']);
fprintf(fid,['6 RCC  0 0 ' num2str(10+standOff) '  0 0 ' num2str(co
      ' num2str(coll/20+.2) ' $ important area around hole\n']);
fprintf(fid,'\n');
fprintf(fid,'Mode p e\n');
fprintf(fid,['SDEF ERG=d1 POS=0 0 ' num2str(10+collThickness-.1+sta
     AXS=0 0 1 EXT=D4 RAD=D5 PAR=2 VEC=0 0 -1 DIR=D6\n']);
fprintf(fid,'SI1 L .317 .468\n');
fprintf(fid,'SP1   .81  .49\n');
fprintf(fid,'SI4 0 .2\n');
fprintf(fid,'SP4 0 1\n');
fprintf(fid,['SI5 0 ' num2str(coll/20) '\n']);
fprintf(fid,'SP5 -21 1 \n');
ang=atan((coll/2)/(collThickness*10/2))+.1;
fprintf(fid,['SI6 -1 ' num2str(cos(ang)) ' 1\n']);
```

```
fprintf(fid,['SP6 0 ' num2str((2-(1-cos(ang)))/2) ' ' num2str((1-co
fprintf(fid,'SB6 0 0 1\n');
fprintf(fid,'TMESH\n');
fprintf(fid,'   RMESH13  \n');
fprintf(fid,['   CORA13 -' num2str(c2c/10+1) ' ' num2str(((c2c/10)+
      num2str(c2c/10+1) '\n']);
fprintf(fid,['   CORB13 -' num2str(res/2) ' ' num2str(res/2) '\n']);
fprintf(fid,['   CORC13 -5 ' num2str((15/res)-1) 'i 10\n']);
fprintf(fid,'  ENDMD\n');
fprintf(fid,'M1   008016 -.231781   006012 -.000124   007014 -.7552
fprintf(fid,'M2   008016 1 001000 2\n');
%fprintf(fid,'M3   072000 1\n'); % tungsten
fprintf(fid,'M3   083000 -.5  082000 -.267  050000 -.133  048000 -
fprintf(fid,'M4   077192 1\n');
fprintf(fid,['NPS ' num2str(NPS)]);
fclose(fid);

%Opens and writes file for diagonal beam
fname2=['IrDiagBeam' num2str(ceil(coll)) 'mmTP.txt'];
mdata2=['IrDiag' num2str(ceil(coll)) 'mmTubeP'];
newLoc=(c2c/10)/sqrt(2);
fid=fopen(fname2,'w');
fprintf(fid,['Diag beam,' num2str(ceil(coll)) 'mm Tube Collimator,
      num2str(c2c) 'mm C2C spacing P\n']);
fprintf(fid,'c Cell Card\n');
fprintf(fid,'1 1 -0.001225  -1 2 3 IMP:p=1 IMP:e=0\n');
fprintf(fid,'2 2 -1  -2 IMP:p=10 IMP:e=10\n');
```

```
fprintf(fid,['3 3  -' num2str(collDen) '  -3 5 6 IMP:p=0 IMP:e=0\n'
fprintf(fid,'4 1 -0.001225  -4 5 IMP:p=1 IMP:e=0\n');
fprintf(fid,'5 4 -22.56  -5 IMP:p=1 IMP:e=0\n');
fprintf(fid,'6 0     1  IMP:p=0 IMP:e=0\n');
fprintf(fid,['7 3  -' num2str(collDen) '  -6 5 4 IMP:p=1 IMP:e=0\n'
fprintf(fid,'\n');
fprintf(fid,'c Surface Card\n');
fprintf(fid,['1 RPP  -10 10  -10 10  -10 ' num2str(10+standOff+2*co
fprintf(fid,'2 RPP  -5 5  -5 5 -5 10 $ water\n');
fprintf(fid,['3 RPP  ' num2str(newLoc-2.5) ' ' num2str(newLoc+2.5)
    num2str(newLoc+2.5) '  ' num2str(standOff+10) ' ' num2str(10+s
fprintf(fid,['4 RCC  ' num2str(newLoc) ' ' num2str(newLoc) ' ' num2
     num2str(collThickness+.15) '  ' num2str(coll/20) ' $ hole\n']
fprintf(fid,['5 RCC  ' num2str(newLoc) ' ' num2str(newLoc) ' ' num2
     '  0 0 .2  ' num2str(sourceS/20) ' $ source\n']);
fprintf(fid,['6 RCC  ' num2str(newLoc) ' ' num2str(newLoc) ' ' num2
    ' num2str(collThickness+.15) '  ' num2str(coll/20+.2) ' $ impo
fprintf(fid,'\n');
fprintf(fid,'Mode p e\n');
fprintf(fid,['SDEF ERG=d1 POS=' num2str(newLoc) ' ' num2str(newLoc)
     '\n     AXS=0 0 1 EXT=D4 RAD=D5 PAR=2 VEC=0 0 -1 DIR=D6\n']),
fprintf(fid,'SI1 L .317 .468\n');
fprintf(fid,'SP1   .81  .49\n');
fprintf(fid,'SI4 0 .2\n');
fprintf(fid,'SP4 0 1\n');
fprintf(fid,['SI5 0 ' num2str(coll/20) '\n']);
fprintf(fid,'SP5 -21 1 \n');
```

```
    ang=atan((coll/2)/(collThickness*10/2))+.1;
    fprintf(fid,['SI6 -1 ' num2str(cos(ang)) ' 1\n']);
    fprintf(fid,['SP6 0 ' num2str((2-(1-cos(ang)))/2) ' ' num2str((1-co
    fprintf(fid,'SB6 0 0 1\n');
    fprintf(fid,'TMESH\n');
    fprintf(fid,'   RMESH13  \n');
    fprintf(fid,['   CORA13 -' num2str(c2c/10+1) ' ' num2str(((c2c/10)+
    fprintf(fid,['   CORB13 -' num2str(res/2) ' ' num2str(res/2) '\n']);
    fprintf(fid,['   CORC13 -5 ' num2str((15/res)-1) 'i 10\n']);
    fprintf(fid,'  ENDMD\n');
    fprintf(fid,'M1   008016 -.231781   006012 -.000124   007014 -.7552
    fprintf(fid,'M2   008016 1 001000 2\n');
    %fprintf(fid,'M3   072000 1\n'); %tungsten
    fprintf(fid,'M3   083000 -.5  082000 -.267  050000 -.133  048000 -
    fprintf(fid,'M4   077192 1\n');
    fprintf(fid,['NPS ' num2str(NPS)]);
    fclose(fid);

else
    type='F';
    fname1=['IrCenterBeam' num2str(ceil(coll)) 'mmF.txt'];
    mdata1=['IrCenter' num2str(ceil(coll)) 'mmFunnel'];
    fid=fopen(fname1,'w');
    fprintf(fid,['Center beam,' num2str(ceil(coll)) 'mm Funnel Collimat
    fprintf(fid,'c Cell Card\n');
    fprintf(fid,'1 1 -0.001225  -1 2 3 IMP:p=1 IMP:e=0\n');
    fprintf(fid,'2 2 -1  -2 IMP:p=10 IMP:e=10\n');
```

```
fprintf(fid,['3 3  -' num2str(collDen) '  -3 6 IMP:p=0 IMP:e=0\n']
fprintf(fid,'4 1 -0.001225  -4 5 IMP:p=1 IMP:e=0\n');
fprintf(fid,'5 4 -22.56  -5 IMP:p=1 IMP:e=0\n');
fprintf(fid,'6 0     1  IMP:p=0 IMP:e=0\n');
fprintf(fid,['7 3  -' num2str(collDen) '  -6 4 5 IMP:p=1 IMP:e=0\n
fprintf(fid,'\n');
fprintf(fid,'c Surface Card\n');
fprintf(fid,['1 RPP  -10 10  -10 10  -10 ' num2str(10+standOff+2*co
fprintf(fid,'2 RPP  -5 5  -5 5 -5 10 $ water\n');
fprintf(fid,['3 RPP  -2.5 2.5  -2.5 2.5  ' num2str(standOff+10) ' '
     num2str(10+standOff+collThickness*2) ' $ collimator\n']);
fprintf(fid,['4 TRC  0 0 ' num2str(standOff+10) '  0 0 ' num2str(co
     num2str(coll/20) ' ' num2str(sourceS/20) ' $ hole\n']);
fprintf(fid,['5 RCC  0 0 ' num2str(10+collThickness-.1+standOff) '
      $ source\n']);
fprintf(fid,['6 TRC  0 0 ' num2str(standOff+10) '  0 0 ' num2str(co
      num2str(coll/20+.2) ' ' num2str(sourceS/20+.2) ' $ important
fprintf(fid,'\n');
fprintf(fid,'Mode p e\n');
fprintf(fid,['SDEF ERG=d1 POS=0 0 ' num2str(10+collThickness-.1+sta
     AXS=0 0 1 EXT=D4 RAD=D5 PAR=2 VEC=0 0 -1 DIR=D6\n']);
fprintf(fid,'SI1 L .317 .468\n');
fprintf(fid,'SP1   .81  .49\n');
fprintf(fid,'SI4 0 .2\n');
fprintf(fid,'SP4 0 1\n');
fprintf(fid,['SI5 0 ' num2str(sourceS/20) '\n']);
fprintf(fid,'SP5 -21 1 \n');
```

```
ang=atan((coll/2)/(collThickness*10/2))+.1;
fprintf(fid,['SI6 -1 ' num2str(cos(ang)) ' 1\n']);
fprintf(fid,['SP6 0 ' num2str((2-(1-cos(ang)))/2) ' ' num2str((1-co
fprintf(fid,'SB6 0 0 1\n');
fprintf(fid,'TMESH\n');
fprintf(fid,'   RMESH13  \n');
fprintf(fid,['   CORA13 -' num2str(c2c/10+1) ' ' num2str(((c2c/10)+
fprintf(fid,['   CORB13 -' num2str(res/2) ' ' num2str(res/2) '\n']);
fprintf(fid,['   CORC13 -5 ' num2str((15/res)-1) 'i 10\n']);
fprintf(fid,'  ENDMD\n');
fprintf(fid,'M1   008016 -.231781   006012 -.000124   007014 -.7552
fprintf(fid,'M2   008016 1 001000 2\n');
%fprintf(fid,'M3   072000 1\n'); %tungsten
fprintf(fid,'M3   083000 -.5  082000 -.267  050000 -.133  048000 -
fprintf(fid,'M4   077192 1\n');
fprintf(fid,['NPS ' num2str(NPS)]);
fclose(fid);

fname2=['IrDiagBeam' num2str(ceil(coll)) 'mmFP.txt'];
mdata2=['IrDiag' num2str(ceil(coll)) 'mmFunnelP'];
newLoc=(c2c/10)/sqrt(2);
fid=fopen(fname2,'w');
fprintf(fid,['Center beam,' num2str(ceil(coll)) 'mm Funnel Collimat
fprintf(fid,'c Cell Card\n');
fprintf(fid,'1 1 -0.001225  -1 2 3 IMP:p=1 IMP:e=0\n');
fprintf(fid,'2 2 -1  -2 IMP:p=10 IMP:e=10\n');
fprintf(fid,['3 3  -' num2str(collDen) '  -3 6 IMP:p=0 IMP:e=0\n']);
```

```
fprintf(fid,'4 1 -0.001225  -4 5 IMP:p=1 IMP:e=0\n');
fprintf(fid,'5 4 -22.56  -5 IMP:p=1 IMP:e=0\n');
fprintf(fid,'6 0     1  IMP:p=0 IMP:e=0\n');
fprintf(fid,['7 3  -' num2str(collDen) '  -6 4 5 IMP:p=1 IMP:e=0\n
fprintf(fid,'\n');
fprintf(fid,'c Surface Card\n');
fprintf(fid,['1 RPP  -10 10  -10 10  -10 ' num2str(10+standOff+2*co
fprintf(fid,'2 RPP  -5 5  -5 5 -5 10 $ water\n');
fprintf(fid,['3 RPP  ' num2str(newLoc-2.5) ' ' num2str(newLoc+2.5)
    num2str(newLoc+2.5) '  ' num2str(standOff+10) ' ' num2str(10+s
fprintf(fid,['4 TRC  ' num2str(newLoc) ' ' num2str(newLoc) ' ' num2
    num2str(collThickness+.15) '  ' num2str(coll/20) ' ' num2str(s
fprintf(fid,['5 RCC  ' num2str(newLoc) ' ' num2str(newLoc) ' ' num2
    '  0 0 .2  ' num2str(sourceS/20) ' $ source\n']);
fprintf(fid,['6 TRC  ' num2str(newLoc) ' ' num2str(newLoc) ' ' num2
    num2str(collThickness+.15) '  ' num2str(coll/20+.2) ' ' num2st
fprintf(fid,'\n');
fprintf(fid,'Mode p e\n');
fprintf(fid,['SDEF ERG=d1 POS=' num2str(newLoc) ' ' num2str(newLoc)
    '\n     AXS=0 0 1 EXT=D4 RAD=D5 PAR=2 VEC=0 0 -1 DIR=D6\n']);
fprintf(fid,'SI1 L .317 .468\n');
fprintf(fid,'SP1   .81  .49\n');
fprintf(fid,'SI4 0 .2\n');
fprintf(fid,'SP4 0 1\n');
fprintf(fid,['SI5 0 ' num2str(sourceS/20) '\n']);
fprintf(fid,'SP5 -21 1 \n');
ang=atan((coll/2)/(collThickness*10/2))+.1;
```

```
    fprintf(fid,['SI6 -1 ' num2str(cos(ang)) ' 1\n']);
    fprintf(fid,['SP6 0 ' num2str((2-(1-cos(ang)))/2) ' ' num2str((1-co
    fprintf(fid,'SB6 0 0 1\n');
    fprintf(fid,'TMESH\n');
    fprintf(fid,'   RMESH13  \n');
    fprintf(fid,['   CORA13 -' num2str(c2c/10+1) ' ' num2str(((c2c/10)+
    fprintf(fid,['   CORB13 -' num2str(res/2) ' ' num2str(res/2) '\n']);
    fprintf(fid,['   CORC13 -5 ' num2str((15/res)-1) 'i 10\n']);
    fprintf(fid,'  ENDMD\n');
    fprintf(fid,'M1   008016 -.231781   006012 -.000124   007014 -.7552
    fprintf(fid,'M2   008016 1 001000 2\n');
    %fprintf(fid,'M3   072000 1\n'); %tungsten
    fprintf(fid,'M3   083000 -.5  082000 -.267  050000 -.133  048000 -
    fprintf(fid,'M4   077192 1\n');
    fprintf(fid,['NPS ' num2str(NPS)]);
    fclose(fid);

end

system(['mcnp6 i=' fname1 ' mdata=' mdata1]);
system(['mcnp6 i=' fname2 ' mdata=' mdata2]);
if exist('outz*','file')
    delete('out*')
    delete('runt*')
end
movefile(mdata1,currentFolder);
movefile(mdata2,currentFolder);
```

```
cd(currentFolder)
dosePlotter(mdata1,mdata2,c2c,coll,sourceS,type);
end

function dosePlotter(mdata1,mdata2,c2c,coll,sourceS,type)
fnameStart=[num2str(c2c) 'mmC2C' num2str(ceil(coll)) 'mmColl' num2str(s
holder=ReadMData(mdata1);
holder=holder.Mesh;
holder=holder{1};
center=reshape(holder.Tally,[],300,1);
errorC=reshape(holder.Error,[],300,1);
holder=ReadMData(mdata2);
holder=holder.Mesh;
holder=holder{1};
diag=reshape(holder.Tally,[],300,1);
[m,n]=size(center);
[o,p]=size(diag);
if m<o
    holder=zeros(o,p);
    holder((o-m)/2+1:o-(o-m)/2,:)=center;
    center=holder;
elseif n<p
    holder=zeros(o,p);
    holder(p-n+1:p-(p-n),:)=center;
    center=holder;
end
side1=circshift(center,c2c/.5);
```

```
side2=circshift(center,-c2c/.5);
out=center+side1+side2+diag.*2+flipud(diag).*2;
switch sourceS
    case 2
        maxActivity=297.2*3.7*10^10;
    case 3
        maxActivity=668.7*3.7*10^10;
    case 4
        maxActivity=1188.8*3.7*10^10;
    case 5
        maxActivity=1857.5*3.7*10^10;
    otherwise
        maxActivity=74.3*(sourceS^2)*3.7*10^10;
end
photonsPerDecay=2;
out=out.*(maxActivity*photonsPerDecay*1.60218e-13*1000*60);
%first constant is MeVto Joule, second is g to kg, third is s to min
%out=out./mean(mean(out(floor(end/2)-4:ceil(end/2)+4,98:103)));
s=max([o p]);
t=min([o p]);
holder=zeros(s,s);
holder((round(s/2)-round(t/2)):(round(s/2)+round(t/2)-1),:)=out;
xs=(0:.05:(s-1)*.05);
xs=xs-(xs(end)/2);
ys=(s-1)*.05:-.05:0;
h1=figure;
surf(ys,xs,smoother(holder,1),'EdgeColor','none')
```

```
% title([num2str(coll) 'mm collimator, ' num2str(c2c) 'mm C2C, paralle
xlabel('Depth (cm)','fontsize',14)
ylabel('Lateral Distance (cm)','fontsize',14)
h=colorbar;
xlabel(h,'Dose Rate (Gy/min)','fontsize',14)
view(0,90)
saveas(h1,[fnameStart 'P.fig'])
saveas(h1,[fnameStart 'P.jpg'])
save([fnameStart 'PData'],'out')
save([fnameStart 'PError'],'errorC')

h2=figure;
outs=smoother(out,1);
plot(ys,outs(ceil(end/2),:))
title(['Depth dose profile ' num2str(coll) 'mm collimator, ' num2str(c2
xlabel('Depth (cm)','fontsize',14)
ylabel('Dose rate (Gy/min)','fontsize',14)
saveas(h2,[fnameStart 'PPDDS.jpg'])

h4=figure;
plot(ys,out(ceil(end/2),:))
title(['Depth dose profile ' num2str(coll) 'mm collimator, ' num2str(c2
xlabel('Depth (cm)','fontsize',14)
ylabel('Dose rate (Gy/min)','fontsize',14)
saveas(h4,[fnameStart 'PPDD.jpg'])

h3=figure;
```

```
sampleFrequency=1; %in cm
samples=0:sampleFrequency:12;
samples(1)=[];
hold on
legendlabels=cell(1,length(samples));
for r=1:length(samples)
    [~,idx]=min(abs(ys-samples(r)));
    plot(xs,outs(:,idx))
    legendlabels{r}=[num2str(samples(r)) ' cm'];
end
xlabel('Horzontal distance (cm)','fontsize',14);
ylabel('Dose rate (Gy/min)','fontsize',14)
title(['Peak to valley plot for ' num2str(coll) 'mm collimator, ' num2s
legend(legendlabels)
saveas(h3,[fnameStart 'PP2VS.jpg'])

h5=figure;
% sampleFrequency=1; %in cm
% samples=0:sampleFrequency:12;
% samples(1)=[];
samples=[.5 2.5 5 7.5 10];
hold on
legendlabels=cell(1,length(samples));
xs=(0:.05:(o-1)*.05);
xs=xs-(xs(end)/2);
for r=1:length(samples)
    [~,idx]=min(abs(ys-samples(r)));
```

```
    plot(xs,smoother(out(:,idx),1))
    legendlabels{r}=[num2str(samples(r)) ' cm'];
end
xlabel('Horzontal distance (cm)','fontsize',14);
ylabel('Dose rate (Gy/min)','fontsize',14)
%title(['Peak to valley plot for ' num2str(coll) 'mm collimator, ' num2
legend(legendlabels)
saveas(h5,[fnameStart 'PP2V.jpg'])

h6=figure;
errorC=errorC.*out;
surf(ys,xs,smoother(errorC,1),'EdgeColor','none')
title([fnameStart 'mmSource Error'])
xlabel('Depth (cm)','fontsize',14)
ylabel('Beam Width (cm)','fontsize',14)
h=colorbar;
xlabel(h,'Dose Rate (Gy/min)')
view(0,90)
saveas(h6,[fnameStart 'PE.jpg'])
end
```

REFERENCES

[1] E. Hall and C.-S. Wuu, "Radiation-induced second cancers: The impact of 3d-crt and imrt," *Int J. Radiation Oncology Biol Phys*, vol. 56, no. 1, pp. 83–88, 2003.

[2] J. Hopewell and K. Trott, "Volume effects in radiobiology as applied to radiotherapy," *Radiother Oncol*, 2000.

[3] H. Bijl, P van Luijk, R. Coppes, J. Schippers, A. Konings, and A. van der Kogel, "Unexpected changes of rat cervical spinal cord tolerance caused by inhomogeneous dose distributions," *Int. J. Radiation Oncology Biol. Phys.*, vol. 57, no. 1, pp. 274–281, 2003.

[4] H. Bijl, P van Luijk, R. Coppes, J. Schippers, A. Konings, and A. van Der Kogel, "Influence of adjacent low-dose fields on tolerance to high doses of protons in rat cervical spinal cord," *Int J Radiat Oncol Biol Phys*, vol. 64, pp. 1204–1210, 2006.

[5] T. Goorley and et al, "Initial mcnp6 release overview," *Nuclear Technology*, vol. 180, pp. 298–315, 2012.

[6] H Kohler, "Rontgentiefen therapie mit massendosen," *MMW*, vol. 56, pp. 2314–2316, 1909.

[7] F Liberson, "Value of multiperforated screen in deep x-ray therapy," *Radiology*, vol. 20, pp. 186–195, 1933.

[8] B Jolles, "The study of connective tissue reaction to radiation: The sieve or chess method," *Br J Cancer*, vol. 3, pp. 27–31, 1949.

[9] H Marks, "Clinical experience with irradiation through a grid," *Radiology*, vol. 58, pp. 338–342, 1952.

[10] R Loeviger, *Encyclopedia of Medical Radiology*. Springer-Verlag, 1970.

[11] M Urano, G Kaneda, and S Shimazaki, "Radiation dose tumor-control assays for irradation through a sieve," *Am. J. Roentgenol.*, vol. 102, pp. 38–42, 1968.

[12] R Asur, K. Butterworth, J Penagaricano, K Prise, and R Griffin, "High dose bystander effects in spatially fractionated radiation therapy," *Cancer Letters*, vol. 356, pp. 52–57, 2015.

[13] M Kudrimoti, W Regine, J Huhn, A Meigooni, M Ahmend, and M Mohiuddin, "Spatially fractionated radiation therapy (sfr) in the palliation of large bulky melanomas," *I J Radiation Oncology*, vol. 54, no. 2, pp. 342–343, 2002, Supplement.

[14] H Zhang, H Zhong, R. Barth, M Cao, and I. Das, "Impact of dose size in single fraction spatially fractionated (grid) radiotherapy for melanoma," *Med Phys*, vol. 41, no. 2, 2014.

[15] H Zhang and et al, "Fractionated grid therapy in treating cervical cancers: Conventional fractionation or hypofractionation?" *Int J Radiat Oncol Biol Phys*, vol. 70, pp. 280–288, 2008.

[16] J. Penagaricano, E. Moros, V Ratanatharathorn, Y Yan, and P Corry, "Evaluation of spatially fractionated radiotherapy (grid) and definitive chemoradiotherapy with curative intent for locally advanced squamous cell carcinoma of the head and neck: Initial response rate and toxicity," *Int. J. Radiation Oncology Biol. Phys.*, vol. 76, no. 5, pp. 1369–1375, 2010.

[17] H. Costlow, H Zhang, and I. Das, "A treatment planning approach to spatially fractionated megavoltage grid therapy for bulky lung cancer," *Med Dosim*, vol. 39, pp. 218–26, 2014.

[18] C Buckey, S Stathakis, K Cashon, and et al, "Evaluation of a commercially-available block for spatially fractionated radiation therapy," *J Appl Clin Med Phys*, vol. 11, no. 3, pp. 3163–3172, 2010.

[19] M Mohiuddin, D. Curtis, W. Grizos, and L Komarnicky, "Palliative treatment of advanced cancer using multiple nonconfluent pencil beam radiation," *Cancer*, vol. 66, no. 1, pp. 114–8, 1990.

[20] S Poh, M Chua, and J Wee, "Why we should give spatially fractionated radiation therapy (grid) a second look - especially in nasopharyngeal carcinoma," *Annals of Nasopharynx Cancer*, vol. 2, no. 4, pp. 12–19, 2018.

[21] R. Zwicker, A Meigooni, and M Mohiuddin, "Therapeutic advantage of grid irradiation for large single fractions," *Int J Radiat Oncol Biol Phys*, vol. 58, pp. 1309–1315, 2004.

[22] C. Johnson, H. Thames, D. Huang, and R. Schmidt-Ullrich, "The tumor volume and clonogen number relationship: Tumor control predictions based upon tumor volume estimates derived from computed tomography," *Int. J. Radiation Oncology Biol. Phys*, vol. 33, no. 2, pp. 281–287, 1995.

[23] J. Ha, G Zhang, S. Naqvi, W. Regine, and C. Yu, "Feasibility of delivering grid therapy using a multileaf collimator," *Med Phys*, vol. 33, no. 1, pp. 76–82, 2006.

[24] V Peng, N Suchowerska, L Rogers, E Mackonis, S Oakes, and D McKenzie, "Grid thereapy using high definition multileaf collimators:realizing benefits of the bystander effect," *Acta Oncologia*, vol. 56, no. 8, pp. 1048–1059, 2017.

[25] J. Jin, B Zhao, J Kaminski, N Wen, Y Huang, J Vender, I Chetty, and F. Kong, "A mlc-based inversely optimized 3d spatially fractionated grid radiotherapy technique," *Radiotherapy and Oncology*, vol. 117, pp. 483–486, 2015.

[26] G Neuner, M. Mohiuddin, N Vander Walde, and et al, "High-dose spatially fractionated grid radiation therapy (sfgrt): A comparision of treatment outcomes with cerrobend vs mlc sfgrt," *Int J Radiat Oncol Biol Phys.*, vol. 33, no. 1, pp. 76–82, 201.

[27] A Nobah, M Mohiddin, and B Moftah, "Effective saptially fractionated grid radiation treatment planning for a passive grid block," *Br J Radiol*, 2015.

[28] H Zhang, E. Johnson, and R. Zwicker, "Dosimetric vaildation of the mcnpx monte carlo simulation for radiobiologic studies of megacvoltage grid radiotherapy," *Int J Radiat Oncol Biol Phys*, vol. 66, pp. 1576–1583, 2006.

[29] S Gholami, H. Nedaie, A. Meigooni, and F Longo, "Grid therapy: Impact of radiobiological models on calculation of therapeutic ratio," in *IFMBE*, World Congress on Medical Physics and Biomedical Engineering, vol. 51, 2015, pp. 487–489.

[30] K Prise and J O'Sullivan, "Radiation-induced bystander signalling in cancer therapy," *Nat Rev Cancer*, vol. 9, pp. 351–60, 2009.

[31] R Yahyapour, E Motevaaseli, A Rezaeyan, H Abdollahi, B Farhood, M Checki, M Najafi, and V Villa, "Mechanisms of radiation bystander and non-targeted effects: Implications to radiation carciogenesis and radiotherapy," *Current Radiopharmaceuticals*, vol. 11, pp. 1–12, 2018.

[32] C Fernandez-Palomo, E Schultke, R Smith, E Brauer-Krisch, J Laissue, C Schroll, J Fazzari, C Seymour, and C Mothersill, "Bystander effects in tumor-free and tumor-bearing rat brains following irradiation by synchrotron x-rays," *International Journal of Radiation Biology*, vol. 89, no. 6, pp. 445–453, 2013.

[33] E Brauer-Krisch, R Serduc, E. Siegbahn, and et al, "Effects of pulsed, spatially fractionated, microscopic synchrotron x-ray beams on normal and tumoral brain tissue," *Mutation Research/Reviews in Mutation Research*, vol. 704, pp. 160–166, 2010.

[34] R ZWICKER, A Meigooni, and M Mohiuddin, "Radiobiological advantage of megavoltage grid therapy," *International Journal of Radiation Oncology Biology Physics*, vol. 51, no. 1, p. 401, 2001.

[35] J. Hopewell, "The skin: Its structure and response to ionizing radiation," *Int J Radiat Biol*, vol. 57, no. 4, pp. 751–73, 1990.

[36] Y. Lawrence, X. Li, I. Naqa, C. Hahn, L. Marks, T. Merchant, and A. Dicker, "Radiation dose-volume effects in the brain," *Int J Radiat Oncol Biol Phys*, vol. 76, S20–S27, 2010.

[37] D Schneider and D Cormach, "Monte carlo calculations of electron energy loss," *Radiat. Res.*, vol. 11, pp. 418–29, 1959.

[38] W Bruce, M Pearson, and H Johns, "Comparison of monte carlo calculations and experimental measurements of scattered radiation produced in a water phantom by primary radiations with half-value layers from 1.25 mm cu to 11 mm pb," *Radiat. Res*, vol. 17, 1962.

[39] D Rogers, "Fifty years of monte carlo simulations for medical physics," *Phys. Med. Biol.*, vol. 51, 2006.

[40] P Andero, "Monte carlo techniques in medical radiation physics," *Phys. Med. Biol.*, vol. 36, 1991.

[41] M Berger, "Methods in computational physics," in, B Alder, S Fernbach, and M Rotenberg, Eds. New York:Academic, 1963, vol. 1, ch. Monte Carlo calculations of the penetration and diffusion of fast charged particles.

[42] E Spezi and G Lewis, "An overview of monte carlo treatment planning for radiotherpy," *Radiation Protection Dosimetry*, vol. 131, no. 1, pp. 123–129, 2008.

[43] A Moutsatsos, E Pantelis, E Pappas, and P Papagiannis, "Experimental dosimetry for model-based ir-192 hdr brachytherapy treatment planning," *Physica Medica*, vol. 30, e36, 2014.

[44] B Juste, R Miro, S Gallardo, G Verdu, and A Santos, "Considerations of mcnp monte carlo code to be used as a radiotherapy treatment planning tool," in *2005 IEEE Engineering in Medicine and Biology 27th Annual Conference*, IEEE, 2006.

[45] I Jabbari and S Monadi, "Development and validation of mcnpx-based monte carlo treatment plan verification system," *J Med Phys*, vol. 40, no. 2, pp. 80–89, 2015.

[46] A Niroomand-Rad, C Blackwell, B Coursey, K Gall, J Galvin, W McLaughlin, A Meigooni, R Nath, J Rodgers, and C Soares, "Radiochromic film dosimetry: Recommendations of aapm radiation therapy committee task group 55," *Med Phys*, vol. 25, no. 11, 1998.

[47] *Ebt3 specification and user guide*, Ashland.

[48] K. Lin, C. Huang, J. Lin, and T. Chu, "Surface dose with grids in electron beam radiation therapy," *Applied Radiation and Isotopes*, vol. 56, pp. 477–484, 2002.

[49] M Tamura, H Monzen, K Kubo, M Hirata, and Y Nishimura, "Feasibility of tungsten functional paper in electron grid therapy: A monte carlo study," *Phys Med Biol*, vol. 62, pp. 878–889, 2017.

[50] A. Meigooni, S. Parker, J Zheng, K. Kalbaugh, W. Regine, and M Mohiuddin, "Dosimetric characteristics with spatial fractionation using electron grid therapy," *Medical Dosimetry*, vol. 27, no. 1, pp. 37–42, 2002.

[51] S. Almberg, J Frengen, A Kylling, and T Lindmo, "Monte carlo linear accelerator simulation of megavoltage photon beams: Independent determination of initial beam parameters," *Med Phys*, vol. 39, no. 1, pp. 40–7, 2012.

[52] B Serrano, A Hachem, E Franchisseur, J Herault, S Marcie, A Costa, R. Bensadoun, and J Barthe, "Monte carlo simulation of a medical linear accelerator for radiotherapy use," *Radiat Prot Dosimetry*, vol. 119, no. 1-4, pp. 506–9, 2006.

[53] S. Lin, T. Chu, and J. Lin, "Monte carlo simulation of a clinical linear acclerator," *Applied Radiation and Isotopes*, vol. 55, no. 6, pp. 759–765, 2001.

[54] K. O'Grady, "Monte carlo modeling of the varian truebeam linear accelerator, with chamber effects included in determination of the source parameters," Master's thesis, McGill University, 2016.

[55] Khan, *Handbook of the Physics of Radiation Therapy*.,.

[56] U. of Maryland Radiation Facilities, *Varian clinac-6 linear accelerator*, Online, 2019.

[57] M. Berger, J. Coursey, M. Zucker, and J Chang, "Stopping-power and range tables for electrons, protons, and helium ions," NIST, Tech. Rep., 2017.

[58] P Almond, P Biggs, B Coursey, W Hanson, M Huq, R Nath, and D Rogers, "Aapm's tg-51 protocol for clinical reference dosimetry of high-energy photon and electron beams," *Med Phys*, vol. 26, no. 9, pp. 1847–70, 1999.